FORMATION FLIGHT FOR FUEL SAVING IN CORONET MISSIONS OF KC-135R AND F-15C/E

by

CHRISTOPHER ALLEN KNIFFIN

Presented to the Faculty of the Graduate School of
The University of Texas at Arlington in Partial Fulfillment
of the Requirements
for the Degree of

MASTER OF SCIENCE

THE UNIVERSITY OF TEXAS AT ARLINGTON
December 2016

ACKNOWLEDGEMENTS

I would like to thank my supervising professor Dr. Atilla Dogan for his invaluable advice and guidance during the course of my studies.

I wish to thank my thesis committee Dr. Kamesh Subbarao and Dr. Donald Wilson for taking the time to serve in my thesis committee and providing crucial feedback.

I would also like to extend my appreciation to William Blake for providing much of the data used in this thesis and providing invaluable guidance.

November 17, 2016

ABSTRACT

FORMATION FLIGHT FOR FUEL SAVING IN CORONET MISSIONS OF KC-135R AND F-15C/E

CHRISTOPHER ALLEN KNIFFIN, M.S.

The University of Texas at Arlington, 2016

Supervising Professor: Atilla Dogan

The fuel saving benefit of formation flight has been demonstrated through theoretical and computational analyses, simulation, wind tunnel and flight tests. When an aircraft flies in a specific region in the wake of another aircraft, it experiences upwash, which results in reduced drag and thus reduced thrust requirement. One specific USAF mission that can potentially benefit from formation flight is coronet missions. In a coronet mission, fighter aircraft are escorted and refueled, as needed, by tanker aircraft over a long range. During the flight, the receiver aircraft fly in formation with the tanker but outside of the wake of the tanker except when they need refueling. In this thesis, the idea of flying the receivers at the sweet spot within the wake of the tanker is investigated. A high fidelity simulation has been developed that models the relative motion of multiple aircraft, aerodynamic coupling between the aircraft, and the effect of mass variation through fuel burn and fuel transfer. Various coronet missions for F-15C and F-15E aircraft escorted by a KC-135R have been simulated. The simulation results are used to quantify the benefit of flying at the sweet spot as compared to outside the wake in terms of the amount of fuel saved.

The results show a significant amount of fuel savings for the whole fleet of KC-135R and multiple F-15C or F-15E when the F-15s fly at the sweet spot. The results also showed that the fighter aircraft can fly longer before refueling if it flies at the sweet spot. This implies that the number of refueling maneuvers and number of tanker aircraft involved in a coronet mission can potentially be reduced. The possibility of additional savings is explored by comparing several trimming methods, as well as tracking the sweet spot. The results show that the trimming method only has an insignificant effect on the fuel burn, however, tracking the sweet spot yields significant additional fuel savings.

TABLE OF CONTENTS

Appendix

LIST OF ILLUSTRATIONS

LIST OF TABLES

Table Page

CHAPTER 1

INTRODUCTION

Formation flight for drag reduction, termed “Surfing Aircraft Vortices for Energy“ or \$AVE within the U.S. Air Force, has the potential to reduce fuel consumption by millions of gallons per year [1]. Using this concept, trailing aircraft in a formation fly close to the wake of a lead aircraft, taking advantage of the beneficial upwash generated by the trailing vortices from the leader. The effect is similar to surfing on a wave of air, hence the term \$AVE. Fuel savings from 10-15% have been demonstrated for formations of similar aircraft [1]. Although formation flight is common in the military, formations are designed to avoid aircraft getting too close to trailing vortices from another aircraft. Many accidents in both the civil and military have resulted from smaller aircraft flying too close to the wake of a larger aircraft, resulting in an out of control situation. Before any aircraft pair attempt to make use of \$AVE, the safety concerns due to an inadvertent wake crossing must be addressed.

A \$AVE application that has the potential to save more than just fuel is the USAF “Coronet“ mission. Coronet missions are long distance (usually transoceanic) movements of fighters escorted by tankers [2]. Coronets are used for exercises, to support contingencies, and conduct scheduled rotations of aircraft. In addition to providing fuel to avoid intermediate stops, the tankers carry the fighter unit‘s personnel and equipment. This allows the aircraft to be ready for immediate follow-on missions. Hundreds of Coronet missions are conducted each year that escort thousands of fighters to their destinations [3].

A typical Coronet mission consists of one or more tankers escorting two or more fighters (a group of six fighters is very common). If the fighters can use $AVE to reduce their fuel consumption, then their required fuel onload will be reduced. This leads to several intriguing possibilities in addition to significant fuel savings [4]. The number of tankers required for a given number of fighters could be reduced, the number of fighters escorted by a given number of tankers could be increased, or both. Since coronet missions are currently planned with the number of fighters to be escorted as a fixed quantity, initial assessments should concentrate on possible tanker reductions. If these can be attained the fuel saved is much larger than just the reduced fighter onload. The fuel expended by the tankers just to fly the mission is also eliminated. Other savings include non-fuel related operating costs (crew etc) and the minor wear and tear due to takeoff/landing, engine, and fuselage pressurization cycles.

For a Coronet $AVE application, fighters could fly in formation with each other, yielding a fuel reduction on the trail but the lead would reap no benefit. A larger benefit could potentially be attained if the fighters fly in formation behind the tankers. If there is at least one tanker for every two fighters, then each could equally benefit. The span loading of modern tankers is roughly twice the span loading of fighters. The size and strength of the beneficial upwash needed for $AVE is directly proportional to span loading, hence the expected savings would be larger. Although the details are unpublished, test flights of an F/A-18 behind a DC-8 conducted by NASA indicated a 29% fuel reduction on the F/A-18 [5].

This thesis will answer the following questions:

1. Does the F-15C/F-15E have enough control authority to fly within the tanker's wake?
2. How much fuel can be saved by flying at the sweet spot?
3. Can the number of refuelings be reduced?

4. Is it possible to reduce the number of tanker aircraft necessary to escort fighters?

These questions will be answered by simulating a coronet mission with a tanker and one or two fighter aircraft. First, it is necessary to create sweet spot contour plots to obtain the location of the sweet spot. The sweet spot location can then be used to simulate a coronet mission. The results of the coronet mission simulation at the sweet spot are compared to the results of the same coronet mission flown in formation out of the wake. This research is the first effort, reported in the literature, that studies aerial refueling and formation flight for fuel saving together.

This research effort is built on prior work on aerial refueling and formation flight. Several of the methods and tools used in this research were initially developed and used for simulation and control of aircraft in aerial refueling (AR)[6, 7]. A new set of nonlinear 6-DOF equations of motion (EOM) of an aircraft undergoing aerial refueling that include the time-varying mass and inertia associated with the fuel transfer as well as the effect of nonuniform wind induced by the tanker was developed, using the theory of mass-varying systems [6, 7]. The EOM were implemented in an integrated simulation environment with a feedback controller for tracking position commands relative to the tanker aircraft as well as the full set of nonlinear, 6–DOF EOM of the tanker aircraft and a feedback controller [8] to fly the tanker along a desired trajectory. When an aircraft is exposed to a non-uniform wind field, standard aerodynamic force and moment equations, based on airspeed, angles of attack and sideslip, and uniform wind components and gradients acting at the CM of the aircraft, cannot be used directly. To overcome this difficulty, Nonuniform Wind Effect Modeling Technique (NUWEMT) was developed. NUWEMT approximates the non-uniform wind/flow field by equivalent uniform translational and rotational wind components [9, 10]. The 2004 test flight data generated by the automated aerial refueling (AAR) program of AFRL with a KC-135R as the tanker and a Calspan Learjet as the surrogate receiver UAV was analyzed. This analysis also involved reproducing the test flight in the simulation environment employing the EOM and NUWEMT [11]. This research work [12–14] resulted in (i) characterization of the mean variation and stochastic content of wind that the tanker and receiver were exposed to during the test flight, and (ii) validation of the NUWEMT and turbulence characterization through the comparison of simulation results with the flight data. The simulation environment was later modified for formation flight of an EQ-II aircraft (a tailless flying wing configuration) behind a KC-135R in an aerial refueling operation [15]. This enabled the simulation of the EQ-II models, with different payload and fuel configurations, flying in the 2004 AAR test flight. With this approach, the ability of EQ-II models to maneuver and maintain contact position behind the tanker was investigated in a realistic aerial refueling condition.

Using the capabilities of the AR simulation environment, the authors studied formation flight of a follower aircraft flying within the wake of a lead aircraft for the purpose of fuel saving. They first investigated (i) the effect of trimming the follower aircraft in the nonuniform wind field at the "sweet spot" with the highest lift-to-drag ratio and (ii) alternative moment generation methods such as fuel transfer between fuel tanks and differential thrusting [16, 17]. This required the amendment of the simulation environment for EQ-II aircraft flying behind a KC-135R to include the effect of variation of mass and CM of fuel in each fuel tank. This model has various fuel-flow-related control variables, (i) the overall fuel flow rate into the receiver, (ii) fuel flow rate into each individual fuel tank, (iii) the amount and (iv) the position vector of the fuel mass, which is assumed to be concentrated at the CM of the fuel in each fuel tank, expressed in the body frame of the receiver. Closed-form mathematical expressions were developed for the CM of fuel in each fuel tank for given fuel amount in each fuel tank of EQ-II aircraft, which has fuel tanks of rather complicated shapes. In the case of formation flight, the derived formulations are used when the fuel is transferred between fuel tanks instead of from a tanker aircraft. Using the trajectory-tracking controller, the EQ-II aircraft was commanded to fly in formation with the KC-135R tanker aircraft. The commanded position relative to the KC-135R was selected to be at the sweet spot obtained based on a static analysis. This study showed that the control surface deflections required to compensate for the induced aerodynamic moments caused additional drag, which reduced the benefit of formation flight. The study also showed that the alternative trim mechanisms (fuel transfer between fuel tanks and differential thrusting) helped achieve the full benefit of formation flight if aircraft was exposed to significant aerodynamic moment at the sweet spot. A follow-up study using the same simulation environment with a pair of KC-135 aircraft flying in formation showed that the trail airplane did not experience any significant aerodynamic moment at the sweet spot and thus did not need alternative trim mechanisms to achieve full formation flight benefit [18]. Further, extended-duration flight was studied, which included the effects of turbulence, to better quantify the benefit of formation flight in terms of the amount of fuel saved. The study showed that over a 6.5 hour flight, the rate of fuel saved was reduced with time, implying that less fuel is saved as time goes on, caused by a reduction of tanker weight [19, 20]. The ride quality of flying in the sweet spot has also been examined. It has been shown that flying in the sweet spot does not have a detrimental impact to a person's comfort level onboard a trail aircraft in formation [19, 21].

The work presented in this thesis resulted in two conference papers. The first paper includes parts of Chapters 1, 2 and 7 and all of Chapter 3, while the second paper includes parts of Chapter 2 and 7 and all of Chapters 1 and 4, respectively [22, 23].

The rest of this thesis is organized as follows. Chapter 2 presents the simulation development, Chapter 3 lays the ground work for Chapter 4 by examining where the static and dynamic sweet spot are located and providing insight into the flow field behind the tanker, Chapter 4 discusses the coronet mission simulations for a single and two F-15C/E's following a KC-135R, Chapter 5 lays out alternative trimming methods, Chapter 6 examines sweet spot tracking in full mission simulations, which is followed by concluding remarks in Chapter 7.

CHAPTER 2

SIMULATION DEVELOPMENT

2.1 Overview

The simulation used for this analysis models full 6-DOF nonlinear dynamics of multiple aircraft. The aerodynamic coupling between aircraft in formation flight, aerial refueling and the transition from these positions is modeled. The motion of the trail aircraft is relative to the lead aircraft. Other details include mass and inertia variation due to fuel burn and fuel transfer for each fuel tank and the effect on the entire aircraft. The flight guidance and control system flies the tanker at the commanded flight condition. A separate flight guidance control system determines when receiver should be refueled and flies the receiver at and between the commanded positions relative to the tanker. It also regulates tank usage based on a schedule, fuel flow from the tanker into the receiver fuel tanks. The flight guidance and control system is designed to be robust against a nonuniform wind field and mass and inertia variation.

2.2 Nonlinear Aircraft Equations of Motion for Receiver Aircraft (F-15C and F-15E)

A new set of equations of motion relative to a non-inertial frame are derived for mass-varying aircraft experiencing wind in Ref. [24]. The translational and rotational dynamics equations are [24] for easy referencing

$$\dot{\mathcal{X}}_{\mathcal{R}} = \mathbf{f_1}\dot{\omega}_{B_R B_T} + c_1 \tag{2.1}$$

$$\dot{\omega}_{B_R B_T} = \mathbf{f_2}\dot{\mathcal{X}}_{\mathcal{R}} + c_2 \tag{2.2}$$

where

$$\mathcal{X}_{\mathcal{R}} = \begin{bmatrix} V \\ \beta \\ \alpha \end{bmatrix} \tag{2.3}$$

$$\omega_{B_R B_T} = \begin{bmatrix} p \\ q \\ r \end{bmatrix} \tag{2.4}$$

$$\mathbf{f_1} = -\mathcal{E}_{\mathbf{R}}^{-\mathbf{1}}\mathbf{S}(\rho_{\mathbf{cm,t}}) \tag{2.5}$$

where

$$\mathcal{E}_{\mathbf{R}} = \begin{bmatrix} \cos\beta_R \cos\alpha_R & -V_R \sin\beta_R \cos\alpha_R & -V_R \cos\beta_R \cos\alpha_R \\ \sin\beta_R & V_R \cos\beta_R & 0 \\ \cos\beta_R \sin\alpha_R & -V_R \sin\beta_R \sin\alpha_R & V_R \cos\beta_R \cos\alpha_R \end{bmatrix} \tag{2.6}$$

and $S(\rho_{cm,t})$ is the skew symmetric operation on $\rho_{cm,t}$ defined in Appendix B. The skew symmetric operation is used throughout this section.

$$\begin{aligned} c_1 = \mathcal{E}_{\mathbf{R}}^{-\mathbf{1}} \Bigg\{ & \frac{1}{m_t} F_{B_R} + \frac{\dot{m}}{m_t} \mathbf{R_{B_R B_T} R_{B_T I}} \, \dot{r}_{B_T} - \dot{W} \\ & + \Big[\mathbf{S}(\omega_{\mathbf{B_R B_T}} + \mathbf{R_{B_R B_T}} \omega_{\mathbf{B_T}}) - \frac{\dot{m}}{m_t} \Big] \big(\mathbf{R_{B_R W_R}} \, U + W \big) \\ & - \Big[\mathbf{S^2}(\omega_{\mathbf{B_R B_T}} + \mathbf{R_{B_R B_T}} \omega_{\mathbf{B_T}}) - \mathbf{S}\left(\mathbf{S}(\omega_{\mathbf{B_R B_T}}) \mathbf{R_{B_R B_T}} \omega_{\mathbf{B_T}} \right) - \mathbf{S}(\mathbf{R_{B_R B_T}} \dot{\omega}_{\mathbf{B_T}}) \Big] \rho_{cm,t} \\ & - \frac{\dot{m}}{m_t} \Big[- \mathbf{R_{B_R B_T}} V_{\dot{m}} + \mathbf{R_{B_R B_T}} \mathbf{S}(\omega_{\mathbf{B_T}}) \rho_C \Big] - \frac{1}{m_t} \Bigg(\sum_{j=1}^{k} \dot{m}_j \dot{\rho}_{m_j} \Bigg) \\ & + \mathbf{S}(\omega_{\mathbf{B_R B_T}} + \mathbf{R_{B_R B_T}} \omega_{\mathbf{B_T}}) \frac{1}{m_t} \Bigg(\sum_{j=1}^{k} \dot{m}_j \rho_{m_j} + 2 \sum_{j=1}^{k} m_j \dot{\rho}_{m_j} \Bigg) - \frac{1}{m_t} \Bigg(\sum_{j=1}^{k} m_j \ddot{\rho}_{m_j} \Bigg) \Bigg\} \end{aligned} \tag{2.7}$$

where m_j is the mass of the fuel in the j-th tank and W is the translational components of the wind.

$$\mathbf{f_2} = \underline{\underline{\mathbf{I}}}_{\mathbf{t}}^{-\mathbf{1}} m_t \mathbf{S}(\rho_{\mathbf{cm,t}}) \mathcal{E}_{\mathbf{R}} \tag{2.8}$$

$$
\begin{aligned}
c_2 = \underline{\underline{\mathbf{I}}}_{\mathbf{t}}^{\mathbf{-1}} \Big\{ & M_{B_R} + \Big[\mathbf{S}(\omega_{\mathbf{B_R B_T}} + \mathbf{R_{B_R B_T}}\omega_{\mathbf{B_T}})\,\underline{\underline{\mathbf{I}}}_{\mathbf{t}} - \underline{\underline{\dot{\mathbf{I}}}}_{\mathbf{m}}\Big]\,(\omega_{B_R B_T} + \mathbf{R_{B_R B_T}}\omega_{B_T}) \\
& + m_t \mathbf{S}(\rho_{\mathbf{cm,t}})\dot{W} - \dot{m}\mathbf{S}(\rho_{\mathbf{R}})\mathbf{R_{B_R B_T}}\Big[\mathbf{R_{B_T I}}\dot{r}_{B_T} + V_{\dot{m}} - \mathbf{S}(\omega_{\mathbf{B_T}})\rho_C\Big] \\
& - \Big[m_t \mathbf{S}(\rho_{\mathbf{cm,t}})\mathbf{S}(\omega_{\mathbf{B_R B_T}} + \mathbf{R_{B_R B_T}}\omega_{\mathbf{B_T}}) - \sum_{j=1}^{k}\dot{m}_j \mathbf{S}(\rho_{m_j})\Big]\,(\mathbf{R_{B_R W_R}}U + W) \\
& + \sum_{j=1}^{k}\dot{m}_j \mathbf{S}(\rho_{m_j})\dot{\rho}_{m_j} + \sum_{j=1}^{k} m_j \mathbf{S}(\rho_{m_j})\ddot{\rho}_{m_j}\Big\} - \mathbf{S}(\omega_{B_R B_T})\mathbf{R_{B_R B_T}}\omega_{B_T} - \mathbf{R_{B_R B_T}}\dot{\omega}_{B_T}
\end{aligned}
\tag{2.9}
$$

Eqs. (2.1) and (2.2) are written in state-space form as [24]

$$\dot{\mathcal{X}}_{\mathcal{R}} = (\mathbf{I}_{3\times 3} - \mathbf{f}_1\mathbf{f}_2)^{-1}(\mathbf{f}_1 c_2 + c_1) \tag{2.10}$$

$$\dot{\omega}_{B_R B_T} = \left(\mathbf{I}_{3\times 3} + m_t \underline{\underline{\mathbf{I}}}_{\mathbf{t}}{}^{-1}\mathbf{S}^2(\rho_{cm,t})\right)^{-1}(\mathbf{f}_2 c_1 + c_2) \tag{2.11}$$

The applied force and moment vectors have three sources: (i) aerodynamics, (ii) propulsion and (iii) gravity. The total applied force, expressed in the body frame, is then

$$F_{B_R} = -\mathbf{R_{B_R W_R}}\begin{bmatrix} D \\ S \\ L \end{bmatrix} + \begin{bmatrix} F_{x_p} \\ F_{y_p} \\ F_{z_p} \end{bmatrix} + m_t \mathbf{R_{B_R B_T}}\mathbf{R_{B_T I}}\begin{bmatrix} 0 \\ 0 \\ g \end{bmatrix} \tag{2.12}$$

where m_t is the total mass of the receiver and g is the acceleration due to gravity. Since the aerodynamic and propulsive moments are both given in the body frame, the total moment with respect to the body frame is

$$M_{B_R} = \begin{bmatrix} \mathcal{L} \\ \mathcal{M} \\ \mathcal{N} \end{bmatrix} + \begin{bmatrix} M_{x_p} \\ M_{y_p} \\ M_{z_p} \end{bmatrix} - \Big[m_R \mathbf{S}(\rho_{cm}) + \sum_{j=1}^{k} m_j \mathbf{S}(\rho_{mj})\Big]\mathbf{R_{B_R B_T}}\mathbf{R_{B_T I}}\begin{bmatrix} 0 \\ 0 \\ g \end{bmatrix} \tag{2.13}$$

Rotational kinematics in matrix form is

$$\dot{E}_{\psi,\theta\,\phi} = \mathbf{L}(\theta,\phi)\omega_{B_R B_T} \tag{2.14}$$

where

$$E_{\psi,\theta,\phi} = \begin{bmatrix} \psi \\ \theta \\ \phi \end{bmatrix} \tag{2.15}$$

$$\mathbf{L}(\theta, \phi) = \begin{bmatrix} 0 & \sin\phi\sec\theta & \cos\phi\sec\theta \\ 0 & \cos\phi & -\sin\phi \\ 0 & \sin\phi\tan\theta & \cos\phi\tan\theta \end{bmatrix} \tag{2.16}$$

Translational kinematics in matrix form is [24]

$$\dot{\xi} = \mathbf{R^T_{B_R B_T}} \mathbf{R_{B_R W_R}} U + \mathbf{R^T_{B_R B_T}} W - \mathbf{R_{B_T I}} \dot{r}_{B_T} + \mathbf{S}(\omega_{B_T})\xi \tag{2.17}$$

Combining all four parts of the equations of motion from Eqs. (2.10), (2.11) (2.14), and (2.17) into a state-space form and expressing them in a compact form leads to

$$\dot{x} = f(x, v, w) \tag{2.18}$$

where x is the state vector

$$x = [V\ \beta\ \alpha\ p\ q\ r\ \psi\ \theta\ \phi\ \xi_x\ \xi_y\ \xi_z]^T \tag{2.19}$$

where (p, q, r), (ψ, θ, ϕ), and (ξ_x, ξ_y, ξ_z) are with respect to the body frame of the lead (tanker) aircraft. The applied force and moment vector, denoted as v in Eq. (2.18), is

$$v = [F_{x_{B_R}}\ F_{y_{B_R}}\ F_{z_{B_R}}\ M_{x_{B_R}}\ M_{y_{B_R}}\ M_{z_{B_R}}]^T \tag{2.20}$$

where $F_{x_{B_R}}$, $F_{y_{B_R}}$ and $F_{z_{B_R}}$ are the applied force components and $M_{x_{B_R}}$, $M_{y_{B_R}}$ and $M_{z_{B_R}}$ are the components of the applied moment around the origin of the receiver body frame. Both force and moments components are in the body frame of the receiver.

Similarly, noting that the applied forces and moments depend on the state variables x and control variables u_0, Eqs. (2.12) and (2.13) can be expressed in a compact form as

$$v = g(x, u_0) \tag{2.21}$$

where the control input vector is

$$u_o = [\delta_a \; \delta_{hL} \; \delta_{hR} \; \delta_r \; T_L \; T_R]^T \tag{2.22}$$

where δ_a, δ_{hL}, δ_{hR} and δ_r are the commanded aileron, left horizontal tail, right horizontal tail and rudder deflections, respectively. T_L and T_R are the commanded thrust by the left and right engine, respectively.

2.3 Aerodynamic Model

The authors were not able to find a comprehensive subsonic aerodynamic database on the F-15 in the open literature comparable to what exists for the F-16 [25]. F-15 aerodynamic and stability and control data are available from a variety of sources [26–31]. For this study, the vast majority of the stability and control derivatives were taken from Ref. [30]. Control derivatives not given by Ref. [30] were taken from Ref. [27]. Clean configuration drag was obtained from Ref. [32] and Ref. [31] with the remainder taken from Ref. [27] and Ref. [28]. Fighters typically carry external fuel tanks during Coronet missions. Incremental drag on an F-15 due to external fuel tanks was obtained from Ref. [33]. For the F-15C, drag, weight and fuel capacities for three 610 gallon external tanks (two wing-mounted, one fuselage-mounted) are given. For the F-15E, the same data for the conformal fuselage tanks and two wing-mounted tanks is given.

Drag due to control deflection, especially aileron and rudder, is very difficult to locate for most configurations. These terms are important for assessment of formation flight benefits since large rolling and yawing moments are induced on the trail aircraft. This trim drag penalty can use up much of the (untrimmed) drag benefit [34]. The authors found six component wind tunnel data with control deflections from tests conducted during the F-15 STOL Maneuver and Technology Demonstrator program [35]. Although the F-15 configuration tested included a canard which is not present on the production F-15, this is assumed not to affect the incremental drag due to control deflection. This data indicated the control drag of each effector was parabolic, as follows:

$$\begin{aligned}\Delta C_{D,controls} \quad &= \quad C_{D\delta_{dh}^2}(\delta_{h,L}^2 + \delta_{h,R}^2) + C_{D\delta_{dh}}(\mid \delta_{h,L} \mid + \mid \delta_{h,R} \mid) + C_{D\delta_a^2}\delta_a^2 \\ &\quad\quad + C_{D\delta_a} \mid \delta_a \mid + C_{D\delta_r^2}\delta_r^2 + C_{D\delta_r}\delta_r \qquad (2.23)\end{aligned}$$

Lift and pitching moment coefficient at zero angle of attack was also obtained from this database (from runs with the canard off). C_{Lq} and C_{mq} were obtained from a low fidelity digital DATCOM model using an elliptical fuselage model. The final form of the aerodynamic buildup expression is given below.

$$C_D = C_{D0} + C_{D\alpha^2}\alpha^2 + \Delta C_{D,controls} + \Delta C_{D,stores} \qquad (2.24)$$

$$C_S = C_{S\beta}\beta + C_{S\delta_r}\delta_r + C_{S\delta_{Dh}}(\delta_{h,l} - \delta_{h,r}) \qquad (2.25)$$

$$C_L = C_{L0} + C_{L\alpha}\alpha + C_{L\delta_h}(\delta_{h,l} + \delta_{h,r})/2 + C_{Lq}\left(\frac{c}{2V}\right)q \qquad (2.26)$$

$$C_l = C_{l\beta}\beta + C_{l\delta_r}\delta_r + C_{l\delta_a}\delta_a + C_{l\delta_{Dh}}(\delta_{h,l} - \delta_{h,r}) + C_{lp}\left(\frac{b}{2V}\right)p + C_{lr}\left(\frac{b}{2V}\right)r \qquad (2.27)$$

$$C_m = C_{m0} + C_{m\alpha}\alpha + C_{m\delta_h}(\delta_{h,l} + \delta_{h,r})/2 + C_{mq}\left(\frac{c}{2V}\right)q \qquad (2.28)$$

$$C_n = C_{n\beta}\beta + C_{n\delta_r}\delta_r + C_{n\delta_a}\delta_a + C_{n\delta D_h}(\delta_{h,l} - \delta_{h,r}) + C_{np}\left(\frac{b}{2V}\right)p + C_{nr}\left(\frac{b}{2V}\right)r \qquad (2.29)$$

The total aerodynamic forces are given by:

$$D = \frac{1}{2}\rho V^2 \mathcal{S} C_D \tag{2.30}$$

$$S = \frac{1}{2}\rho V^2 \mathcal{S} C_S \tag{2.31}$$

$$L = \frac{1}{2}\rho V^2 \mathcal{S} C_L \tag{2.32}$$

The total aerodynamic moments are given by:

$$\mathcal{L} = \frac{1}{2}\rho V^2 \mathcal{S} b C_l \tag{2.33}$$

$$\mathcal{M} = \frac{1}{2}\rho V^2 \mathcal{S} c C_m \tag{2.34}$$

$$\mathcal{N} = \frac{1}{2}\rho V^2 \mathcal{S} b C_n \tag{2.35}$$

where $\mathcal{S}$ is the reference area, b is the wing span, c is the mean aerodynamic chord and ρ is the ambient air density. The aerodynamic forces are with respect to the wind frame and the aerodynamic moments are with respect to the body frame. All parameters, including the origin of the body frame, are given in Appendix D.

2.4 Non-Uniform Wind Effect Modeling Technique (NUWEMT)

Since vortex–induced velocities acting on an aircraft are highly non-uniform, standard aerodynamic force and moment equations, based on airspeed, angles of attack and sideslip, and uniform wind components acting at the center of mass (CM) of the aircraft, cannot be used directly. Instead, NUWEMT is implemented, which enables the use of standard dynamic equations of motion and aerodynamic build-up equations with wind effect terms included [9,10,36–41]. The NUWEMT approximates the nonuniform wind field the aircraft is exposed to by uniform translational and rotational wind components. This method is validated using data from wind tunnel [9] and flight tests [12–14] conducted within the AFRL Automated Aerial Refueling (AAR) program. This approach has been proven very useful and accurate in the case of formation flight simulation and control [9, 10, 36, 38–40]. It has also been implemented for aerial refueling simulation and control design verification in Refs. [6, 12–14, 42–46].

2.5 Mass and Inertia Properties

In this analysis, a full F-15C is an F-15C with three filled external tanks, as well as full internal fuel. A full F-15E is an F-15E with three filled external tanks, as well as full internal fuel and full fuel in the conformal tanks. A weight summary of the aircraft and the fuel tanks is given in Table 2.1 For this analysis the empty F-15C and F-15E have full internal fuel, but empty external and conformal tanks.

Table 2.1. F-15 Aircraft and Fuel Mass Data

	F-15C	F-15E
Full Mass [kg]	25,566	34,251
Empty Mass (with full internal tanks) [kg]	20,170	24,564
# of External Tanks	3	3
External Tank Fuel Mass (each) [kg]	1,798	1,798
# of Conformal Tanks	None	2
Conformal Tanks Fuel Mass (each) [kg]	N/A	2,145

In simulations, the inertia matrix should change as the fuel amounts in fuel tanks vary through fuel burn or transfer. This requires the inertia matrix of the aircraft with empty external and conformal tanks. Further, the inertia matrix should be with respect to the origin of the body frame, not with respect to the center of mass of the full aircraft. The following discussion explains how this is achieved. The inertia matrices are transformed into the body-frame using the parallel axis theorem as

$$\underline{\underline{\mathbf{I}}}_{\mathbf{BF,FULL}} = \underline{\underline{\mathbf{I}}}_{\mathbf{CM,FULL}} + m\big[(\rho_{cm,full} \cdot \rho_{cm,full})\mathbf{I}_{3\times3} - \rho_{cm,full}\rho_{cm,full}^{T}\big] \tag{2.36}$$

where m is the mass of the full mass configuration, and $\rho_{cm,full}$ is the representation in the body frame of the position vector of the center of mass with respect to the origin of the body frame. Since the aircraft will vary its mass significantly during the simulation, it is necessary to characterize the change in inertia. The empty mass inertia matrix is used as baseline and the instantaneous fuel amount is added. To obtain the inertia matrix for the empty F-15C and F-15E the parallel axis theorem is used.

$$\underline{\underline{\mathbf{I}}}_{\mathbf{RB}} = \underline{\underline{\mathbf{I}}}_{\mathbf{BF,FULL}} - \sum_{j=1}^{k} m_{j,full}\big[(\rho_{j,full}^{T}\rho_{j,full})\mathbf{I}_{3\times3} - \rho_{j,full}\rho_{j,full}^{T}\big] \tag{2.37}$$

where $m_{j,full}$ is the mass of the fuel in the full j^{th} tank and $\rho_{j,full}$ is the representation in the body frame of the position vector of the CM of $m_{j,full}$ with respect to the origin of the body frame. The inertia matrix of the aircraft and fuel with respect to the body frame with a specified amount of fuel (m_j) in each fuel tank is

$$\underline{\underline{\mathbf{I}}}_{\mathbf{t}} = \underline{\underline{\mathbf{I}}}_{\mathbf{RB}} + \sum_{j=1}^{k} m_j \left[\big(\rho_{mj}^{T}\rho_{mj}\big)\mathbf{I}_{3\times3} - \rho_{mj}\rho_{mj}^{T}\right] \tag{2.38}$$

where ρ_{m_j} is the representation in the body frame of the CM position of fuel m_j in the j^{th} fuel tank with respect to the origin of the body frame.

The fuel tanks in F-15C and F-15E are used in a specific order. Similarly, in aerial refueling, the tanks are filled up in a specific sequence. The F-15C is set to burn fuel from the external wing tanks first. After they are depleted, the external fuselage tank is used. In aerial refueling, the external fuselage tank is filled first and then the external wing tanks are filled. The F-15E is set to burn fuel from the external wing tanks first. After they are depleted, the external fuselage tank is used. Lastly, the conformal tanks are depleted. In aerial refueling of F-15E, first, the external fuselage tank is filled, after that, the conformal tanks are filled; the external wing tanks are filled last.

A comparison between the F-15 and KC-135R masses used for the coronet mission in this analysis is given in Table 6.1.

Table 2.2. Coronet Mission Starting Mass

	KC-135R	F-15C	F-15E
Full Mass [kg]	146,280	25,556	34,251
Max Fuel Mass [kg]	92,156	5,394	9.684
Initial Mass / Max Mass	88%	100%	100%
Initial Fuel / Max Fuel	81%	100%	100%

2.6 Actuator Model for Control Surfaces

The maximum all-moving horizontal tail deflection is +15 deg down -29 deg up, however the maximum differential tail deflection is ±22 deg. The rate limit for the horizontal tails is 46 deg/s. The maximum aileron deflection is ±20 deg. The aileron deflection rate limit is 100 deg/s. The maximum rudder deflection is ±15 deg. The rudder deflection rate limit is 105 deg/s.

2.7 Engine Model

The components of the propulsive force in the body frame are

$$F_{x_p} = (T_L + T_R)c_{T_{xe}} \tag{2.39}$$

$$F_{y_p} = (T_L - T_R)c_{T_{ye}} \tag{2.40}$$

$$F_{z_p} = -(T_L + T_R)c_{T_{ze}} \tag{2.41}$$

where $c_{T_{x_e}}$, $c_{T_{y_e}}$ and $c_{T_{z_e}}$ are the directional thrust coefficients given by

$$c_{T_{x_e}} = \cos\delta_{T_{zi}} \cos\delta_{T_{yi}} \tag{2.42}$$

$$c_{T_{y_e}} = \cos\delta_{T_{zi}} \tag{2.43}$$

$$c_{T_{z_e}} = \cos\delta_{T_{zi}} \sin\delta_{T_{yi}} \tag{2.44}$$

where $\delta_{T_{yi}}$ and $\delta_{T_{zi}}$ are the inclination angles of the engines. The propulsive moment components are given by

$$M_{x_p} = (T_L - T_R)\rho_{x_e} \tag{2.45}$$

$$M_{y_p} = (T_L + T_R)\rho_{y_e} \tag{2.46}$$

$$M_{z_p} = (T_L - T_R)\rho_{z_e} \tag{2.47}$$

where ρ_{x_e}, ρ_{y_e} and ρ_{z_e} are given by

$$\rho_{x_e} = l_{zi} \sin\delta_{T_{zi}} + l_{yi} \cos\delta_{T_{zi}} \sin\delta_{T_{yi}} \tag{2.48}$$

$$\rho_{y_e} = l_{zi} \cos\delta_{T_{zi}} \cos\delta_{T_{yi}} + l_{xi} \cos\delta_{T_{zi}} \sin\delta_{T_{yi}} \tag{2.49}$$

$$\rho_{z_e} = l_{yi} \cos\delta_{T_{zi}} \cos\delta_{T_{yi}} + l_{xi} \sin\delta_{T_{zi}} \tag{2.50}$$

where l_{xi}, l_{yi} and l_{zi} are the components in the body frame of the position vector of the point of thrust application relative to the origin of the body frame of the receiver. All engine parameters are given in Appendix D.

This study assumed that the engines can provide the required thrust instantaneously. The maximum thrust available from each engine at the flight condition simulated is

$$T_{max} = 26.7\ kN$$

2.8 Linear Control Design

2.8.1 Trim Condition Analysis

The flight condition used in this analysis is straight level flight at 7616.9 m and 204.39 m/s airspeed. For the trim analysis the full weight and inertia configurations as defined in Section 2.5 are used. The trim condition is solved for zero bank angle by satisfying

$$\begin{bmatrix} \dot{\mathcal{X}}_R \\ \dot{\omega}_{B_R B_T} \\ \cos(\alpha)\sin(\theta) - \sin(\alpha)\cos(\phi)\cos(\theta) \end{bmatrix} = 0_{7\times 1} \tag{2.51}$$

All non-zero nominal values for the F-15C and F-15E at this flight condition and mass and inertia configuration are given in Table 2.3.

Table 2.3. Nominal Condition Trim Values

		Full F-15C	Full F-15E
α	deg	5.45	7.48
θ	deg	3.42	5.45
δ_{hL}	deg	-4.11	-5.15
δ_{hR}	deg	-4.11	-5.15
T_L	$\% \, T_{max}$	52.9	72.6
T_R	$\% \, T_{max}$	52.9	72.6

2.8.2 Aircraft Linear State-Space Model

To implement a gain scheduling controller using LQR control design, it is necessary to create linear state-space models at all nominal conditions selected to be included in the control design. Linearization is carried out in a modular approach. The equation of motion in Eq. (2.18) is linearized first, which should lead to

$$\Delta\dot{x} = \mathbf{A}\Delta x + \mathbf{B}\Delta v \tag{2.52}$$

where

$$\mathbf{A} = \begin{bmatrix} \mathbf{A}_{\mathbf{x}} \\ \mathbf{A}_{\omega} \\ \mathbf{A}_{\psi\theta\phi} \\ \mathbf{A}_{\zeta} \end{bmatrix} \tag{2.53}$$

$$\mathbf{B} = \begin{bmatrix} \mathbf{B}_{\mathbf{x}} \\ \mathbf{B}_{\omega} \\ \mathbf{0}_{\mathbf{6}\times\mathbf{6}} \end{bmatrix} \tag{2.54}$$

The components of A and B matrices are formulated in Appendix C. The linearization with respect to the tanker variables w is not done as the control law to be designed does not use that dependency. The linearization of the applied force and moment expression in Eq. (2.21) should yield

$$\Delta v = \mathbf{E}\Delta x + \mathbf{F}\Delta u_0 \tag{2.55}$$

The linear model of the aircraft is then obtained by combining Eqs. (2.52) and (2.55) as

$$\Delta\dot{x} = (\mathbf{A} + \mathbf{B}\ \mathbf{E})\Delta x + (\mathbf{B}\ \mathbf{F})\Delta u_0 \tag{2.56}$$

This modular linearization process consists of separately formulating matrices **A**, **B**, **E**, and **F**, which is done by the partial derivatives of Eqs. (2.1), (2.2), (2.14), (2.17) and (2.21). The details of this linearization process are given in Appendix C.

2.9 Augmentation with Position and Sideslip, Bank Angle or Yaw Angle-Error Integral States

The output of interest is the trajectory of the trailing aircraft relative to the leader. When the aircraft flies in the wake of the lead aircraft for the purpose of fuel saving, it is subject to induced aerodynamic moments. The trail aircraft when flying in cruise condition behind the lead aircraft needs to be trimmed to compensate for the induced aerodynamic moments. This can be done in one of the three different configurations, (1) zero sideslip, (2) zero bank angle, or (3) zero yaw angle relative to the lead. When one of these configurations is chosen, the other variables are trimmed at nonzero values. Depending on the configuration selected, the output vector is defined to be one of the following

$$y = [\Delta\beta \ \Delta\xi_x \ \Delta\xi_y \ \Delta\xi_z]^T \tag{2.57}$$

$$y = [\Delta\phi \ \Delta\xi_x \ \Delta\xi_y \ \Delta\xi_z]^T \tag{2.58}$$

$$y = [\Delta\psi \ \Delta\xi_x \ \Delta\xi_y \ \Delta\xi_z]^T \tag{2.59}$$

which is written in terms of the state vector as

$$y = \mathbf{C}\Delta x \tag{2.60}$$

where x is the state vector, defined in Eq. (2.19) and $\mathbf{C}$ and is chosen such that y is as defined in Eq. (2.57), (2.58) or (2.59). To ensure zero tracking error at the steady state condition, as well as zero sideslip, bank or yaw, four additional states are defined as the integral of the output error

$$e_r = y - y_c \tag{2.61}$$

where y_c is the commanded position and sideslip, bank or yaw angle of the receiver. With the integral states included, a new augmented state vector is defined as

$$x_A = \begin{bmatrix} \Delta x \\ e_r \end{bmatrix} \tag{2.62}$$

The augmented state-space equation for x_A, then, becomes

$$\dot{x}_A = \mathbf{A_A} x_A + \mathbf{B_A}\Delta u_0 \tag{2.63}$$

where

$$\mathbf{A_A} = \begin{bmatrix} \mathbf{A} + \mathbf{B}\ \mathbf{E} & \mathbf{0_{12\times 4}} \\ \mathbf{C} & \mathbf{0_{4\times 4}} \end{bmatrix} \tag{2.64}$$

$$\mathbf{B_A} = \begin{bmatrix} \mathbf{B}\ \mathbf{F} \\ \mathbf{0_{4\times 4}} \end{bmatrix} \tag{2.65}$$

2.9.1 New Control Vector

To simplify the control design, the aileron command, left and right tail commands and left and right thrust commands, included in the original control vector u_0 in Eq. (2.22), are replaced by an effective aileron command, an elevator command and a total thrust command. The effective aileron command consists of aileron and differential tail deflection, the elevator command consists of the mean tail deflection and the total thrust command consists of the combined left and right engine thrust. The new control vector is then defined as

$$u = [\delta_{a_{eff}}\ \delta_{hm}\ \delta_r\ T_t]^T \tag{2.66}$$

where $\delta_{a_{eff}}$ is the effective aileron deflection, δ_{hm} is the mean horizontal tail deflection, δ_r is the rudder deflection, and T_t is the total thrust. The mapping from u_0 to u is determined as follows. The mean and differential horizontal tail deflections are defined as

$$\delta_{hm} = \frac{1}{2}(\delta_{hL} + \delta_{hR}) \tag{2.67}$$

$$\delta_{hd} = \delta_{hL} - \delta_{hR} \tag{2.68}$$

The effective aileron deflection is the sum of the actual aileron and differential tail deflections as

$$\delta_{a_{eff}} = \delta_a + \delta_{hd} \tag{2.69}$$

In the F-15 control law, the differential tail use is set to be 30% of the actual aileron deflection. This implies

$$\delta_{hd} = 0.3\ \delta_a \tag{2.70}$$

Solving for δ_a in terms of $\delta_{a_{eff}}$ using Eqs. (2.69) and (2.70) gives

$$\delta_a = \frac{1}{1.3}\delta_{a_{eff}} \tag{2.71}$$

Solving for δ_{hL} and δ_{hR} in terms of $\delta_{a_{eff}}$ and δ_{hm} using Eqs. (2.69), (2.70) and (2.67) yields

$$\delta_{hL} \;=\; \frac{0.3}{2.6}\,\delta_{a_{eff}} + \delta_{hm} \tag{2.72}$$

$$\delta_{hR} \;=\; -\frac{0.3}{2.6}\,\delta_{a_{eff}} + \delta_{hm} \tag{2.73}$$

The total thrust is defined as

$$T_t = T_l + T_r \tag{2.74}$$

Since the left and right engine thrust are the same

$$T_l \;=\; \frac{1}{2}\,T_t \tag{2.75}$$

$$T_r \;=\; \frac{1}{2}\,T_t \tag{2.76}$$

Putting Eqs. (2.71), (2.72), (2.73), (2.75) and (2.76) together in matrix form, the mapping matrix is constructed between u and u_0 such that

$$u_0 = \mathbf{M_u} u \tag{2.77}$$

with

$$\mathbf{M_u} = \begin{bmatrix} \frac{1}{1.3} & 0 & 0 & 0 \\ \frac{0.3}{2.6} & 1 & 0 & 0 \\ -\frac{0.3}{2.6} & 1 & 0 & 0 \\ 0 & 0 & 1 & 0 \\ 0 & 0 & 0 & \frac{1}{2} \\ 0 & 0 & 0 & \frac{1}{2} \end{bmatrix} \tag{2.78}$$

After substituting u_0 from Eq. (2.77) into Eq. (2.63), the augmented state-space equation with the new control vector becomes

$$\dot{x}_A = \mathbf{A_A} x_A + \mathbf{B_A M_u} \Delta u \tag{2.79}$$

2.9.2 LQR Design

For gain scheduling, six different nominal conditions are defined and matrices of the linearized state-space equation in Eq. (2.79) are computed for each nominal condition. The six nominal conditions, as summarized in Table 2.4, represent straight-level flight with two different airspeeds and level turns (left and right) with the same two airspeeds. Based on Eq. (2.79), a state-space model for each nominal condition is written as

$$\dot{x}_A = \mathbf{A_{A_i}}\, x_A + \mathbf{B_{AM_i}}\, \Delta u \tag{2.80}$$

Table 2.4. Nominal Conditions by Turn rate and Airspeed

Nominal Condition	Tanker Yaw Rate	Tanker Airspeed
1	$\dot{\psi}_{T1}$	V_{T1}
2	$\dot{\psi}_{T1}$	V_{T2}
3	$\dot{\psi}_{T2}$	V_{T1}
4	$\dot{\psi}_{T2}$	V_{T2}
5	$\dot{\psi}_{T3}$	V_{T1}
6	$\dot{\psi}_{T3}$	V_{T2}

Using LQR design technique, the state feedback gain matrix $\mathbf{K_i}$ is obtained, for the state-space model in (2.80), to minimize the cost function:

$$J(\Delta u) = \int_{0}^{\infty} \left\{ x_A^T \, \mathbf{Q_i} \, x_A + \Delta u^T \, \mathbf{R_i} \, \Delta u \right\} \mathrm{d}t \tag{2.81}$$

where $\mathbf{Q_i}$ are symmetric positive semidefinite and $\mathbf{R_i}$ are symmetric positive definite. Note that matrices $\mathbf{Q_i}$ and $\mathbf{R_i}$ can be selected separately for each nominal condition.

Thus, the state feedback control laws with the integral control is

$$\Delta u_i = -\mathbf{K_i} \, x_A \tag{2.82}$$

where $i = \{1, 2, 3, 4, 5, 6\}$. Note that the control laws assume the availability of full state measurement or estimation for feedback. In the implementation of linear controllers, a Lagrange interpolation "scheduling" scheme is employed to determine effective values of the gains at a given flight condition. With this scheme, the nonlinear gain scheduling controller based on the six linear designs is

$$\begin{aligned}
\Delta u \;=\; & \frac{\left(\dot{\psi}_c - \dot{\psi}_{T2}\right)\left(\dot{\psi}_c - \dot{\psi}_{T3}\right)\left(V_c - V_{T2}\right)}{\left(\dot{\psi}_{T1} - \dot{\psi}_{T2}\right)\left(\dot{\psi}_{T1} - \dot{\psi}_{T3}\right)\left(V_{T1} - V_{T2}\right)}\, u_1 \\
& + \frac{\left(\dot{\psi}_c - \dot{\psi}_{T2}\right)\left(\dot{\psi}_c - \dot{\psi}_{T3}\right)\left(V_c - V_{T1}\right)}{\left(\dot{\psi}_{T1} - \dot{\psi}_{T2}\right)\left(\dot{\psi}_{T1} - \dot{\psi}_{T3}\right)\left(V_{T2} - V_{T1}\right)}\, u_2 \\
& + \frac{\left(\dot{\psi}_c - \dot{\psi}_{T1}\right)\left(\dot{\psi}_c - \dot{\psi}_{T3}\right)\left(V_c - V_{T2}\right)}{\left(\dot{\psi}_{T2} - \dot{\psi}_{T1}\right)\left(\dot{\psi}_{T2} - \dot{\psi}_{T3}\right)\left(V_{T1} - V_{T2}\right)}\, u_3 \\
& + \frac{\left(\dot{\psi}_c - \dot{\psi}_{T1}\right)\left(\dot{\psi}_c - \dot{\psi}_{T3}\right)\left(V_c - V_{T1}\right)}{\left(\dot{\psi}_{T2} - \dot{\psi}_{T1}\right)\left(\dot{\psi}_{T2} - \dot{\psi}_{T3}\right)\left(V_{T2} - V_{T1}\right)}\, u_4 \\
& + \frac{\left(\dot{\psi}_c - \dot{\psi}_{T1}\right)\left(\dot{\psi}_c - \dot{\psi}_{T2}\right)\left(V_c - V_{T2}\right)}{\left(\dot{\psi}_{T3} - \dot{\psi}_{T1}\right)\left(\dot{\psi}_{T3} - \dot{\psi}_{T1}\right)\left(V_{T1} - V_{T2}\right)}\, u_5 \\
& + \frac{\left(\dot{\psi}_c - \dot{\psi}_{T1}\right)\left(\dot{\psi}_c - \dot{\psi}_{T2}\right)\left(V_c - V_{T1}\right)}{\left(\dot{\psi}_{T3} - \dot{\psi}_{T1}\right)\left(\dot{\psi}_{T3} - \dot{\psi}_{T2}\right)\left(V_{T2} - V_{T1}\right)}\, u_6
\end{aligned} \tag{2.83}$$

CHAPTER 3

SWEET SPOT DETERMINATION

3.1 Static Sweet Spot Simulations

The static simulation is analogous to a wind tunnel test. During the simulation, the receiver aircraft, with all control deflections set to zero, is placed in a position relative to the tanker aircraft. The orientations of both aircraft are fixed at their nominal values. As the position of the receiver, within the wake of the tanker aircraft, is varied relative to the tanker, the aerodynamic forces and moments also change. For each relative point, aerodynamic force and moment coefficients are recorded. The static sweet spot is the location in formation flight, where the lift-to-drag ratio is largest. To determine this location, the simulation is run for all points in a grid. The grid used in this analysis spans from -0.2 KC-135R spans to 0.2 KC-135R spans vertically and 0.25 KC-135R spans to 1.2 KC-135R spans laterally and contains 1521 data points (39 vertical points by 39 horizontal points). The grid is depicted in Figure 3.1. The static simulations are run for 4 separate cases, each of which is a combination of a heavy or light tanker and a full or empty F-15 as defined in Section 2.5. The heavy tanker configuration used in this study is a KC135-R with 74529 kg fuel. The light tanker configuration represents a KC-135R with 34253 kg fuel. All 4 cases are run for both the F-15C and F-15E.

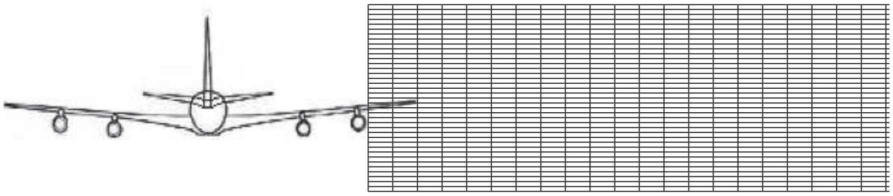

Figure 3.1. Depiction of Grid used in Static and Dynamic Simulations.

3.1.1 F-15C

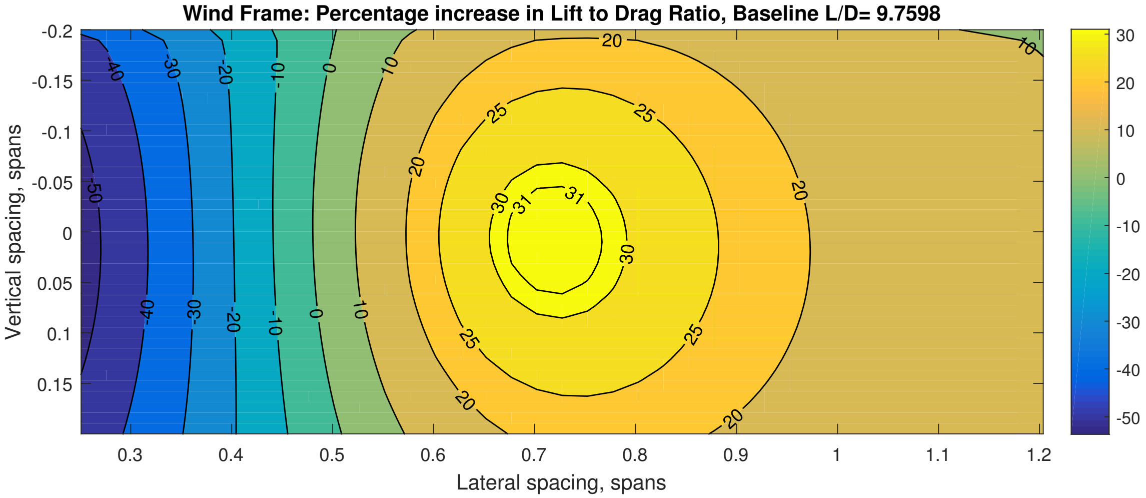

Figure 3.2. Change in Lift-to-Drag Ratio Simulation Results for the Full F-15C Heavy Tanker Case.

Figure 3.2 shows the change in lift-to-drag ratio for the heavy tanker full F-15C case. The static sweet spot is located 0.7272 spans laterally and 0.0102 spans below from the tanker. The increase in lift-to-drag ratio is 31.95% when compared to solo flight. The lift to drag ratio decreases as you move closer to the tanker. This is due to entering the downwash region of the tanker.

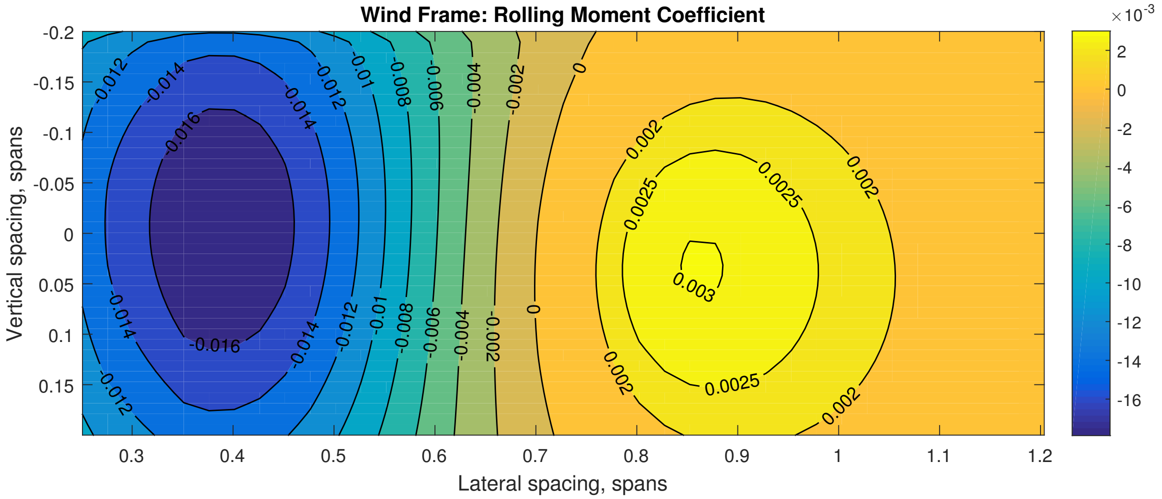

Figure 3.3. Rolling Moment Coefficient Simulation Results for the Full F-15C Heavy Tanker Case.

Figure 3.3 shows the induced rolling moment coefficient for the heavy tanker full F-15C case. To minimize trim drag it is desirable to fly with minimal control deflections. Flying at the zero induced rolling moment location would allow for flying without aileron deflection (as is the case in solo flight). The zero rolling moment line is located slightly inboard of the static sweet spot (0.7022 spans). At the static sweet spot there is a small rolling moment present, which will require very small aileron deflections and thus induced drag by aileron deflection will be small in the static sweet spot.

Figure 3.4 shows the pitching moment coefficient for the heavy tanker full F-15C case. At the static sweet spot the pitching moment has its maximum negative value. The magnitude of the pitching moment is increased by 142%, compared to solo flight, which will require additional negative tail deflections for trim. This should result in more induced drag for flying in the static sweet spot.

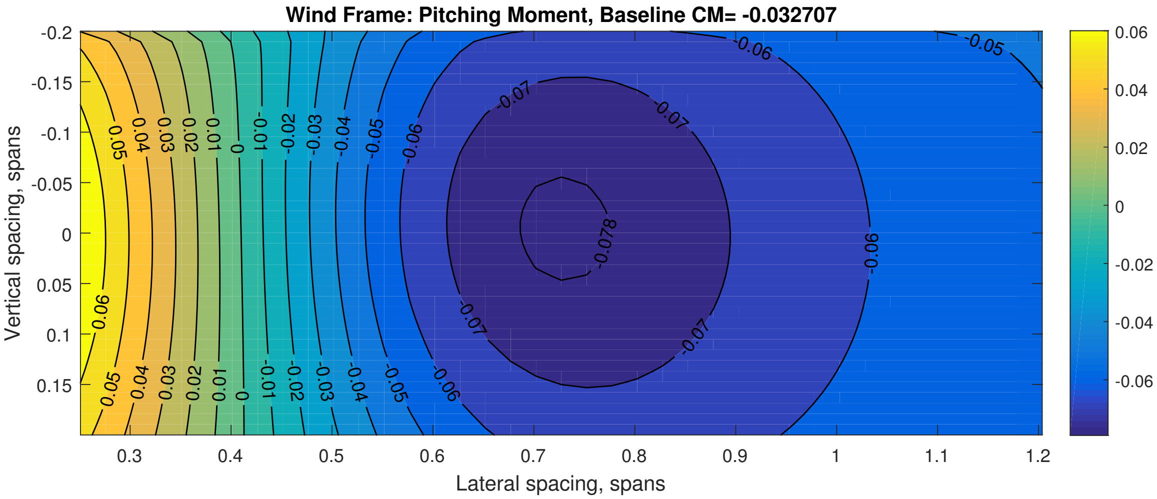

Figure 3.4. Pitching Moment Coefficient Simulation Results for the Full F-15C Heavy Tanker Case.

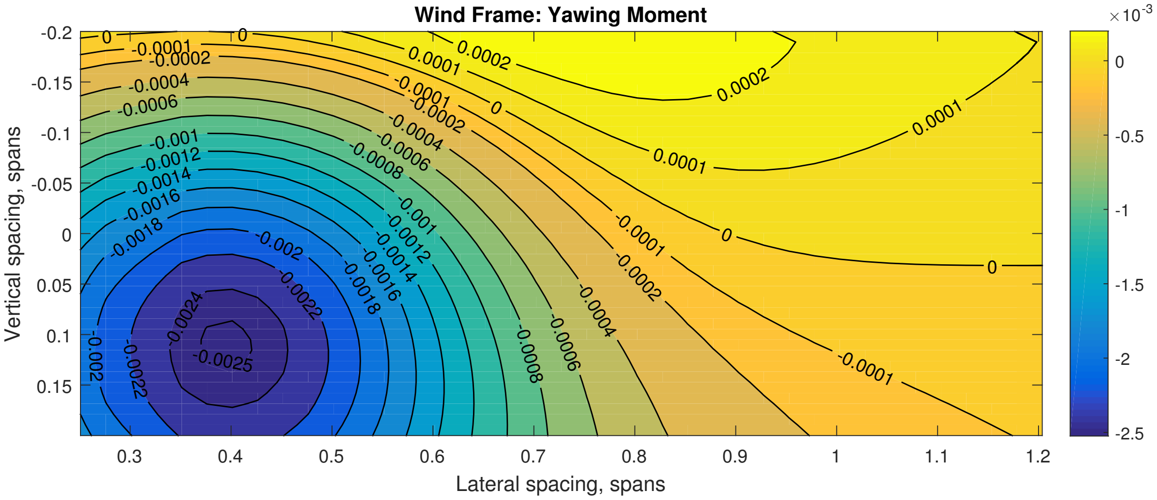

Figure 3.5. Yawing Moment Coefficient Simulation Results for the Full F-15C Heavy Tanker Case.

Figure 3.5 shows the induced yawing moment coefficient for the heavy tanker full F-15 case. While the zero yawing moment line is located away from the static sweet spot, the magnitude of the induced yawing moment at the static sweet spot is very small, so only small rudder deflections will be necessary.

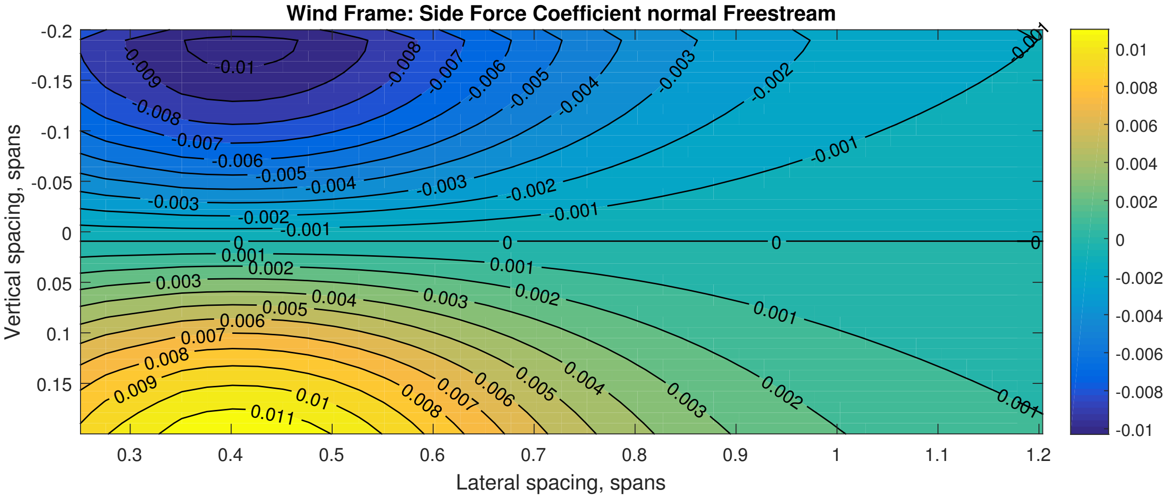

Figure 3.6. Side Force Coefficient Simulation Results for the Full F-15C Heavy Tanker Case.

Figure 3.6 shows the side force coefficient. The zero side force coefficient line runs laterally at 0.0102 spans below the tanker, which is the vertical location of the static sweet spot. Therefore no additional control deflections are necessary to cope with an induced side force, when flying at the static sweet spot. The contour plot shows that the induced side force depends mostly on the vertical spacing.

3.1.2 F-15E

The static results of the full F-15E heavy tanker case are very similar to those of the full F-15C heavy tanker case. Figure 3.7 shows the change in lift-to-drag ratio for the full F-15E heavy tanker case. The static sweet spot is at the same location as it is for the full F-15C heavy tanker case. The increase in lift-to-drag ratio at the sweet spot (23.97%), however, is lower than that of the F-15C.

Figure 3.8 shows the induced rolling moment coefficient for the full F-15E heavy tanker case. The zero rolling moment line is at the same location as it was for the F-15C.

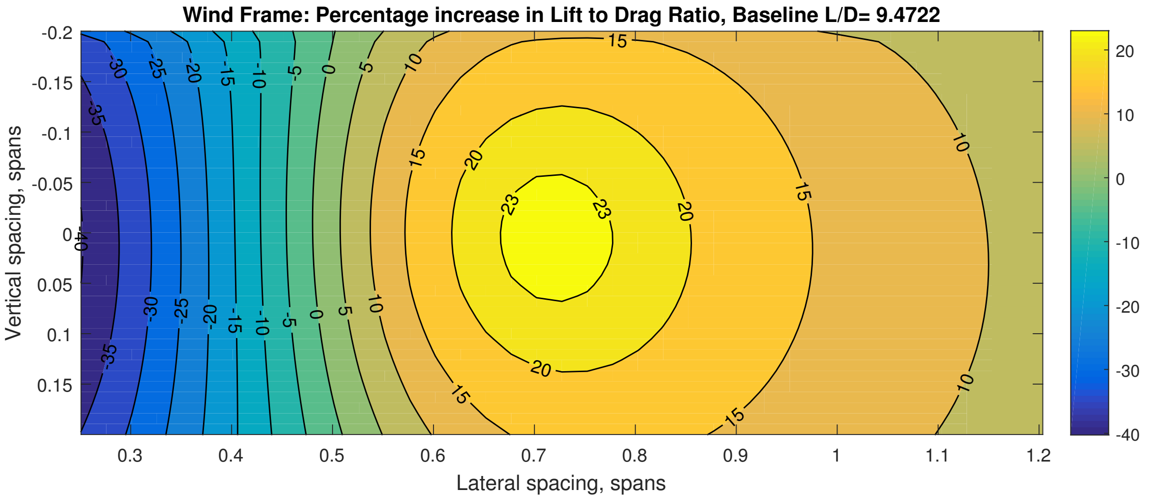

Figure 3.7. Lift-to-Drag Ratio Simulation Results for the Full F-15E Heavy Tanker Case.

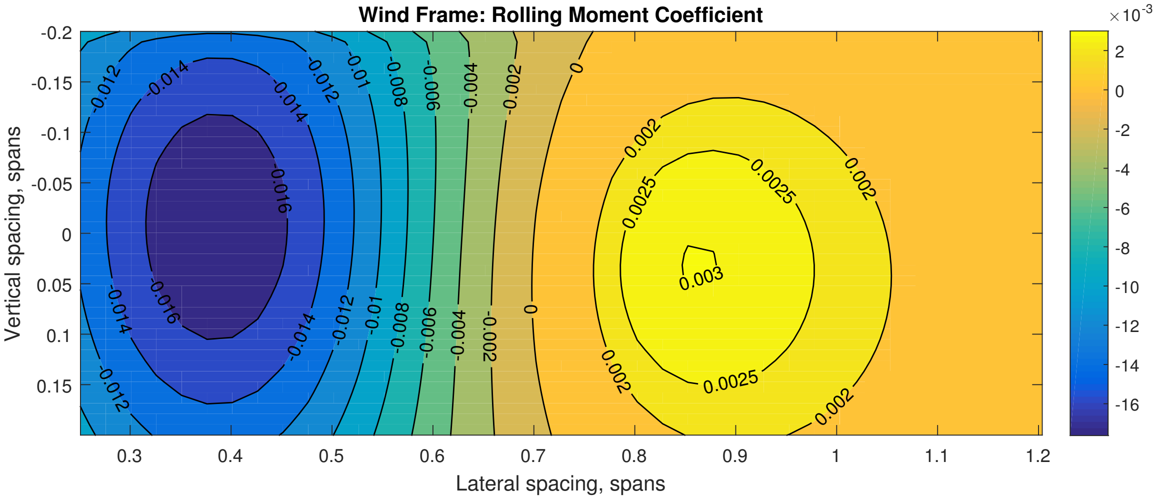

Figure 3.8. Rolling Moment Coefficient Simulation Results for the Full F-15E Heavy Tanker Case.

Figure 3.9 shows the pitching moment coefficient for the heavy tanker full F-15E case. Again, at the static sweet spot the pitching moment coefficient has its maximum negative value. The magnitude of the pitching moment is increased by 103%, compared to solo flight, which is a smaller increase than in the F-15C case.

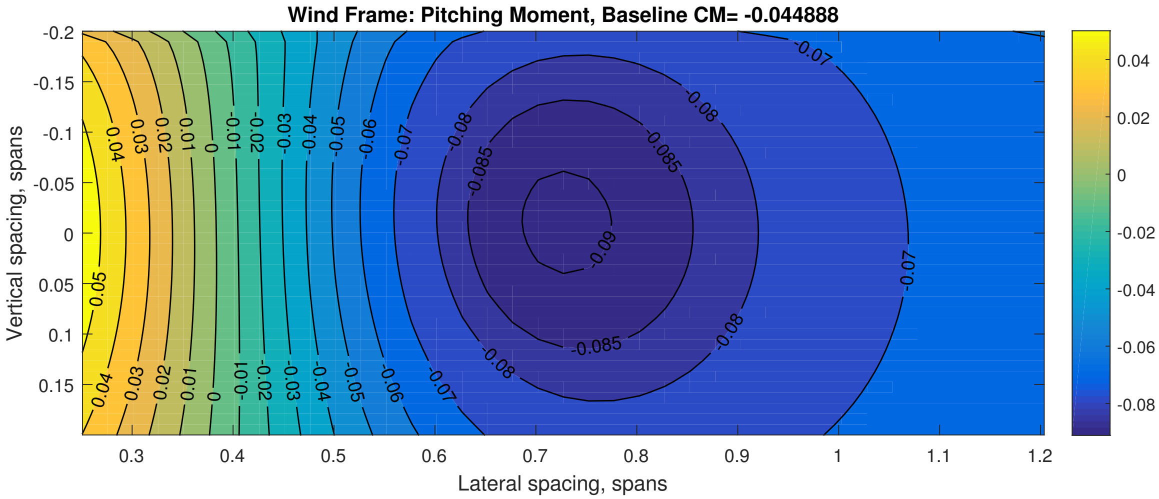
Wind Frame: Pitching Moment, Baseline CM= -0.044888

Figure 3.9. Pitching Moment Coefficient Simulation Results for the Full F-15E Heavy Tanker Case.

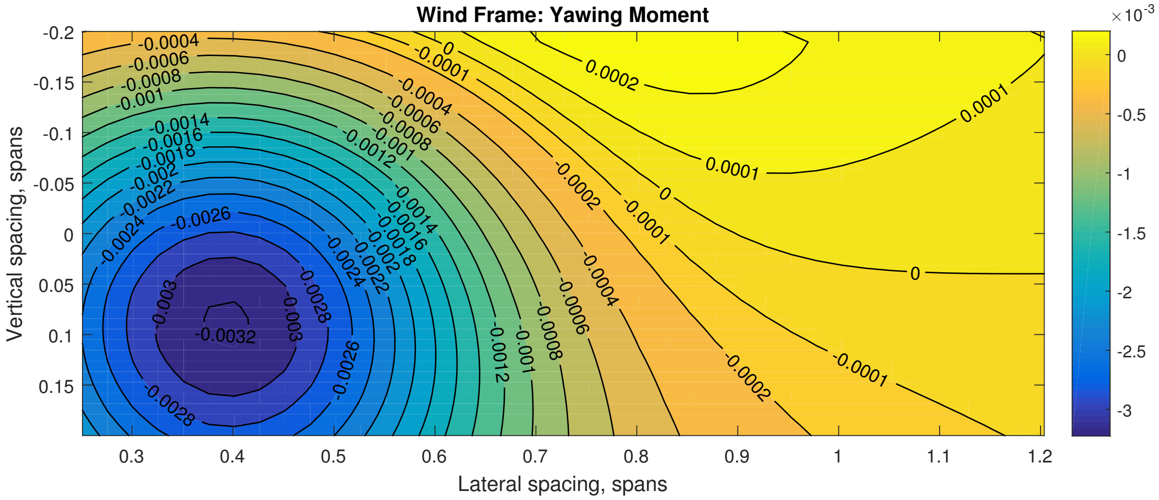
Wind Frame: Yawing Moment

Figure 3.10. Yawing Moment Coefficient Simulation Results for the Full F-15E Heavy Tanker Case.

Figures 3.10 and 3.11 show the induced yawing moment coefficient and induced side force coefficient, respectively, for the heavy tanker full F-15E case. The yawing moment plot is very similar to that of the F-15C case in that the magnitudes for the yawing moment are small near the sweet spot and the shape of the contours is nearly

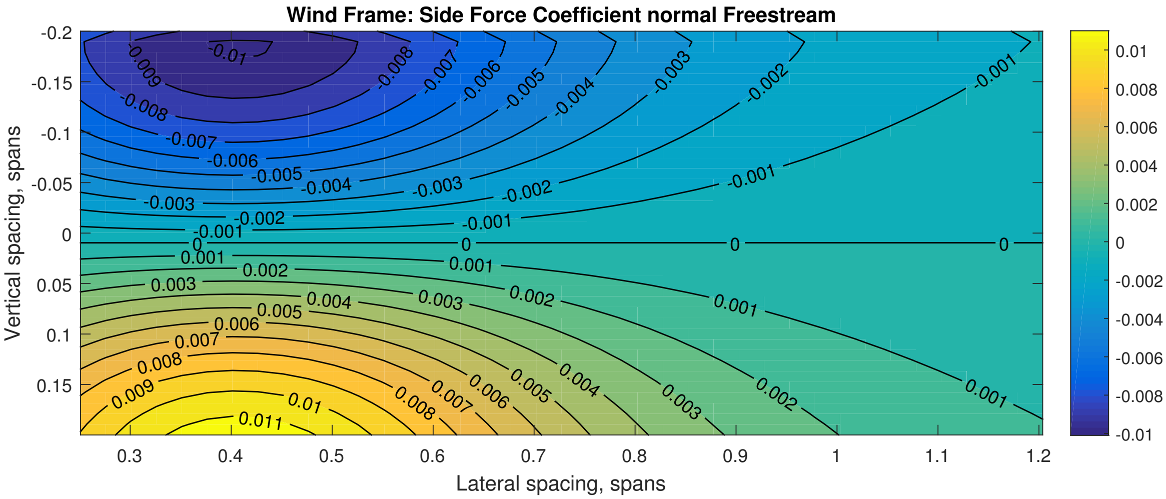

Figure 3.11. Side Force Coefficient Simulation Results for the Full F-15E Heavy Tanker Case.

the same. The induced side force coefficient plot is nearly identical for the F-15C and F-15E due to both aircraft having the same geometry. There is only a very small difference in magnitude, which can be explained by the two aircraft having different pitch angles due to different weights

3.1.3 Static Sweet Spot Summary

A summary of the static sweet spot results is provided in Table 3.1. The results show that the sweet spot location is independent of receiver weight, however the receiver weight does have an effect on the magnitude of the increase in lift-to-drag ratio. A lighter receiver obtains a larger increase in lift-to-drag ratio, which explains why the lift-to-drag ratio increases are smaller for the F-15E, because the F-15E is essentially a heavier F-15C (the only difference being a small difference in $C_{D,0}$ and weight). The results also show that the static sweet spot does depend on the tanker weight. As the tanker gets lighter the sweet spot moves inboard. The increase in lift-to-drag ratio also reduces. At the static sweet spot location moving up or down one grid point vertically has almost no impact on the magnitude of the lift-to-drag ratio.

Table 3.1. Static Sweet Spot Summary

Tanker	Receiver		Sweet Spot		
Aircraft Mass	Type	Fuel Mass	Position [tanker wingspan]		L/D Increase [%]
			Y	Z	
Heavy	F-15C	Full	0.7272	0.0102	31.95
		Empty	0.7272	0.0102	40.40
	F-15E	Full	0.7272	0.0102	23.97
		Empty	0.7272	0.0102	33.11
Light	F-15C	Full	0.6771	0.0102	27.21
		Empty	0.6771	0.0102	34.38
	F-15E	Full	0.6771	-0.0084	20.46
		Empty	0.6771	0.0111	28.21

Moreover, the results show that the rolling moment coefficient contour plots are almost exactly the same for same tanker configurations, regardless of F-15 type and fuel amount. The small differences can be attributed to the difference in the trim pitch angles (the F-15E is heavier and has a higher trim pitch). Similarly, the yawing moment coefficient contour plots are almost exactly the same for same tanker configurations, regardless of F-15 type and fuel amount. Again, the small differences should be due to the difference in trim pitch angles. The side force coefficient exhibits the same behaviour as the rolling moment coefficient. Unlike the induced rolling moment and side force coefficients, however, the yawing moment difference seems to slightly depend on the relative position as well. The change in pitching moment coefficient at the sweet spot depends heavily on the receiver weight. With the lightest receiver and heaviest tanker the change in pitching moment coefficient is 189%, whereas with the heaviest receiver and heaviest tanker it is only 103%.

Tanker weight affects all parameters. With increasing tanker weight all force and moment coefficients are increased. The tanker weight also affects where the maxima for the moment coefficients are. With increasing weight, the maximum locations are moved outboard. Interestingly, the zero rolling moment coefficient line and maximum pitching moment coefficient location moves outboard at the same rate as the static sweet spot.

3.2 Dynamic Sweet Spot Simulations

The dynamic simulation is analogous to an actual flight. The purpose of this analysis is to change the commanded position of the receiver aircraft to determine the required thrust variation over a grid, similar to the one used in the static sweet spot simulations. As the induced forces and moments change with the relative position, the controller retrims the follower aircraft at each commanded position. The wind is turned on after 5 seconds of flight and the simulation is run until steady-state trimmed flight is obtained. During the dynamic sweet spot simulations, the fuel burn is turned off to ensure that the mass of the receiver and tanker do not vary between grid points, since the settling time varies between commanded positions. The last value of the simulation (representative of the trim condition) for all control effectors is saved and the data is visualized on a contour plot. The process is repeated for all points in the grid defined in Section 3.1. An extended grid, shown in Fig. 3.12, ranging from 0 spans to 1.2 spans laterally is used for the full F-15C, full KC-135R case to characterize the effect of the wind in the refueling position.

3.2.1 F-15C

The dynamic simulation for the F-15C is run for the same 4 cases defined in Section 3.1.

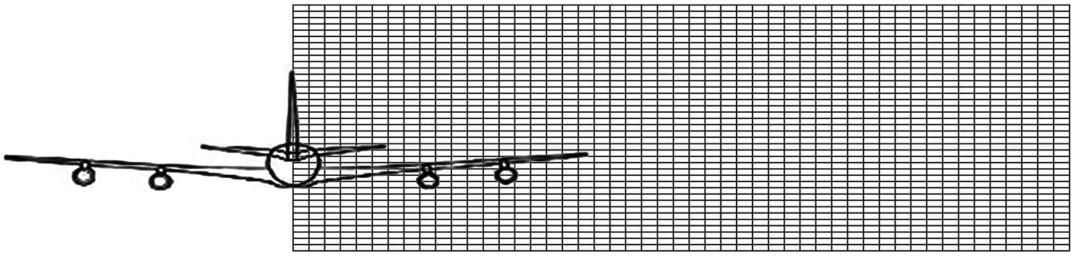

Figure 3.12. Depiction of Extended Grid.

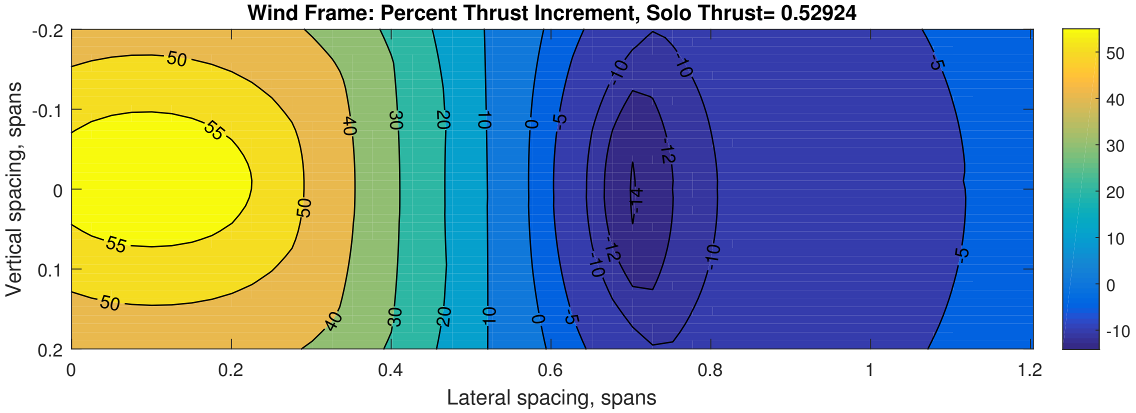

Figure 3.13. Thrust Increment Simulation Results for the Full F-15C Heavy Tanker Case.

Figure 3.13 shows the change in thrust due to the flow field for the heavy tanker full F-15C case. The dynamic sweet spot is located 0.7022 spans laterally from the tanker and at the same altitude as the tanker. A comparison with the rolling moment variation in Fig. 3.3 reveals that the dynamic sweet spot coincides with the zero rolling moment coefficient line. The decrease in thrust is 14.15% at the sweet spot when compared to solo flight. The decrease in thrust is much lower than the increase in lift-to-drag ratio. This is due to extra control surface deflections necessary to trim the aircraft. The refueling position is at the bottom left corner of the grid. The

F-15C requires 44% more thrust to fly at the refueling position compared to that in solo flight.

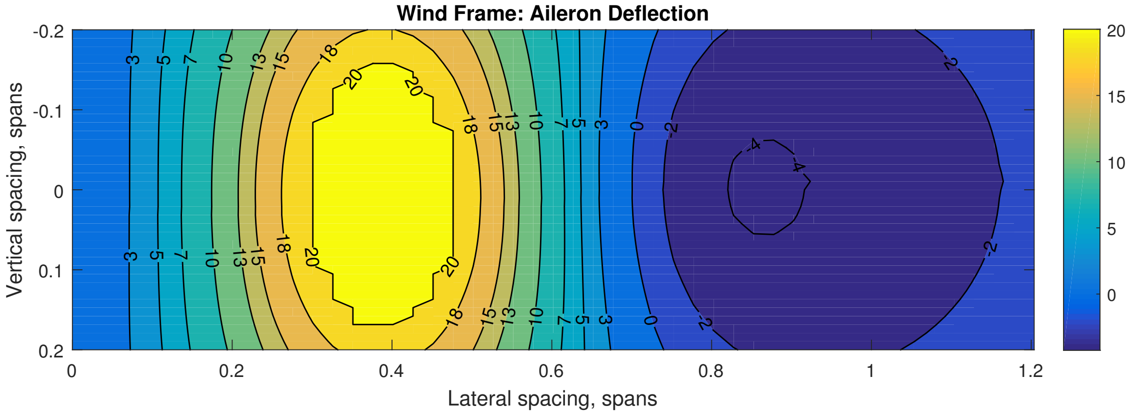

Figure 3.14. Aileron Deflection Simulation Results for the Full F-15C Heavy Tanker Case.

Figure 3.14 shows the aileron deflections necessary to trim the aircraft at each grid point for the heavy tanker full F-15C case. At the dynamic sweet spot the aileron deflection necessary is only −0.1°, which causes very little trim drag. There is a region where the aileron deflection saturates, but the F-15C is still trimmed, since the additional differential tail deflections provide the necessary roll control. At the refueling position the aileron deflections are essentially zero since there is no induced rolling moment at that location.

Figure 3.15 shows the rudder deflections necessary for trim at each grid point for the heavy tanker full F-15C case. At the dynamic sweet spot, the required rudder deflection is 0.28 deg, which causes very little trim drag. As discussed in section 3.1.1 the yawing moment coefficient is very small throughout the grid, which explains why the maximum rudder deflection shown in the contour plot is only 2 deg. At the refueling position, the rudder deflections are essentially zero.

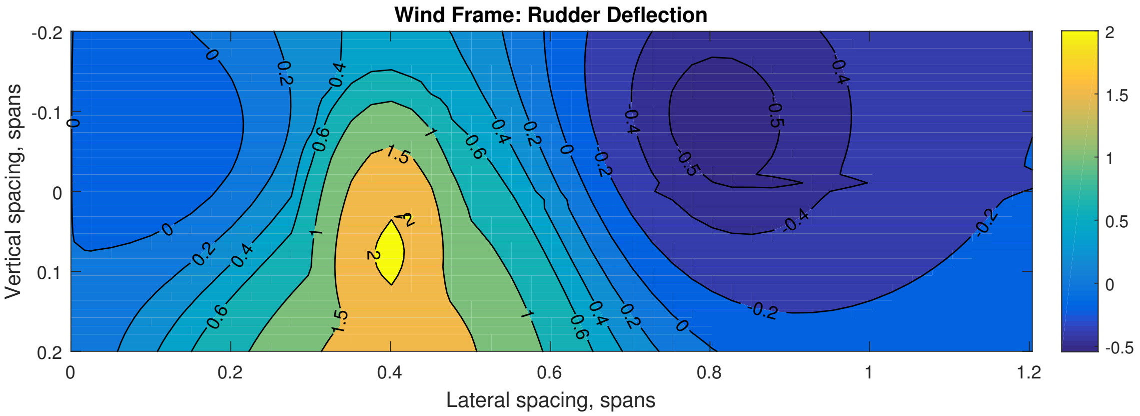

Figure 3.15. Rudder Deflection Simulation Results for the Full F-15C Heavy Tanker Case.

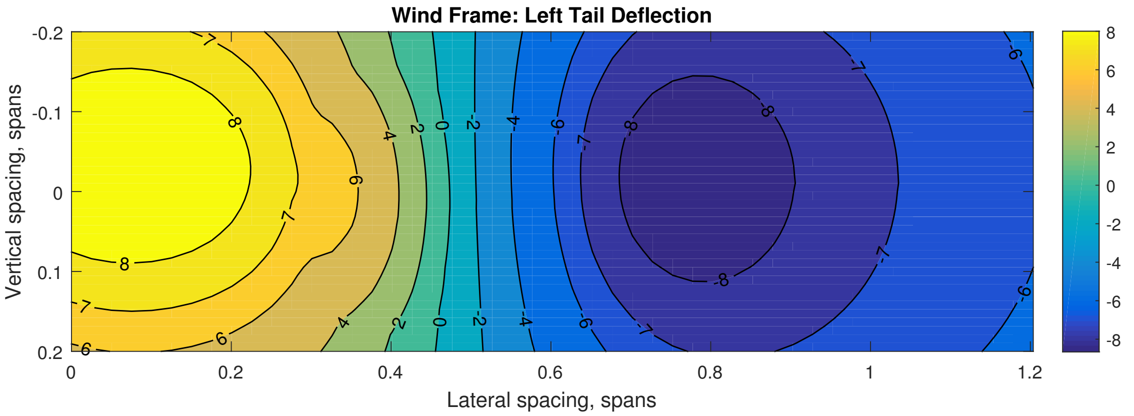

Figure 3.16. Left Tail Deflection Simulation Results for the Full F-15C Heavy Tanker Case.

Figures 3.16 and 3.17 show the left and right tail deflections necessary to fly at each grid point for the heavy tanker full F-15C case. The dynamic sweet spot is located in the region of maximum deflection for both the left tail and the right tail, which can be explained by the high induced pitching moment in that area, shown in Fig. 3.4. The high tail deflections in that area cause the reduction in benefit when comparing static sweet spot results to dynamic sweet spot results. The excursions seen in the 6 deg contour line of the left deflection and in the -7 deg contour line of

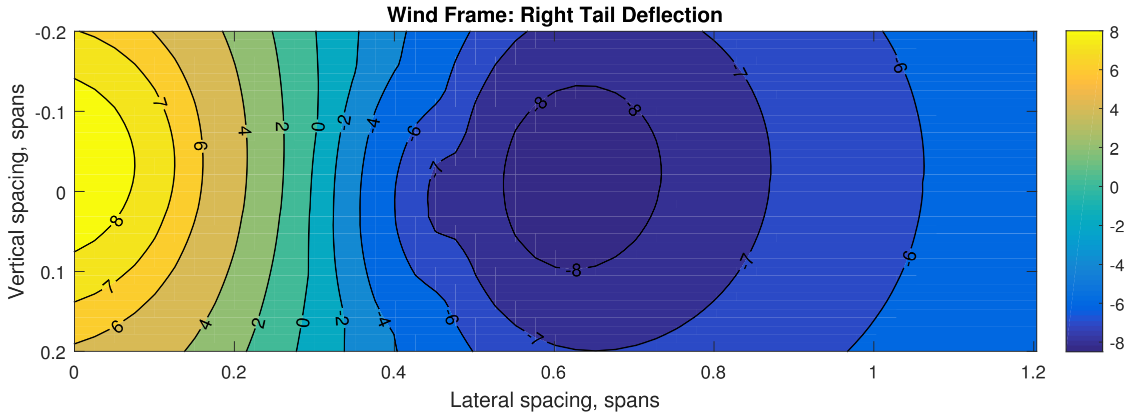

Figure 3.17. Right Tail Deflection Simulation Results for the Full F-15C Heavy Tanker Case.

the right deflection correspond to the region where the aileron saturates as shown in Fig. 3.14.

3.2.2 F-15E

The dynamic simulation for the F-15E is run for the same 4 cases defined in Section 3.1.

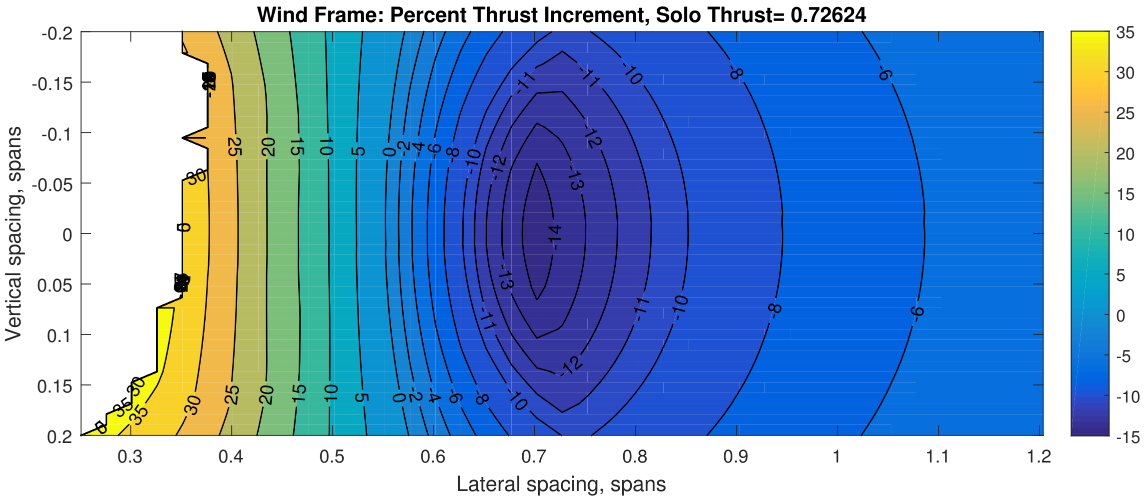

Figure 3.18. Thrust Increment Simulation Results for the Full F-15E Heavy Tanker Case.

The dynamic results of the full F-15E heavy tanker case are very similar to those of the full F-15C heavy tanker case. Fig. 3.18 shows the change in thrust for the full F-15E heavy tanker case. The dynamic sweet spot is at the same location as it is for the full F-15C heavy tanker case. The decrease in thrust at the sweet spot (14.53%), however, is larger than that of the F-15C, contrary to the lift-to-drag ratio increase, which was larger for the F-15C. The blank area in Fig. 3.18, on the left, laterally close to the tanker, indicates a region where the aircraft could not be stabilized. Inspection of the contour plots of all control variables reveals that the aircraft does not have enough thrust available before it saturates at the maximum available thrust. Recall from Fig. 3.13 that the F-15C thrust requirement goes up more than 40% when it flies at the lateral position of 0.3 wing spans. As it laterally moves closer, the required thrust goes up to 55% more than the solo thrust requirement, which is 53% of the maximum available thrust. In the case of the full F-15E, the solo required thrust is already 73% of the maximum available thrust. As it laterally moves closer to the tanker (closer than 0.35 tanker wingspan), the required thrust exceeds the maximum available thrust and thus the thrust saturates. In the simulation, the maximum available thrust is set based on the data available for Pratt and Whitney F100-PE-220 engines. If General Electric F110-GE-129 engines were used, which increase the maximum available thrust from 6000 lb to 6875 lb per engine, the blank region will disappear as the aircraft will have enough maximum available thrust. Further, this specific result directly depends on the drag model of the aircraft. The aerodynamic model might be overestimating the drag. If that is the case, a more accurate drag model may also eliminate this issue observed in the simulation.

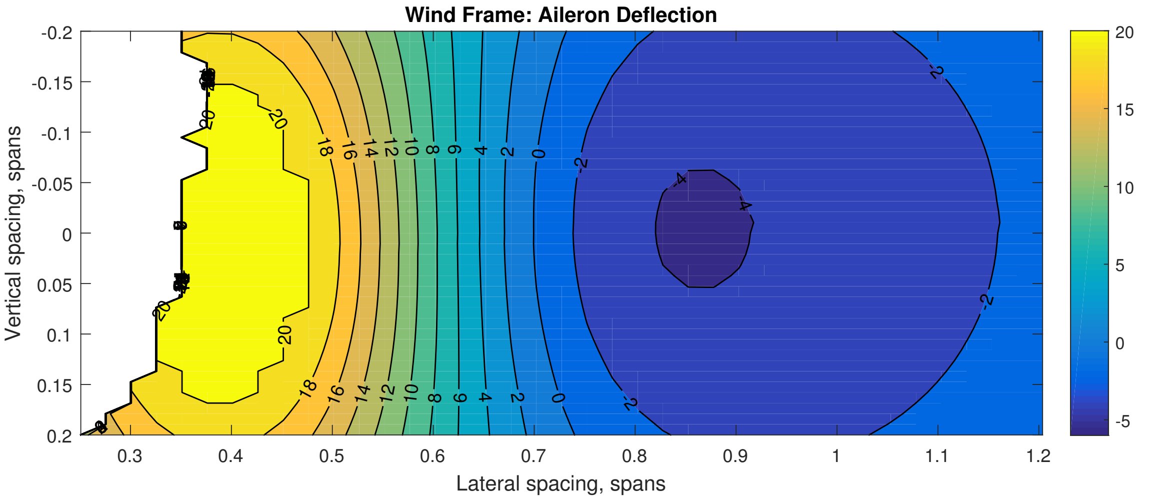

Figure 3.19. Aileron Deflection Simulation Results for the Full F-15E Heavy Tanker Case.

Figure 3.19 shows the aileron deflection necessary to fly at each grid point for the heavy tanker full F-15C case. The contour is very similar to that of the full F-15C heavy tanker case.

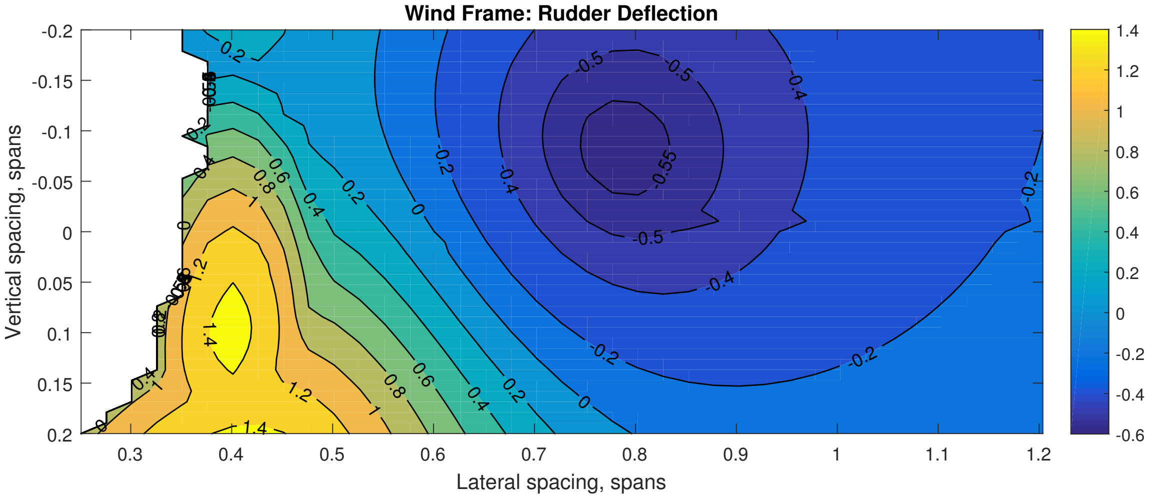

Figure 3.20. Rudder Deflection Simulation Results for the Full F-15E Heavy Tanker Case.

Figure 3.20 shows the rudder deflection necessary to fly at each grid point for the heavy tanker full F-15C case. The contour only varies in magnitude compared the full F-15C heavy tanker case. The magnitude of the rudder deflections is only slightly higher for the F-15E, as compared to the F-15C results.

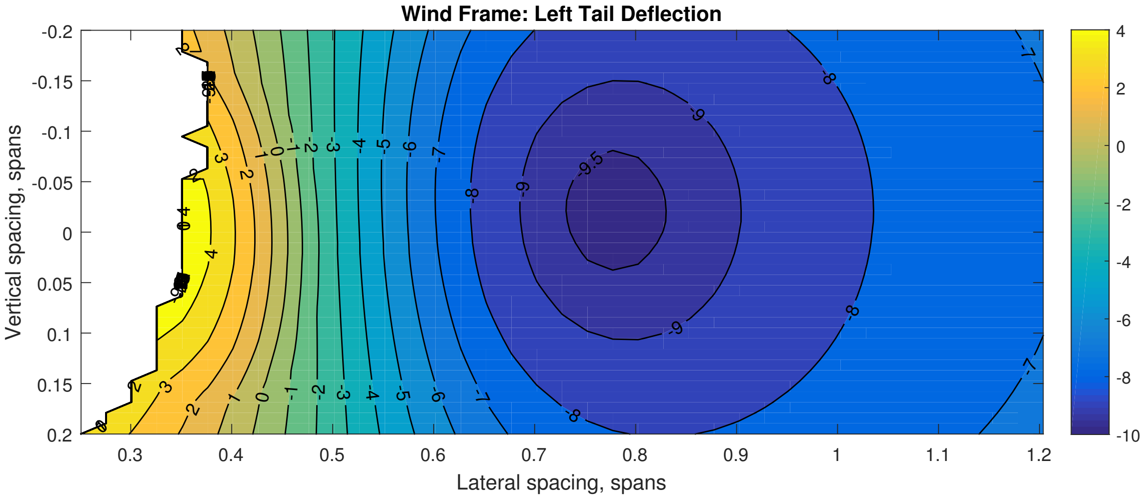

Figure 3.21. Left Tail Deflection Simulation Results for the Full F-15E Heavy Tanker Case.

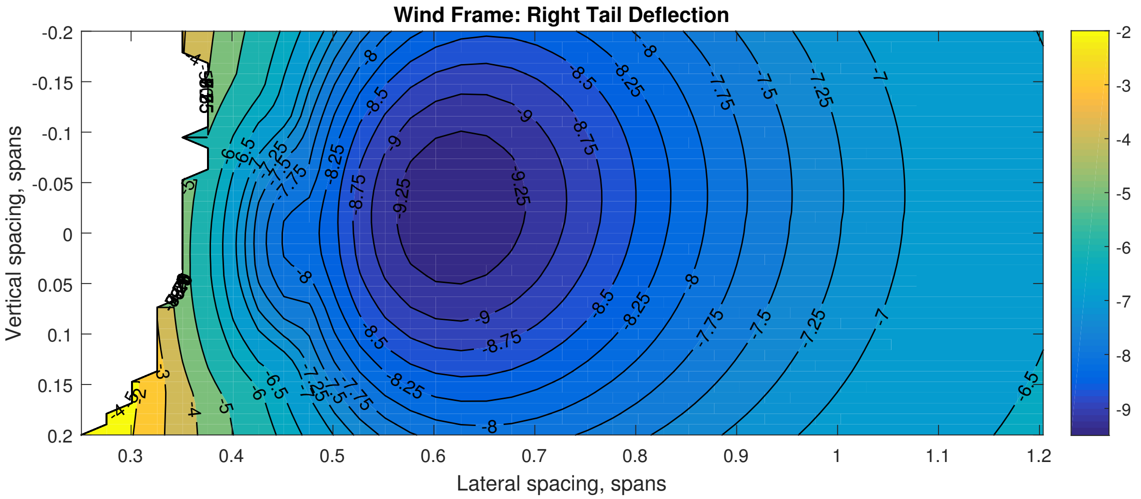

Figure 3.22. Right Tail Deflection Simulation Results for the Full F-15E Heavy Tanker Case.

Figures 3.16 and 3.17 show the left and right tail deflections necessary to fly at each grid point for the heavy tanker full F-15C case. The tail deflections are similar to the F-15C case.

3.2.3 Dynamic Sweet Spot Summary

A summary of the dynamic sweet spot results is provided in Table 3.2. The results are similar to the static sweet spot results in that the sweet spot location is independent of receiver weight and only depends on the tanker weight. The dynamic sweet spot moves inboard at the same rate as the static sweet spot as the tanker gets lighter. The dynamic sweet spot stays at the zero induced rolling moment coefficient line. The thrust reduction is much smaller than the increases in lift-to-drag ratio due to extra control surface deflections.

Table 3.2. Dynamic Sweet Spot Summary

Tanker	Receiver		Sweet Spot		
Aircraft Mass	Type	Fuel Mass	Position [tanker wingspan]		Thrust Reduction [%]
			Y	Z	
Heavy	F-15C	Full	0.7022	0	14.15
		Empty	0.7022	0	12.59
	F-15E	Full	0.7022	0	14.53
		Empty	0.7022	0	13.37
Light	F-15C	Full	0.6520	0	12.35
		Empty	0.6520	0.0105	10.92
	F-15E	Full	0.6520	0	12.73
		Empty	0.6520	0	11.64

CHAPTER 4

CORONET MISSION SIMULATIONS

4.1 Overview

Various full coronet mission simulations are performed to quantify the benefit of flying at the sweet spot. The simulation results are used to answer the specific questions posed earlier for coronet missions: (1) amount of fuel to be saved, (2) number and frequency of refueling, and (3) possibility of eliminating a tanker aircraft from missions involving multiple tankers. Coronet missions are simulated with different type and number of receiver aircraft escorted by a KC-135R: (1) one F-15C, (2) two F-15C, (3) one F-15E, and (4) two F-15E. Each receiver case is simulated twice with the receiver flying at two different "formation positions": (1) formation position is out of the tanker's wake, (2) formation position at the sweet spot. The former is the simulation of current practice in coronet missions where the fighter aircraft fly in formation with the tanker, but outside the tanker's wake. The latter is to simulate the proposed alternative where the fighters fly at sweet spot to benefit from "surfing" the wake of the tanker. The comparison of results from the former and the latter will help answer the questions stated above.

Table 4.1. Coronet Mission Starting Mass

	KC-135R	F-15C	F-15E
Full Mass [kg]	146,280	25,556	34,251
Max Fuel Mass [kg]	92,156	5,394	9.684
Initial Mass / Max Mass	88%	100%	100%
Initial Fuel / Max Fuel	81%	100%	100%

Simulations start when the fighter aircraft are at the formation position, at the sweet spot or out of the wake, with the mass and fuel configuration specified in Table 4.1. In this chapter, the sweet spot is considered a fixed position relative to the tanker throughout the simulation even though the actual sweet spot moves inboard as the tanker weight decreases. The sweet spot for the coronet missions in this chapter is the one determined when the tanker and the receiver aircraft are at their heavy mass configurations as specified in Section 2.5. Since the sweet spot change with the tanker weight is not tracked in the simulations to be presented herein, the formation benefit in terms of the fuel saved will be less than the full potential. Later, in Chapter 6, the additional benefit of tracking the sweet spot position through the flight will be investigated. The formation position out of the wake is also a fixed position relative to the tanker.

Table 4.2. Coordinates of Formation Positions in Tanker Body Frame [m]

	x	y	z
Refueling Position	-24.9936	0	7.8433
Observation Position	-40.2336	60.9600	7.8433
Sweet Spot	-152.4000	28.0016	-5.8053
Formation Position Out of Wake	-152.4000	159.5079	0

The fighter aircraft flies at the formation position (out of the wake or at sweet spot) until the last fuel tank has only 15% fuel left. When this happens, the aircraft is commanded to move to the refueling position to be refueled. The aircraft first moves to the observation position and stays there for half a minute and then moves to the refueling position. The coordinates of the four positions relative to the body frame of the tanker aircraft are given in Table 4.2. Further, Fig. 4.1 illustrates the x and y coordinates of these four points. The aircraft moves between two points in three

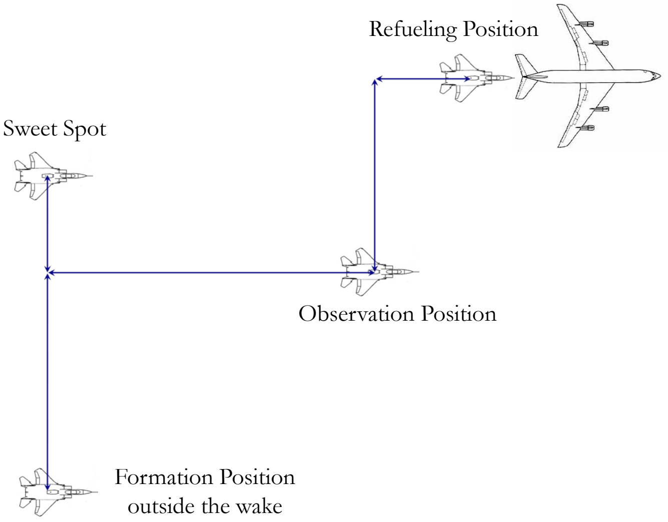

Figure 4.1. Illustration of Formation Positions.

stages, in each of which the aircraft moves along one axis only. The sequence is along z-axis, y-axis, and x-axis if the aircraft is moving for refueling. The commanded speed along x-axis is 2 m/s except when approaching to the refueling position, in which the commanded speed is 1 m/s for F-15C, 0.5 m/s for F-15E. This is to avoid overshooting the refueling position and moving under the tanker aircraft. The commanded speed along y- and z-axes is 1 m/s in all stages. The z-y-x sequence is reversed when the aircraft is moving back to the formation position after all the fuel tanks are filled up. The sequence of tanks to be refueled is based on the refueling schedule given in Section 2.5. These refueling maneuvers are repeated as many times as needed throughout the flight. The simulations stop when the tanker aircraft has 5% fuel left.

A simulation with two fighter aircraft is the same as the one with one aircraft in almost all aspects stated above. The second receiver is considered to be flying at the corresponding formation position on the other side of the tanker. The refueling of the second receiver takes place two minutes after each refueling of the first receiver is completed. In the simulation environment, there is only one full receiver aircraft model. The second full receiver aircraft model is not included in the simulations to avoid the time needed for the development of the simulation as well as additional computation time the second full model would impose. In the simulation environment with a full tanker model and a full receiver model, the second receiver is represented as additional fuel offload from the tanker. Two minutes after each refueling of the full receiver model, the tanker aircraft model offloads the same amount of fuel for the same amount of time. The only error in this approach stems from the fuel burn rate during the fuel transfer. When fuel is flowing from tanker into the receiver, the receiver engines are also burning fuel. This fuel burn rate depends on the strength of the downwash at the refueling position. The downwash strength depends on the weight of the tanker. After the first receiver is refueled, the tanker weight will be lower for the next aircraft to be refueled, which means it will be exposed to relatively weaker downwash, and thus its fuel burn rate should be slightly lower as compared to the first receiver aircraft. This difference will slightly affect the the duration of fuel transfer into the second receiver since the fuel flow rate is the same. The resulted discrepancy is ignored in this approach since this effect is very small in fuel transfer time.

The subsequent section presents a comparison of full missions with an F-15C flying either at the sweet spot or out of the wake in detail. The other cases of the full missions will follow with less detail.

4.2 F-15C Coronet Mission Simulations

This section first presents the single F-15C receiver simulation results, followed by two F-15C simulations. In the figures, case1 is when the receiver flies out of the wake and case2 is when at the sweet spot.

4.2.1 Single F-15C escorted by KC-135R

Figure 4.2 shows the commanded and actual position components of the receiver aircraft relative to the tanker. Figure 4.3 shows the detailed views during the first refueling maneuver. The figures show that the feedback controller can successfully track the commanded trajectory through the wake of the tanker and keep the aircraft at the refueling position during the fuel transfer. It can also be seen clearly from the figures that the receiver aircraft goes to the observation position while moving between the formation position (out of the wake in case1 and at sweet spot in case2). It is also clear that the receiver moves along z-axis, y-axis and x-axis in sequence when moving from formation position to observation position and from observation to the refueling position. When moving from refueling to observation and from observation to the formation position, the reversed sequence is followed, as stated earlier.

Figure 4.4 shows the effective translational and rotational wind components the receiver aircraft is experiencing during the whole mission, and Fig. 4.5 shows the same only during the first refueling. In case2, the W_z component is negative (upwash) when the aircraft is at the sweet spot. W_z in case1 is zero when the receiver is at the formation position, which is out of the wake. Note that the upwash magnitude in case2 is decreasing since the tanker weight and thus the lift decreases. Because of the same reason, the q component of the rotational wind also goes down. W_z in both cases goes to a large positive speed, indicating strong downwash when the receiver moves to the refueling position, right behind the tanker. Contrary to W_z, W_y seems to increase as the tanker loses weight. This can be explained by the fact that these components are in the receiver body frame. Figure 4.6 shows that receiver in case2 flies with small yaw trim increasing slightly until about the 8th hour and staying about constant afterwards. W_y shows the same pattern. Thus, the increase in W_y

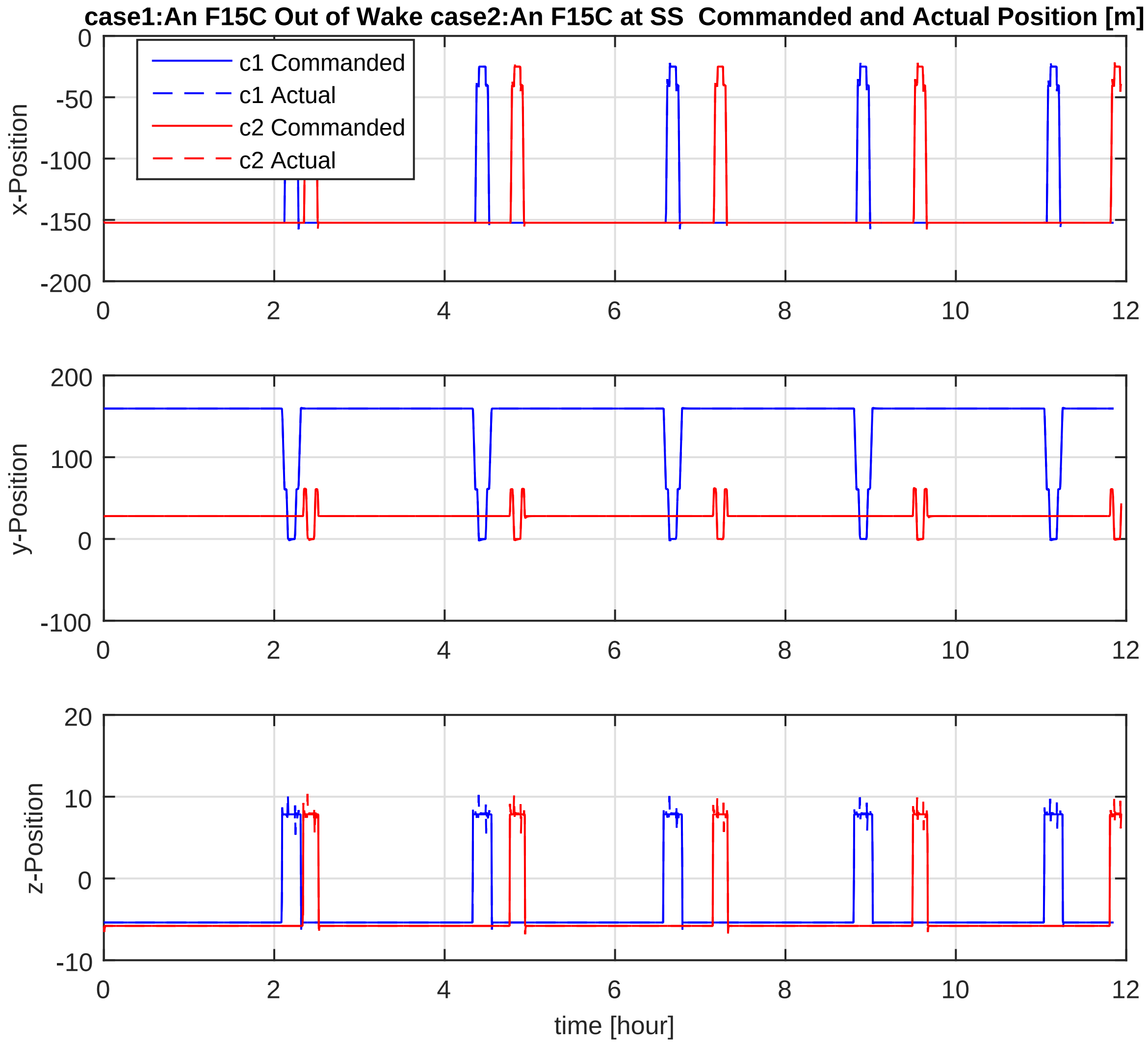

Figure 4.2. Single F-15C Commanded and Actual Position.

is because it is the component of the wind resolved in body frame. Note the large induced rolling moment when the aircraft traverses the wake laterally.

Figure 4.6 shows the Euler angles, angle of attack and side slip angle of the receiver aircraft during the whole mission, and Fig. 4.7 shows the same only during the first refueling. The figure also shows the detailed views during the first refueling maneuver. At the sweet spot, the receiver aircraft is trimmed with small a yaw and

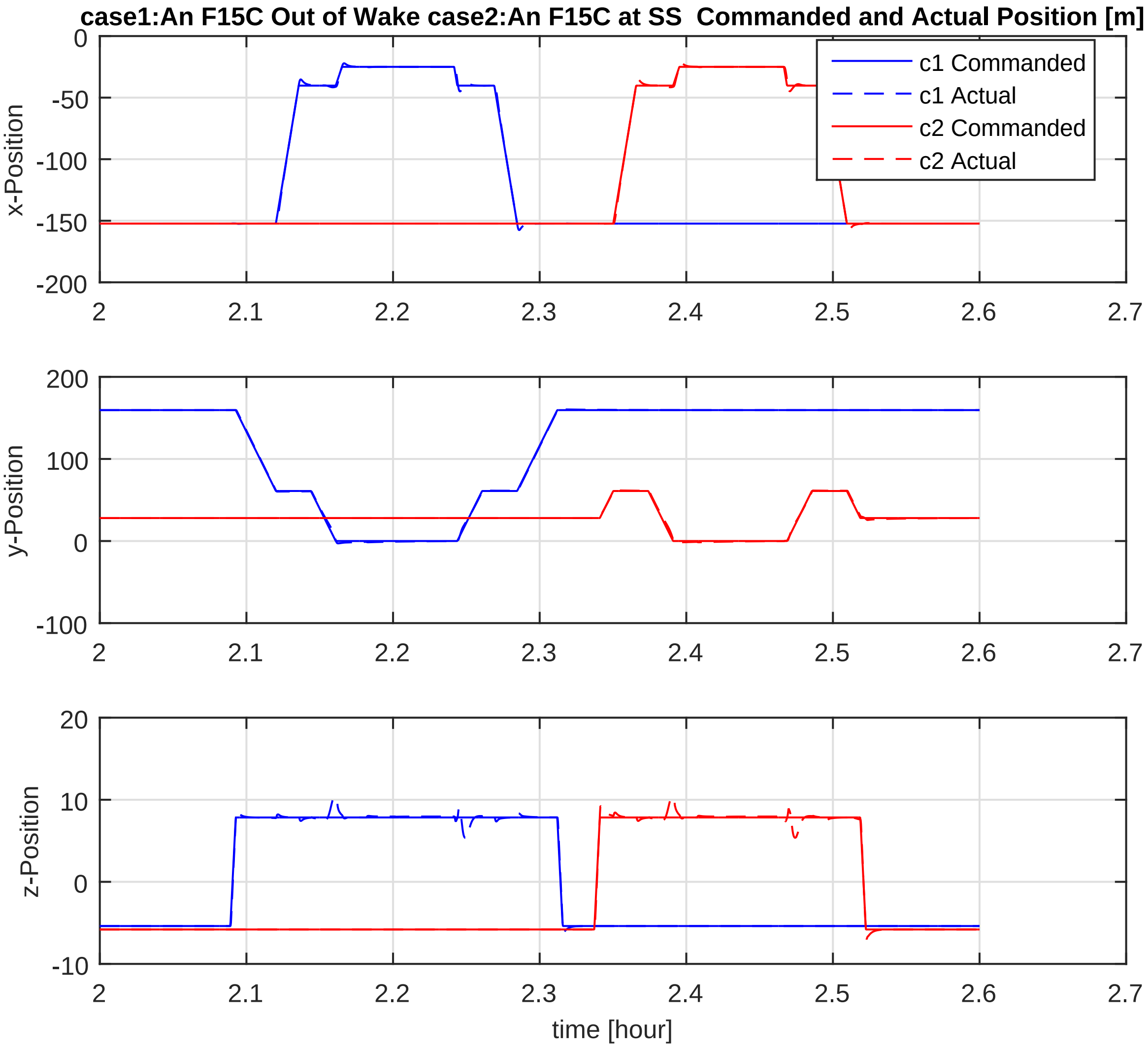

Figure 4.3. Single F-15C Commanded and Actual Position - zoomed in during the first refueling.

bank angles. Both angle of attack and pitch angle decrease as the aircraft loses weight and they increase again after each refueling. When at the sweet spot, the angle of attack is higher than the pitch angle, which is due to the upwash. In case2, the angle of attack and pitch angles are the same since the aircraft is out of the wake. The angle of attack is lower than the pitch angle when the aircraft moves to the refueling position where the aircraft is exposed to downwash in both case1 and case2.

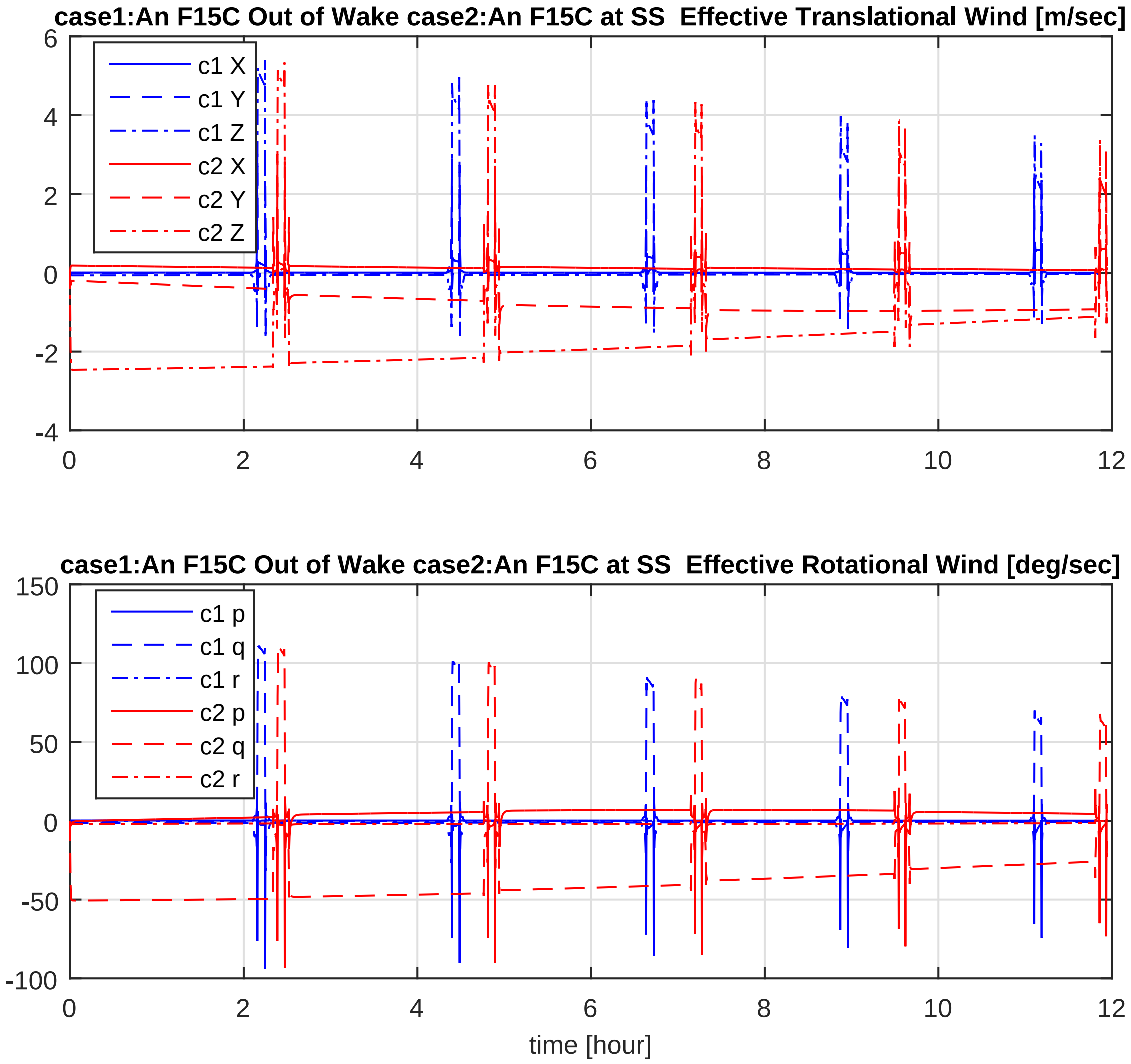

Figure 4.4. Single F-15C Wind.

Figure 4.8 shows the control variables of the receiver aircraft in both cases during the whole mission, and Fig. 4.9 shows the same only during the first refueling. The aileron and rudder stay zero when the aircraft is at the cruise condition out of the tanker's wake in case1. The aileron and rudder are used to move the aircraft to and from the refueling position. The aileron and rudder deflections of the receiver in case2 when flying at the sweet spot are small since the induced roll and yaw moments are very small at the sweet spot. The horizontal tail deflection in both

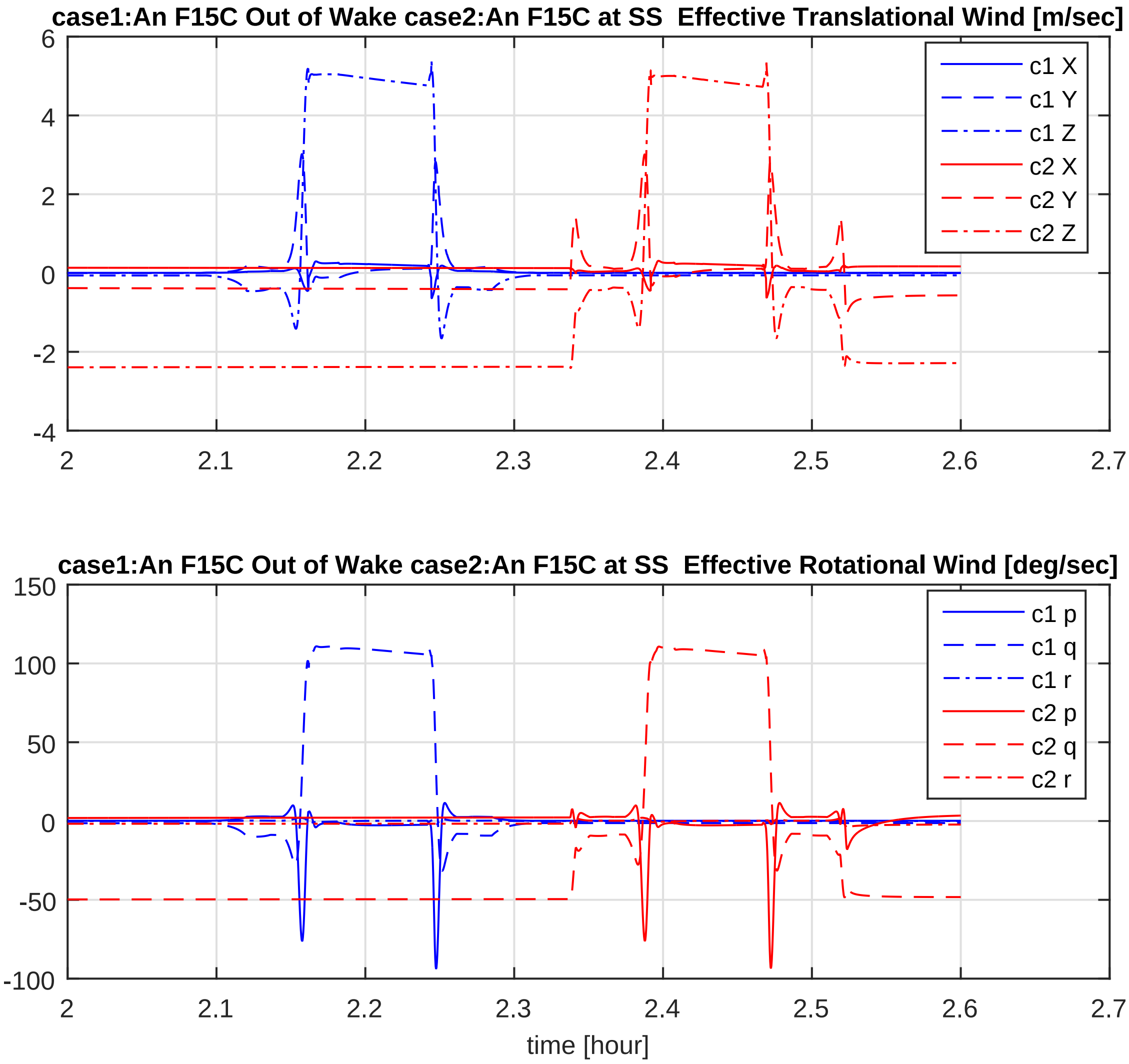

Figure 4.5. Single F-15C Wind - zoomed in during the first refueling.

cases stays in the negative region during the whole flight except when the aircraft moves to the refueling position. The tail deflection in case1 when the receiver is at the sweet spot is higher than that in case2 when the aircraft is flying out of the wake. This is because at the sweet spot, the aircraft is exposed to additional aerodynamic pitching moment induced by the tanker's wake. The induced pitching moment in the downwash region at the refueling position reverses sign, which explains why the tail deflection goes positive at the refueling position. The small difference in the

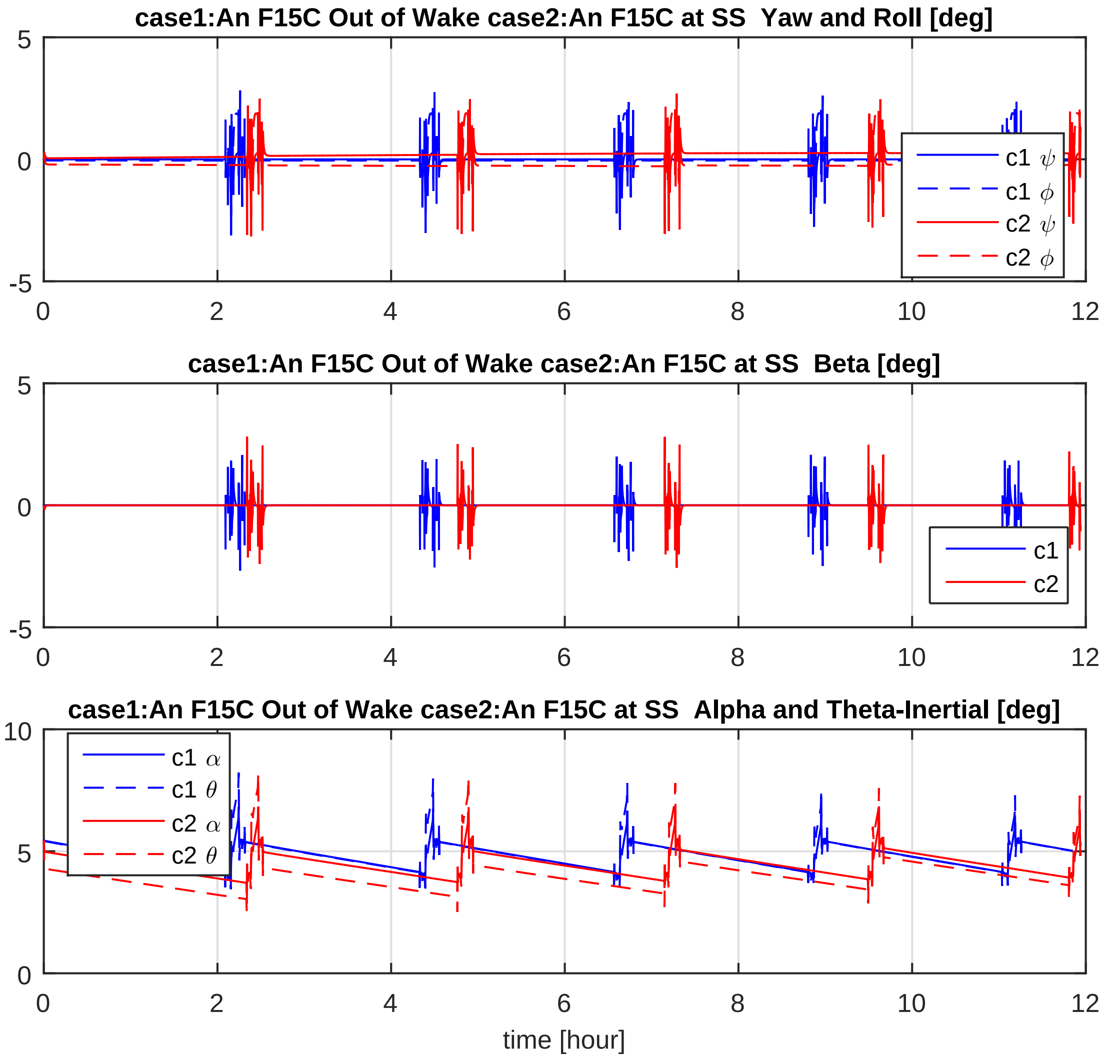

Figure 4.6. Single F-15C Euler Angles, Angle of Attack and Side Slip Angle.

left and right tail deflections in case2 is because the controller is set up such that the differential tail is used along with aileron (differential tail is 30% of the aileron deflection) to generate rolling moment in general and to counter the small induced rolling and yawing moments in this specific case. The receiver thrust decreases as it becomes lighter by burning fuel. When the receiver moves to the refueling position before the fuel transfer is initiated, the thrust goes up significantly. This is because the aircraft now flies in the downwash region of the tanker wake and this requires

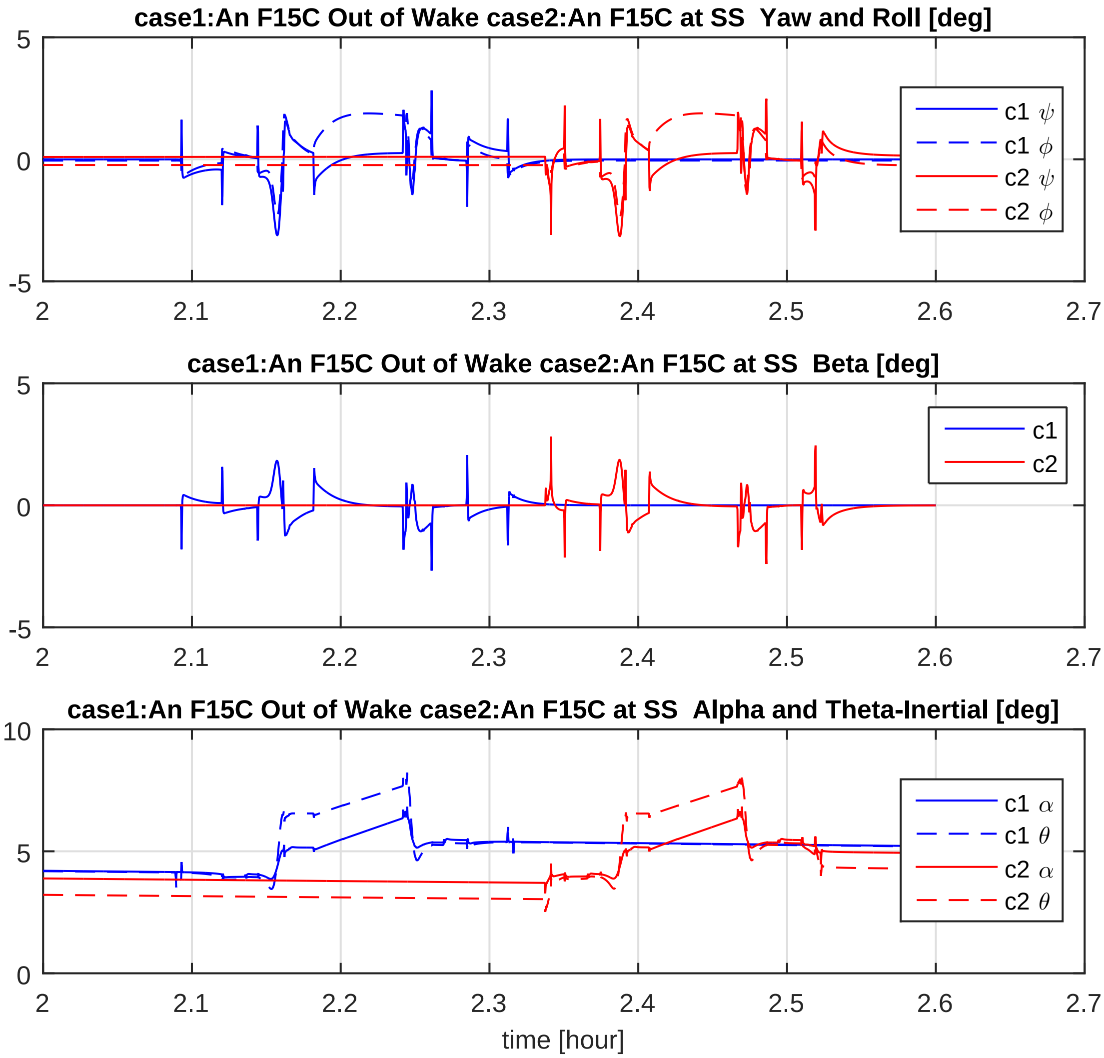

Figure 4.7. Single F-15C Euler Angles, Angle of Attack and Side Slip Angle - zoomed in during the first refueling.

higher thrust level to maintain the relative position. During the fuel transfer, the thrust goes further up as the aircraft weight increases. Comparing the receiver thrust in case1 and case2 manifests the benefit of formation flight. The thrust in case2 where the receiver flies at the sweet spot is lower than that when the aircraft flies out of the wake in case2. As stated previously, this is because at the sweet spot the aircraft is exposed to upwash, which reduces the level of required thrust. As the tanker weight decreases, the upwash becomes weaker and thus the formation flight benefit decreases. This can be seen by the fact that the thrust of case2 shifts up and gets closer to the case1. The thrust of case2 is higher than in case1 only during the refueling of case2 where the aircraft is in the strong downwash region while the aircraft in case1 is flying out of the wake. The thrust required gets close to the maximum available thrust when the aircraft moves to and from the refueling position.

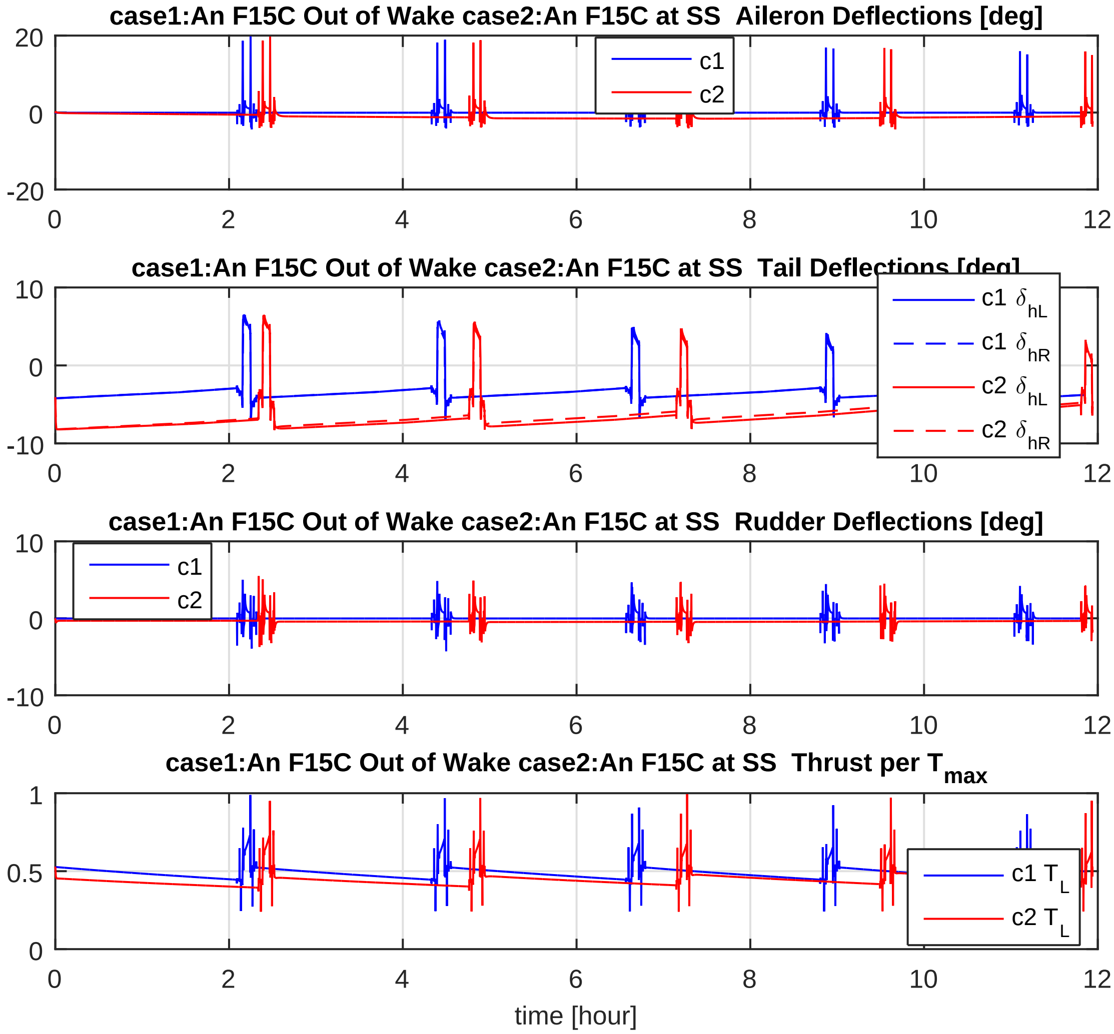

Figure 4.8. Single F-15C Receiver Control Variables.

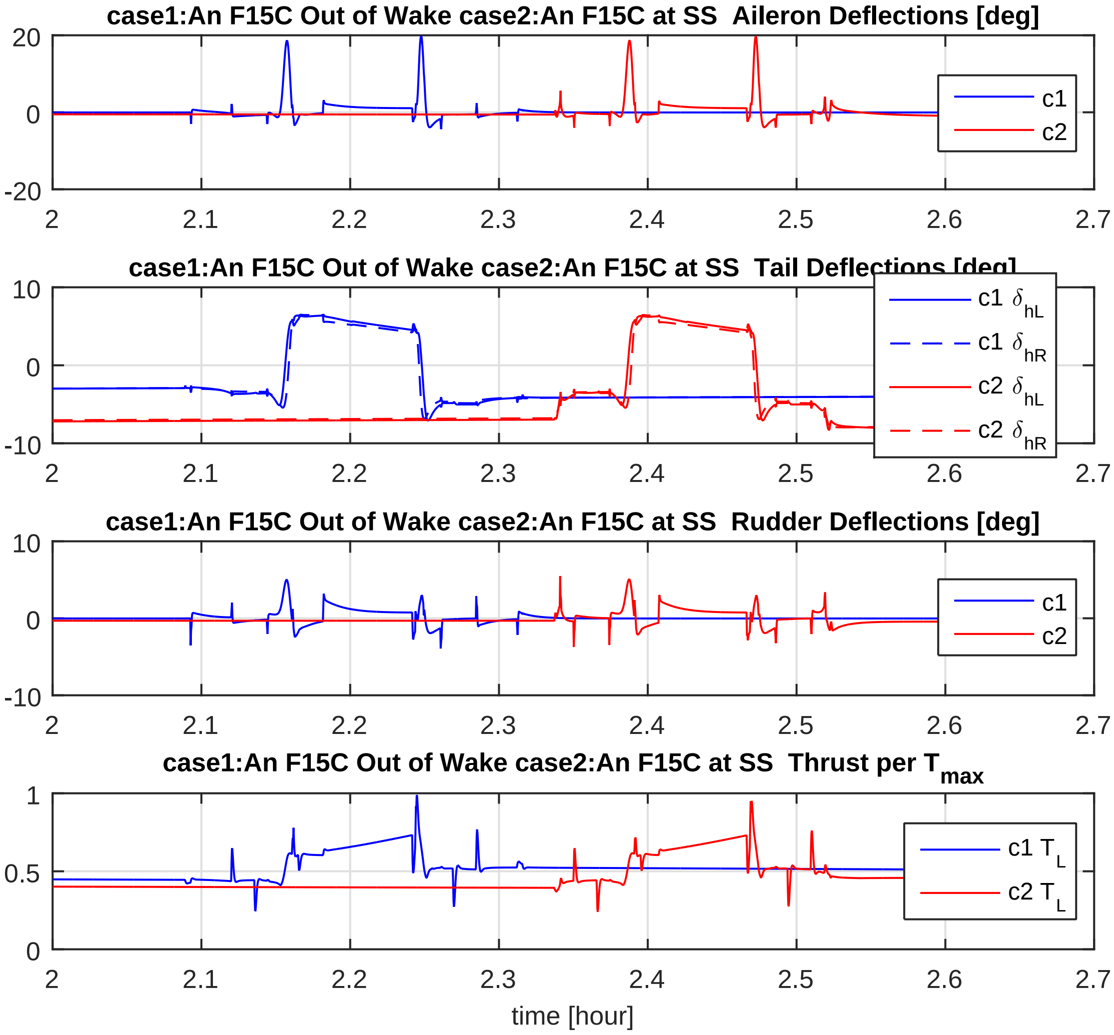

Figure 4.9. Single F-15C Receiver Control Variables - zoomed in during the first refueling.

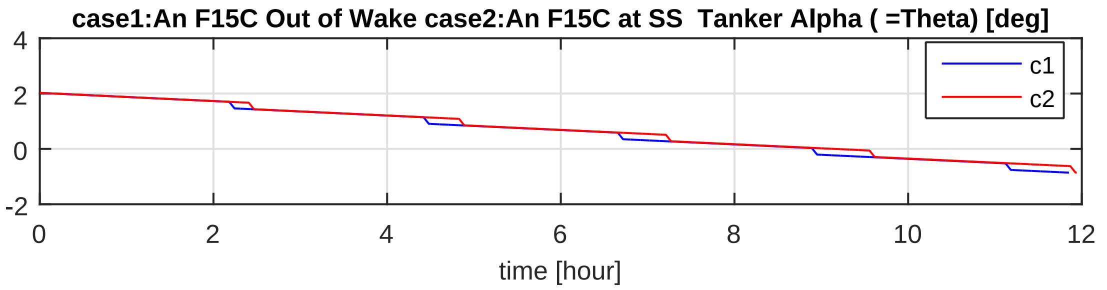

Figure 4.10. Single F-15C Angle of Attack.

Figure 4.10 shows the angle of attack of the tanker (the pitch angle is equal to the angle of attack as the tanker flies in cruise condition with no wind). At the start of the simulation, the angle of attack is 2 deg. As the fuel is lost and the aircraft becomes lighter, the angle of attack decreases. In the last three hours when it is very light, the aircraft flies with small negative angles of attack.

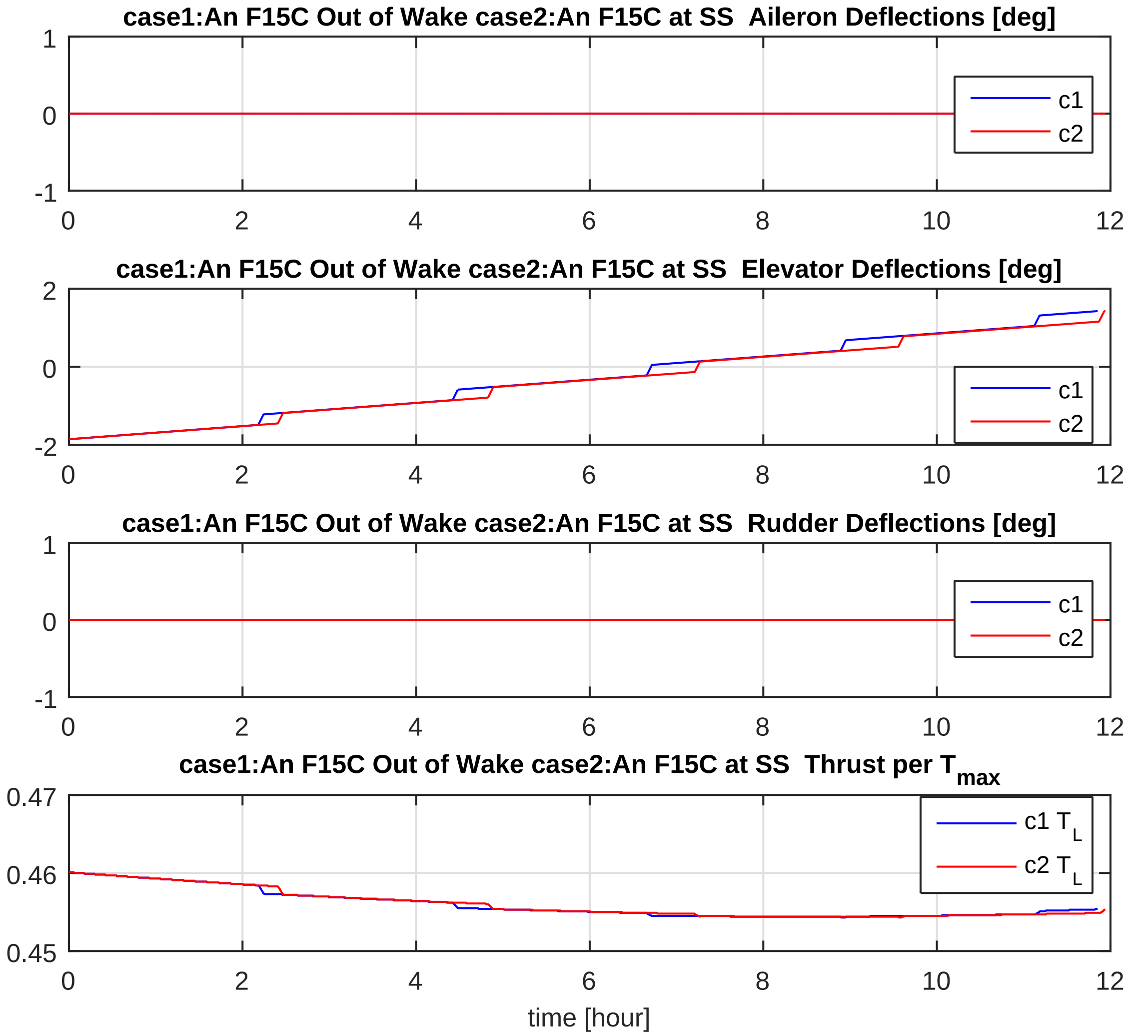

Figure 4.11. Single F-15C Tanker Control Variables.

Figure 4.11 shows the control variables of the tanker. The aileron and rudder deflections stay zero as the tanker stays in the cruise condition throughout the simulation. The elevator starts with -2 deg deflection and increases as the aircraft weight decreases. At the seventh hour of the flight, the elevator deflection turns positive. The required thrust shows the same trend as the fuel burn rate shown earlier as the relation is linear.

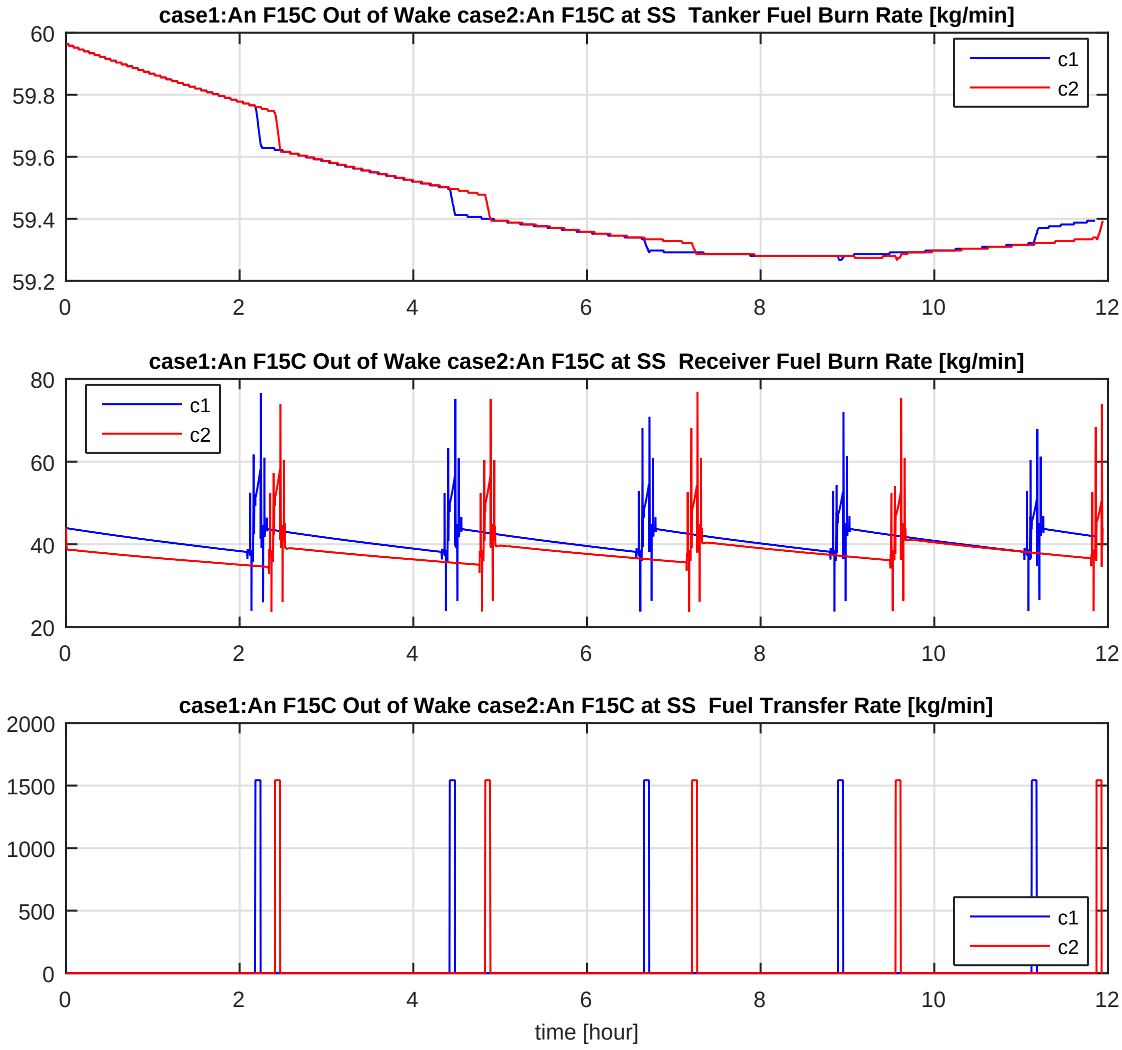

Figure 4.12. Single F-15C Tanker and Receiver Fuel Burn Rate.

Figure 4.12 shows the tanker and receiver fuel burn rates. The tanker fuel burn rate is close to 60 kg/min throughout the flight. In the first 8 hours of the flight, the fuel burn rate decreases very slightly. After that, it shows a minor increase. The relatively abrupt changes in tanker fuel burn rate occur when the tanker off-loads fuel during the refueling of the receiver aircraft. The receiver fuel burn rate has the same pattern as the thrust, shown previously since the relation is linear.

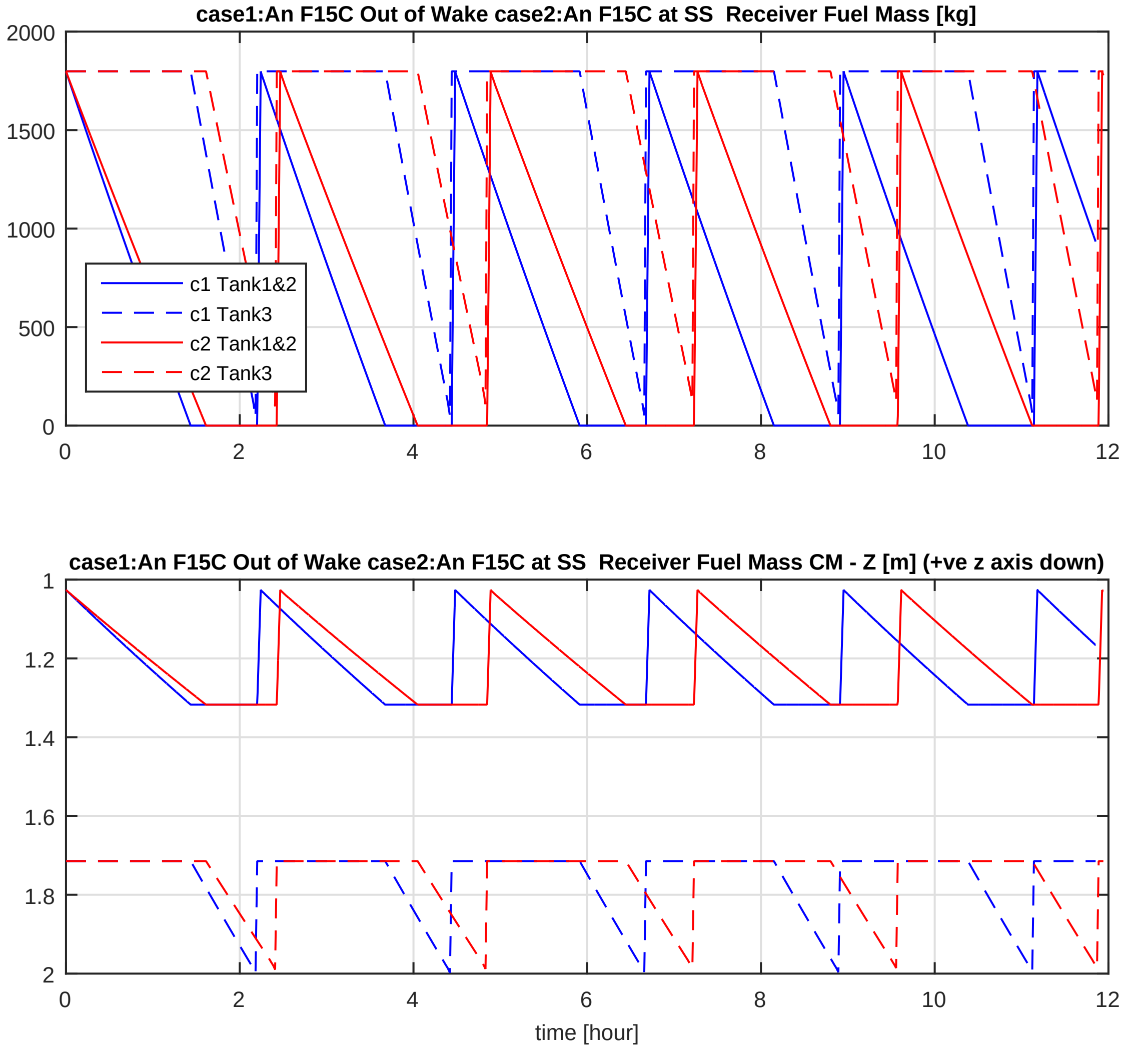

Figure 4.13. Single F-15C Fuel Amount and Fuel Center of Mass.

Figure 4.13 shows the fuel amount and z-coordinate of the fuel center of mass (cm) in each fuel tank. Since tanks 1 and 2 are used and refueled together, change in their fuel amount and cm location in tank 3 is twice as fast. A comparison of the fuel amount in the fuel tanks between case1 and case2 also shows that case2 fuel amounts decrease slower than those of case1. This is because in case2 the aircraft flies at the sweet spot and thus burns less fuel. A closer look at the amount of fuel left in tank 3 right before the fuel transfer starts reveals that less fuel is left in tank 3 in case1 as compared to case2. This is because the refueling maneuver starts when 15% fuel is left in tank 3 in both cases. Since the aircraft in case1 is further away from the refueling position, it takes longer to reach the refueling position and thus burns more fuel.

Figure 4.14 shows the receiver aircraft mass and change in cm location. A comparison between case1 and case2 aircraft mass indicates again the fact that fuel is burned slower in case2. The cm x-position is slightly ahead of the origin of the body frame and moves slightly backward as fuel is burned. As expected, the z-position of cm goes up as fuel is burned and goes down as tanks are refueled. Both figures above show that receiver aircraft in case2 has more fuel left at the end of the simulation. In case2, the simulation happens to stop right after the refueling while tanks 1 and 2 are almost half used in case1. In addition to how much fuel is burnt, the amount of fuel left at the end of the simulation is another indicator of formation flight benefit.

Figure 4.15 shows (1) the mass of the tanker aircraft, (2) the mass ratio of the tanker to the maximum gross mass and mass ratio of the fuel left to the maximum fuel capacity of the tanker, (3) fuel burnt by the tanker aircraft and (4) fuel transferred from tanker to the receiver. The first observation is about the flight duration. The simulations are set to stop when the fuel in tanker drops to 5%. Based on this, there is not much difference in flight time. The tanker flies only 5.4 minutes longer when

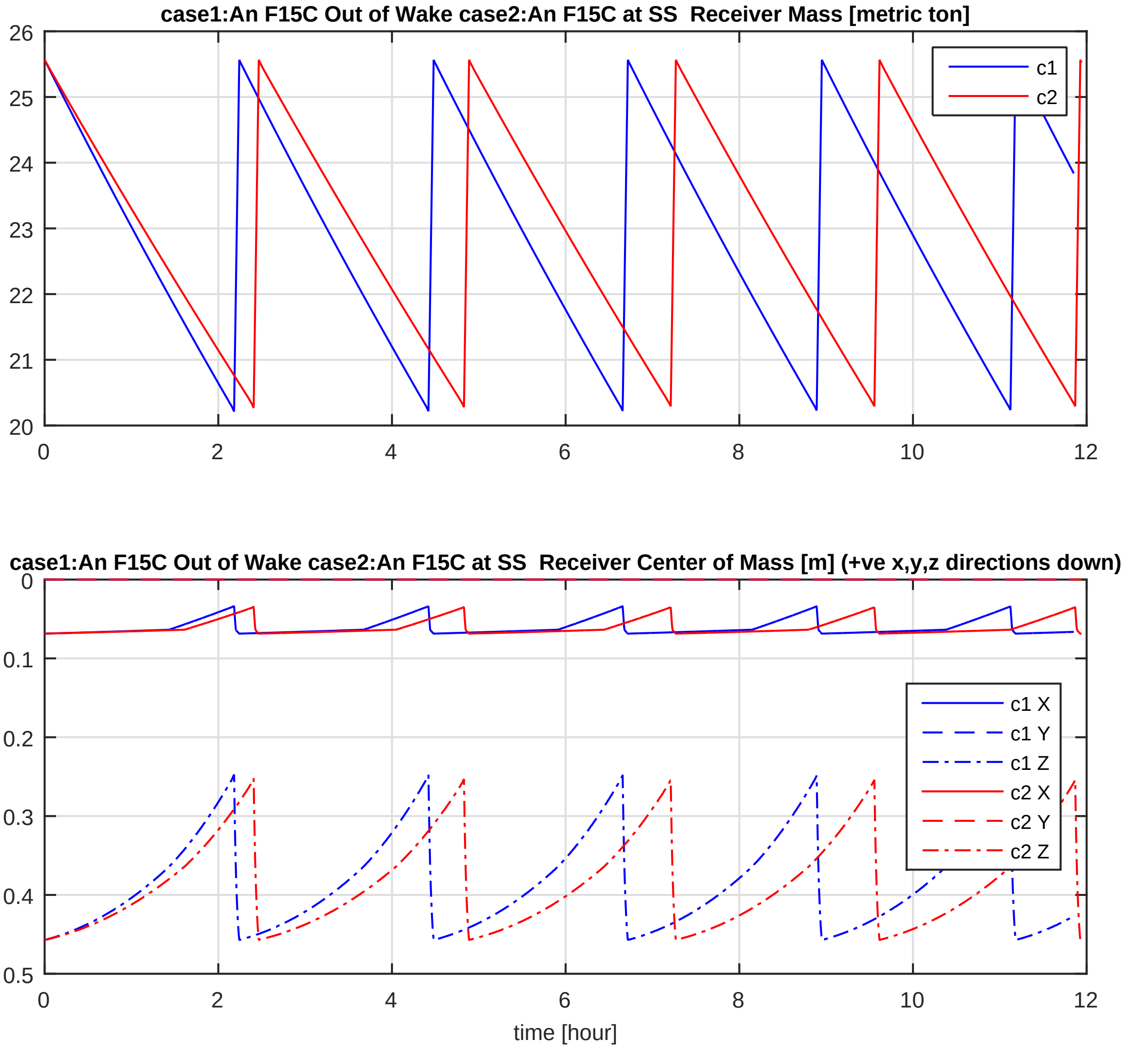

Figure 4.14. Single F-15C Receiver Mass and Center of Mass.

the receiver flies at the sweet spot. As stated earlier, the simulation starts when tanker has 81% fuel and ends when only 5% fuel left. Thus, in close to 12 hours, 75% of the tanker's fuel is used. The last two plots shows how much of this 75% fuel is burnt by the tanker and how much is transferred to the receiver. By the end of the simulation 42.6 tons of fuel is burnt by the tanker and 27.3 tons of fuel is transferred to the receiver.

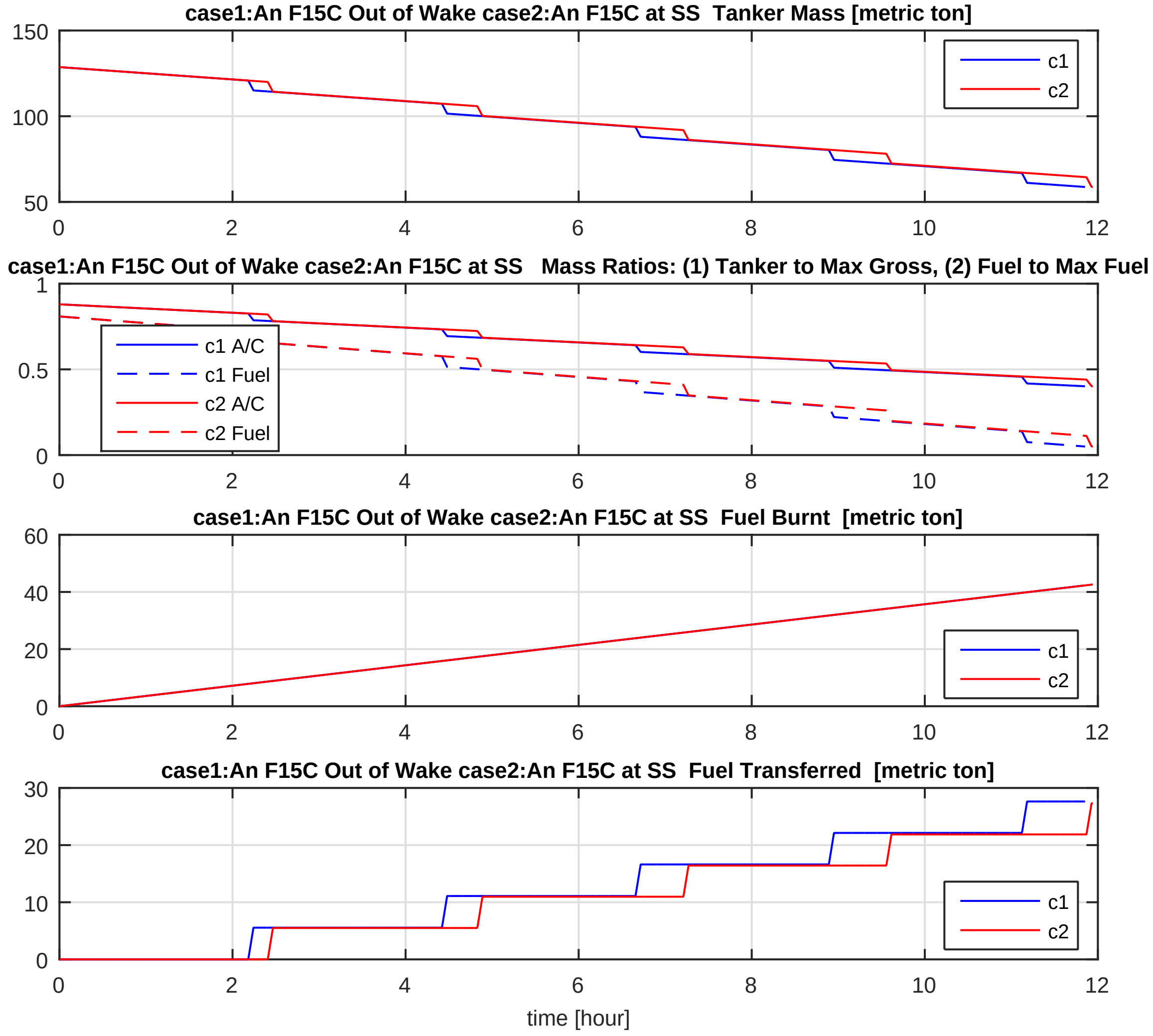

Figure 4.15. Single F-15C Tanker Mass.

Figure 4.16 shows (1) the amount of fuel burnt by the tanker and receiver during the flight, (2) the difference in the amounts of fuel burnt by tanker and receiver combined between the two cases presented, (3) the percent difference in total fuel burnt by the tanker and receiver between the two cases, (4) and the fuel transfer rate into the receiver aircraft. The fourth plot is included here just to illustrate when and how long actual fuel transfer takes place. The first plot shows that the tanker burns more fuel than the receiver aircraft. There is no visible difference in fuel burnt by the

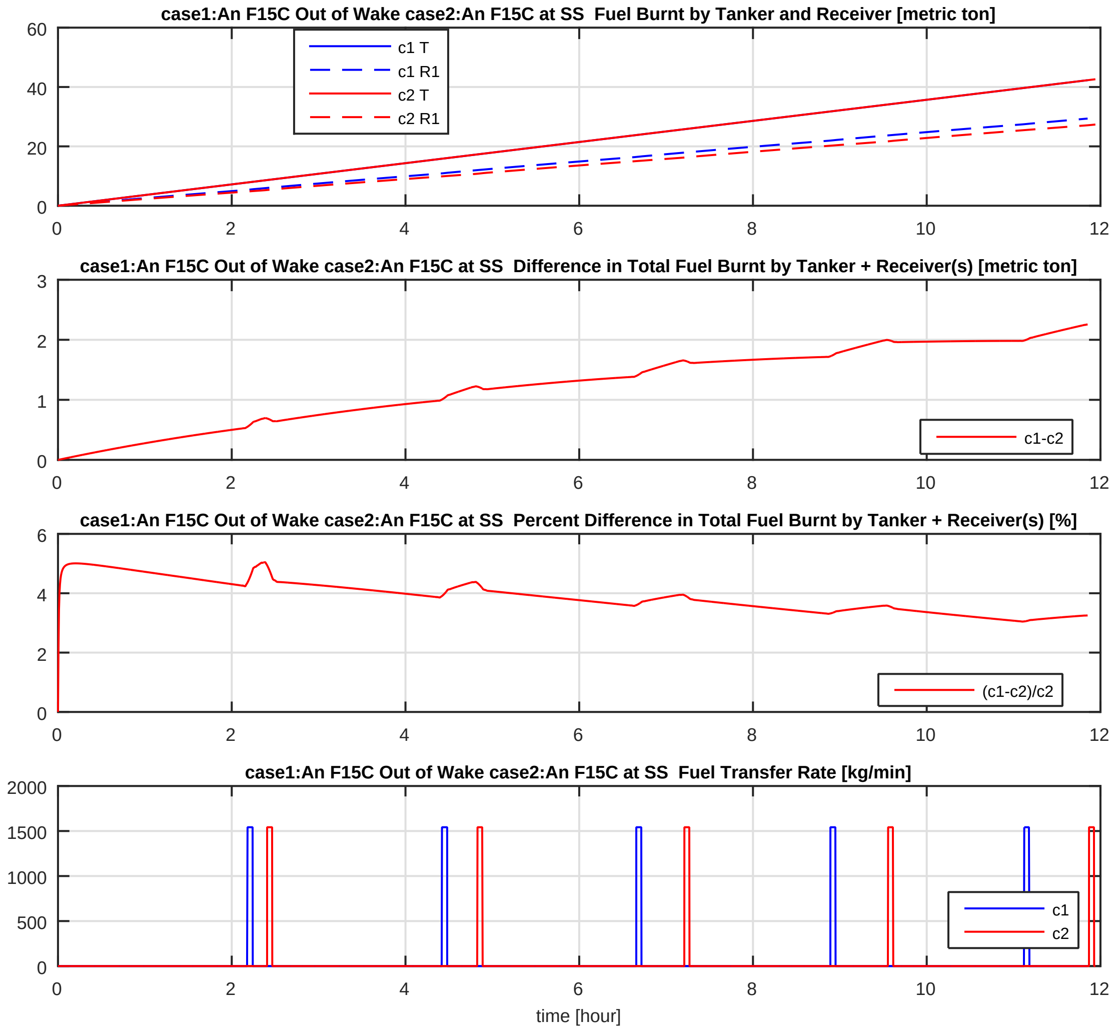

Figure 4.16. Single F-15C Tanker and Receiver Fuel Burn].

tanker between the two cases. It also shows that F-15C flying at the sweet spot burns less fuel compared to the F-15C flying out of the wake. Thus, the difference in the fuel burnt increases between these two cases as the flight time increases. This is used to quantify the benefit of formation flight at the sweet spot. The second plot shows this formation flight benefit in detail in terms of difference in total fuel burnt by the tanker and the receiver. Since the difference in fuel burnt by the tankers is not significant, the main reason of the difference in total fuel burnt is the due to the receivers. Since the aircraft flying at the sweet spot burns less fuel, it requires refueling later. This can be seen in the last plot. During this 12 hour flight, each aircraft needs to refuel four times. Each time the receiver flying at the sweet spot refuels at a longer time after the refueling of the receiver flying out of the wake. At the end of the 12 hour flight, the second plot shows 2.257 tons of fuel saved when the receiver flies at the sweet spot. Note the spikes between the refuelings from the second plot. The receiver flying out of the wake will refuel first by flying at the refueling position, which is in the strong downwash region, as shown before in Fig. 4.5, and thus requires more thrust to maintain the relative position. Further, after the fuel transfer, the receiver aircraft in this case is heavier since the other aircraft is flying with less fuel. These two mechanisms together increases the fuel burn rate and thus the increase in the fuel burnt difference. This spike disappears after the receiver flying at the sweet spot goes through refueling at a later time. The duration of the spikes increases and the magnitudes decreases between the subsequent refueling cycles. This is because time difference between the refueling of the receiver in case1 and that in case2 increases and the strength of the wake and thus the magnitude of the upwash at the sweet spot decreases as the tanker loses fuel. The percent fuel saved presented in the third subplot is the amount of fuel saved as presented in the second subplot relative to the fuel burnt by the tanker and the receiver combined in case2. This is a better measure of fuel saved since it puts it against the amount of fuel burnt by the tanker-receiver fleet if the receiver flies at the sweet spot. Thus, the percent fuel saved, in a sense, is the amount of extra fuel that would be burnt if the receiver flies out of the wake instead of at the sweet spot as compared to the fuel burnt when the receiver flies at the sweet spot. The percent fuel saved starts at about 5% initially and decreases as the tanker weight decreases. By the end of the mission, the percent fuel saved drops to about 3%. This clearly shows that the formation benefit directly depends on the weight of the tanker.

4.2.2 Two F-15C escorted by KC-135R

In the previous section, the simulation results of one F-15C escorted by a KC-135R are presented. This section shows the fuel saving results when two F-15C are escorted by a KC-135R. Since the two-receiver simulation is done with the one full receiver model simulation with the second receiver represented as additional fuel offload from the tanker, as discussed earlier, only the fuel saving results are shown in this section. The other figures are exactly the same.

Figure 4.17 presents the amounts of fuel burned by the tanker and each receiver, and the fuel saved by the whole fleet of one KC-135R and two F-15C flying at sweet spots on each side of the tanker. The flight time difference between the two cases is now 34 min. Recall from the previous section that in the cases of one receiver, the difference was only 5.4 min. The flight time in the case of sweet spot (case2) is 9.5 hours while it was 11.94 when the tanker was escorting one receiver. This is because the ratio of the fuel used by the tanker to the fuel transferred to receiver does not linearly change with the number of receivers. In the case of one receiver, by the end of 11.94 hour flight, 42.61 tons of fuel is used by the tanker and 27.31 tons are transferred to the single receiver. In the case of two receivers, by the end of 9.5 hours of flight, 33.94 tons of fuel are used by the tanker and 35.98 tons are transferred to the receiver. In the case of a single receiver, at 9.5 hour, about the same amount of fuel is used by the tanker but 16.42 tons of fuel is transferred to the receiver. Note that 16.42 is less than half of 35.98 (see Fig. 4.18). Both subplot 2 and 3 show similar trends in fuel saved in terms of amount and percentage, respectively, as in the case of

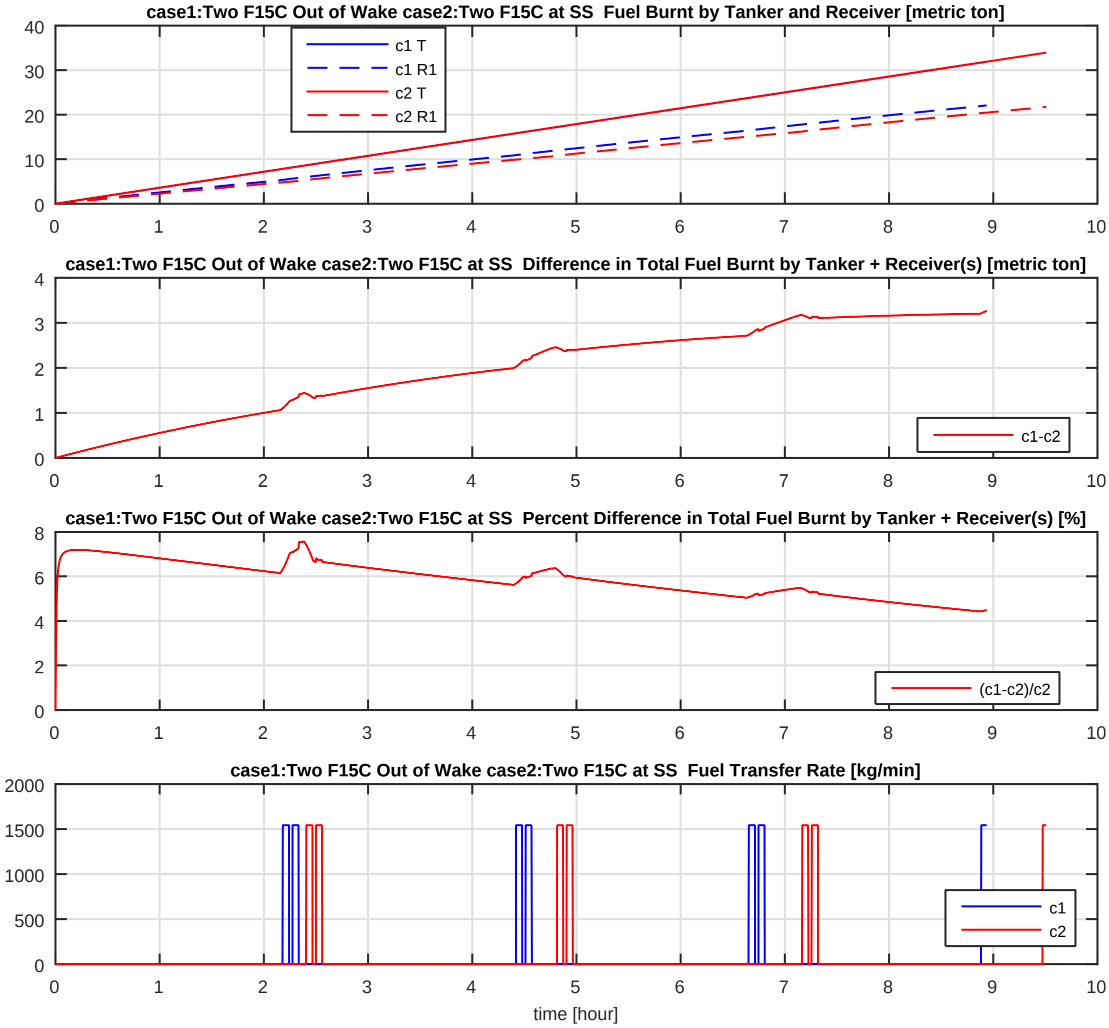

Figure 4.17. Two F-15C Tanker and Receiver Fuel Burn.

one F-15C cases presented in Fig. 4.16. The comparison between the single receiver and two receiver cases are given in the next section.

Table 4.3 compares the percent fuel saved in two-hour intervals with one receiver versus two receivers flying at the sweet spot. It is clear that utilizing the two sweet spots on both sides of the tanker by two receiver aircraft results in more fuel saved compared to the same fleet of aircraft with receivers flying outside the wake. The

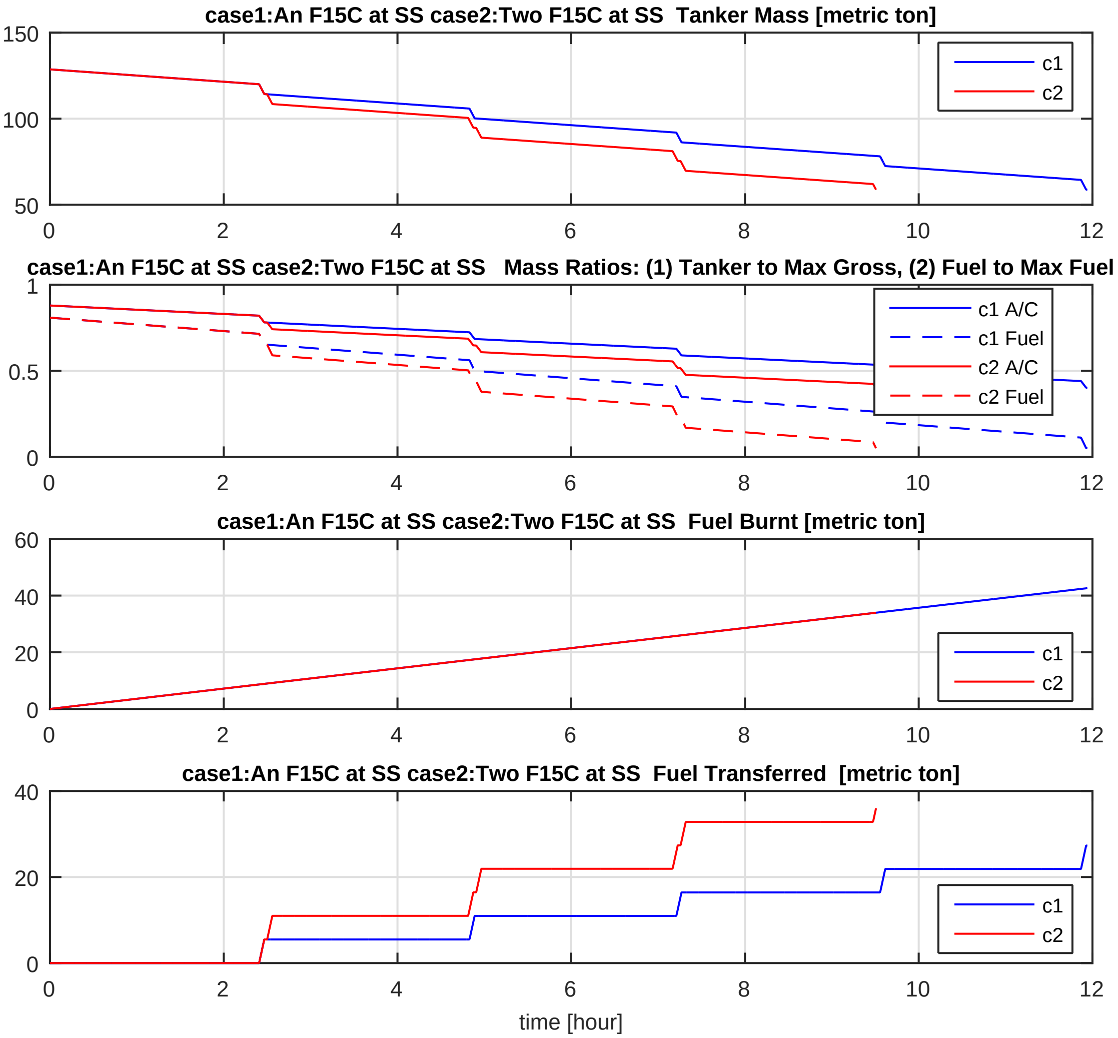

Figure 4.18. Tanker Aircraft and Fuel Mass Properties in One vs Two F-15C.

middle column is added to note the observation that fuel saved in percentage is not doubled with two receivers as compared to one receiver.

Table 4.3. Comparison of Percent Fuel Saved between One versus Two F-15C

Flight Time [hour]	% Fuel Saved		
	One F-15C	2×One F-15C	Two F-15C
2	4.307	8.614	6.237
4	3.984	7.968	5.831
6	3.767	7.534	5.369
8	3.565	7.130	4.848

4.3 Comparison of F-15E and F-15C

Before the simulation results of the F-15E coronet missions are presented, a comparison of the F-15E and F-15C aircraft responses, when they fly at the sweet spot, are provided in this section. This should help better understand the differences in the results of the coronet mission with F-15E and F-15C. The first subplot of Fig. 4.19 shows the mass variation during the mission. The F-15E is almost always heavier than F-15C. This results in the observation in the second subplot that F-15E burns more fuel than F-15E does. This is obviously because the F-15E is and flies heavier and the F-15E has more aerodynamic drag due to the addition of the conformal tanks. The third subplot shows that F-15E flies longer before refueling even though it burns more fuel. This is due to the fact that F-15E uses two extra conformal tanks while F-15C uses only three external tanks. The third subplot also shows that F-15E takes longer to refuel because it needs to refuel two conformal tanks in addition to the three external ones. The last subplot shows that the F-15E always flies with higher thrust compared to the F-15C and thrust saturates at the refueling position when it is near and at its max weight.

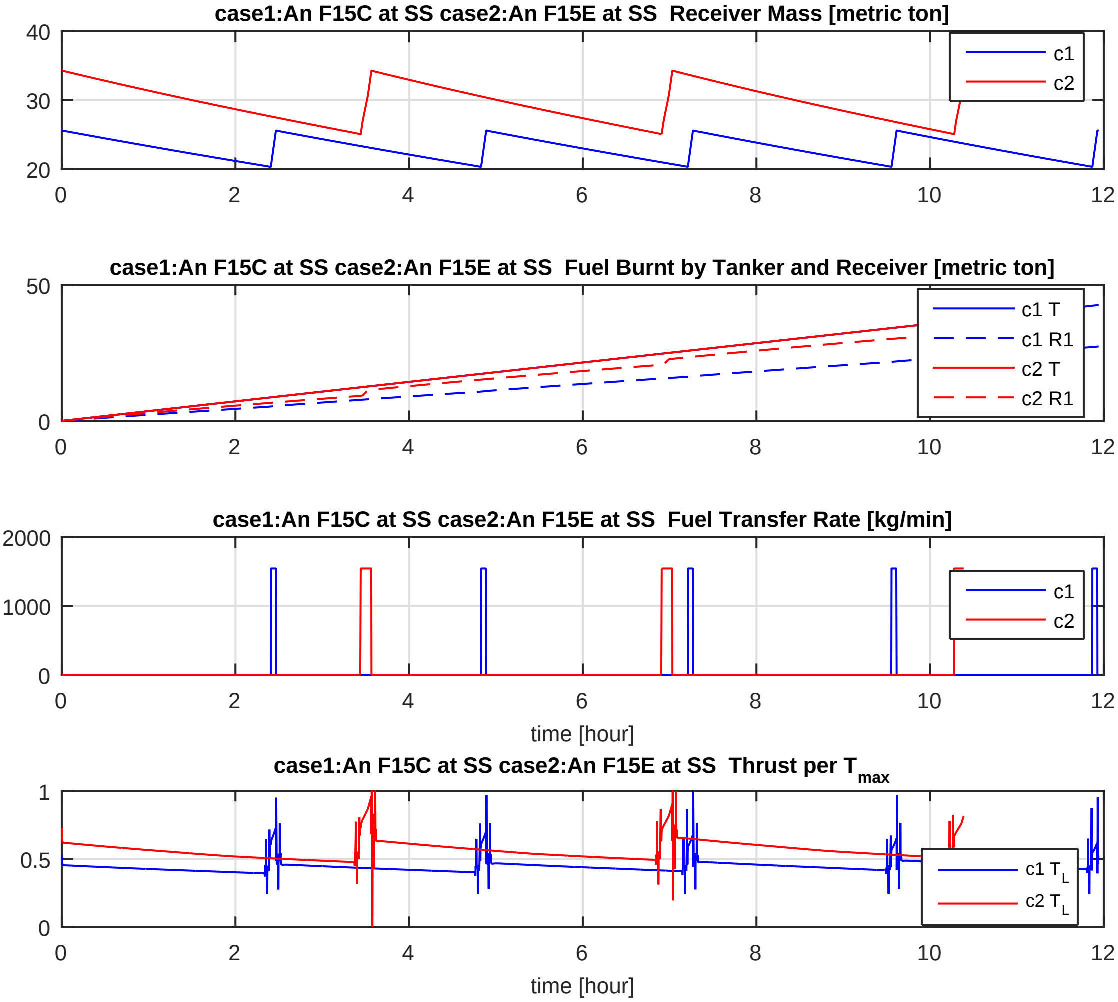

Figure 4.19. Comparison of F-15E and F-15C in Coronet Mission.

4.3.1 F-15E Coronet Mission Simulations

This section presents the fuel saving when F-15E receivers fly at the sweet spots of the tanker in a coronet mission. The results of the single F-15E are presented first, followed by two F-15E. In the figures for the F-15E, case1 is when the receiver flies out of the wake and case2 is when at the sweet spot, as before.

Figure 4.20 shows the same fuel quantities as in the F-15C sections. As seen from the first subplot of the figure on the previous page, the amount of fuel burnt by an F-15E out of the wake increases faster than that by an F-15E at the sweet spot.

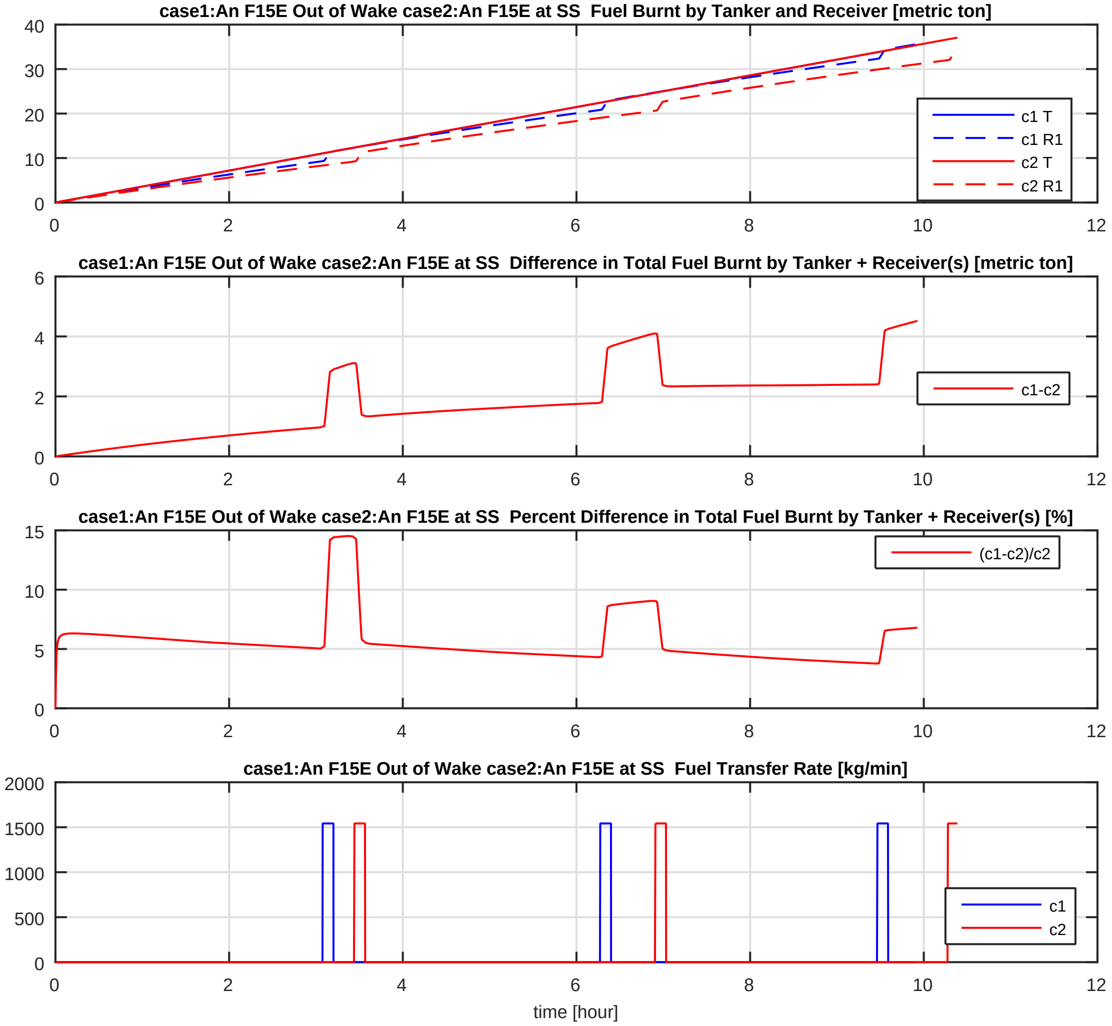

Figure 4.20. Single F-15E Tanker and Receiver Fuel Burn.

The second subplot above shows the difference in the amount of fuel burnt by tanker and the F-15E together between the two cases (F-15E is flying out of wake or at the sweet spot). As the first plot indicates, the tanker seems to burn about the same amount of fuel between the two cases. Thus, the increase in the difference in the fuel burnt between the two cases is mainly due to the F-15E burning less fuel at the sweet spot. The third subplot shows the percent fuel saved, which is more than that in the case of an F-15C, shown in Fig. 4.16. Since the F-15E aircraft out of the wake burns fuel faster, it went through refueling earlier as shown in the last subplot. When the F-15E goes to the refueling position, it needs to fly at the downwash region, which is less efficient than flying out of the wake. Further, as fuel is transferred, it becomes heavier and burns more fuel. This all happens while, in the other case, the F-15E is flying at the sweet spot and flying light. That is why the difference in fuel burnt increases significantly. Once the F-15E goes back to its formation position out of the wake after refueling, it is heavier than the F-15E in the other case (case2). In the meantime, the F-15E in case2 is still flying at the sweet spot. Thus, the increase in difference in fuel burnt slows down. About 15 minutes after the F-15E in case1 is refueled, the F-15E in case2 goes through refueling. Since the F-15E in case2 moves to refueling position with downwash and its weight increases through refueling, it starts burning fuel faster, which results in a decrease in difference in fuel burnt. Once the F-15E in case2 is done with refueling and moves back to the sweet spot, the difference in fuel burnt starts increasing again even though the F-15E in case2 is heavier than that in case1. This increase between the refueling maneuvers was not as prominent in the case of the F-15C because the F-15E needs to stay at the refueling position longer as it refuels the two conformal tanks in addition to the three external ones. Further, the weight difference before and after the refueling is much higher in the case of a F-15E than of a F-15C as, again, F-15E uses and refuels the two conformal tanks.

Figure 4.21 shows the same quantities when two F-15E are escorted by the tanker. The main point to note here is that the fuel saved in magnitude as well as in comparison to two aircraft flying out of the wake increases relative to the fuel save when one F-15E is escorted. This observation was made when F-15C cases were compared as well. The next section will show the comparison of fuel saved in percentage among cases when one or two F-15C or F-15E are escorted in coronet missions.

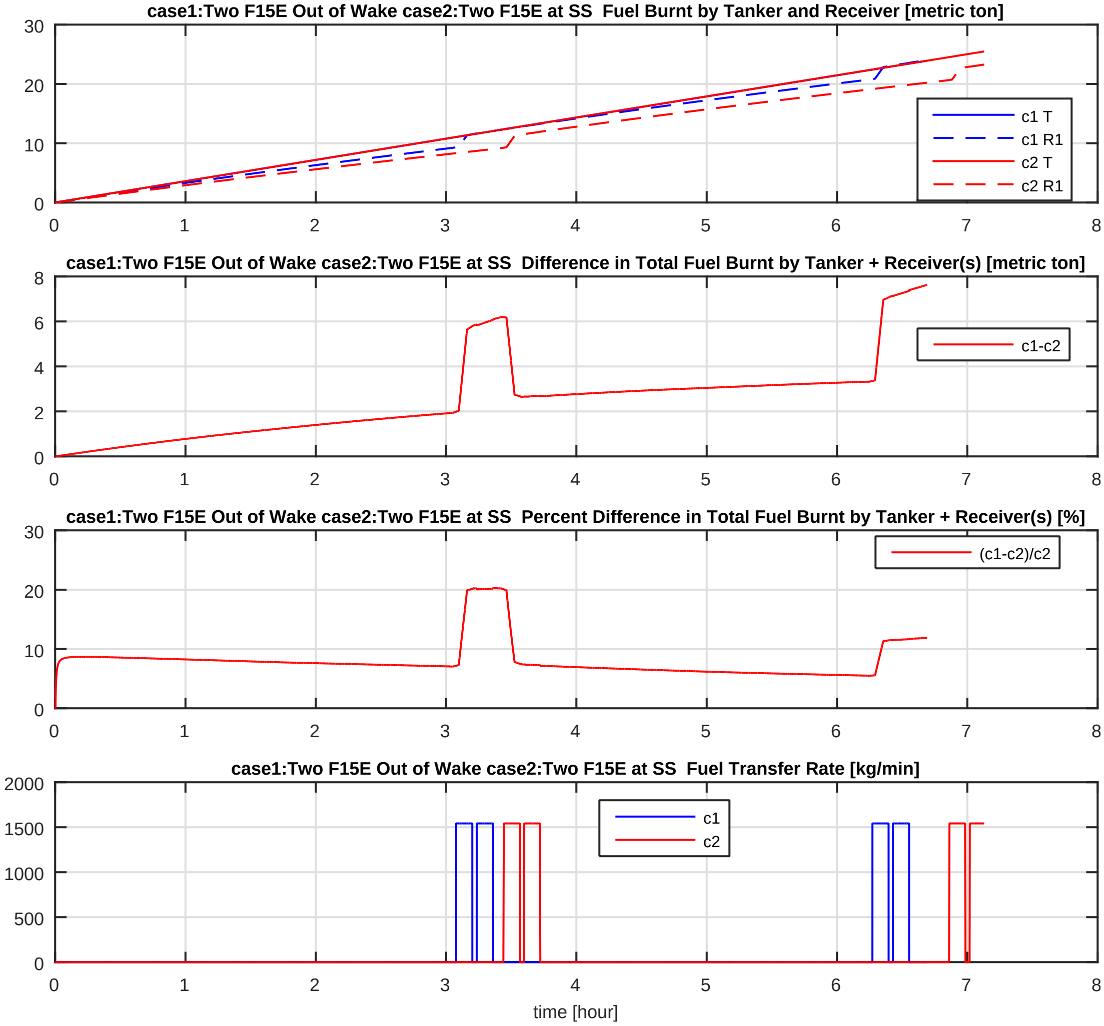

Figure 4.21. Two F-15E Tanker and Receiver Fuel Burn.

4.3.2 Comparison of One/Two F-15C/E Missions

This section summarizes the four simulation comparisons to show the percent fuel saved when one or two F-15C or F-15E are flown at sweet spots. Table 4.4 shows the percent fuel savings based on mission length in one hour intervals. The data shows that the F-15E has a higher percentage of fuel savings than the F-15C. Note that even the same value of percentage would be equivalent to a higher amount of fuel saved in the case of F-15E since F-15E burns more fuel. It also shows that a higher percentage of fuel is saved when two receivers fly in the sweet spots, however the overall fuel savings does not double.

Table 4.4. Coronet Mission Summary of One or Two F-15C or F-15E

Flight Time [hour]	% Fuel Saved			
	One F-15C	Two F-15C	One F-15E	Two F-15E
1	4.722	6.811	5.962	8.238
2	4.307	6.237	5.467	7.603
3	4.271	6.387	5.058	7.072
4	3.984	5.831	5.244	6.938
5	4.068	5.941	4.768	6.177
6	3.767	5.369	4.396	5.620

CHAPTER 5

ALTERNATE TRIMMING METHODS

5.1 Overview

This chapter explores two additional trimming methods, zero yaw angle and zero bank angle, respectively. First, the dynamic sweet spot analysis from Section 3.2 is repeated to establish the sweet spot location. Next the full mission simulation from Chapter 4 and the fuel burn is compared to the zero side slip angle case.

5.2 Dynamic Sweet Spot Analysis

The dynamic sweet spot analysis from Section 3.2 is repeated for a zero roll angle trimmer and a zero bank angle trimmer, respectively. Rather than using Eq. (2.57) as the output vector, as is the case in Section 3.2, Section 5.2.1 uses Eq. (2.58) and Section 5.2.2 uses Eq. (2.59), respectively. The results are then compared to the zero side slip angle case.

5.2.1 Zero Roll Angle

Figure 5.1 shows the change in thrust for the heavy tanker full F-15C case with zero roll angle trimming method. The figure shows that the dynamic sweet spot is at the same location as it is, when the zero side slip trimming method is used. The magnitude of the thrust reduction is also nearly the same for both cases, a 14.17% reduction for the zero roll angle method and 14.15% reduction for the zero side slip method, respectively. Figure 5.2 shows a comparison between the two methods. The value shown is the percentage change relative to the zero side slip case at each grid

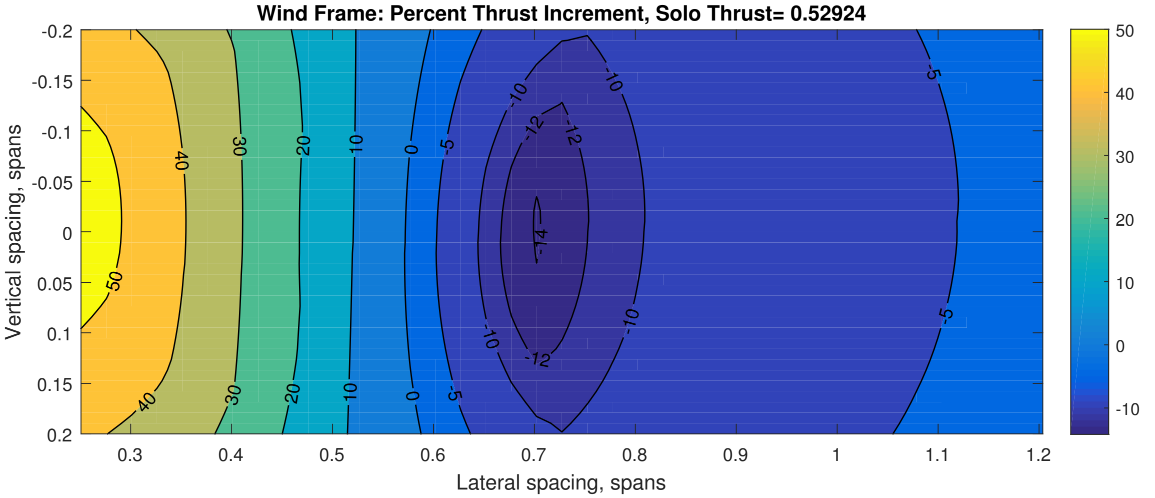

Figure 5.1. Change in Thrust Required (No Roll Trimming Method).

point. A negative number represents additional savings for the zero roll angle method over the zero side slip method. It shows that inboard of the dynamic sweet spot the zero roll angle method is more efficient than the zero side slip angle method, when flying below the tanker, which means that it is not only more efficient to trim for zero roll angle at the sweet spot, but also at the refueling position and the transition to the refueling position. It also shows that throughout the grid the difference in reduction between the two methods is a maximum of only 1%. The high-gradient oval region between 0.3 and 0.5 lateral spans is caused by aileron saturation in that region.

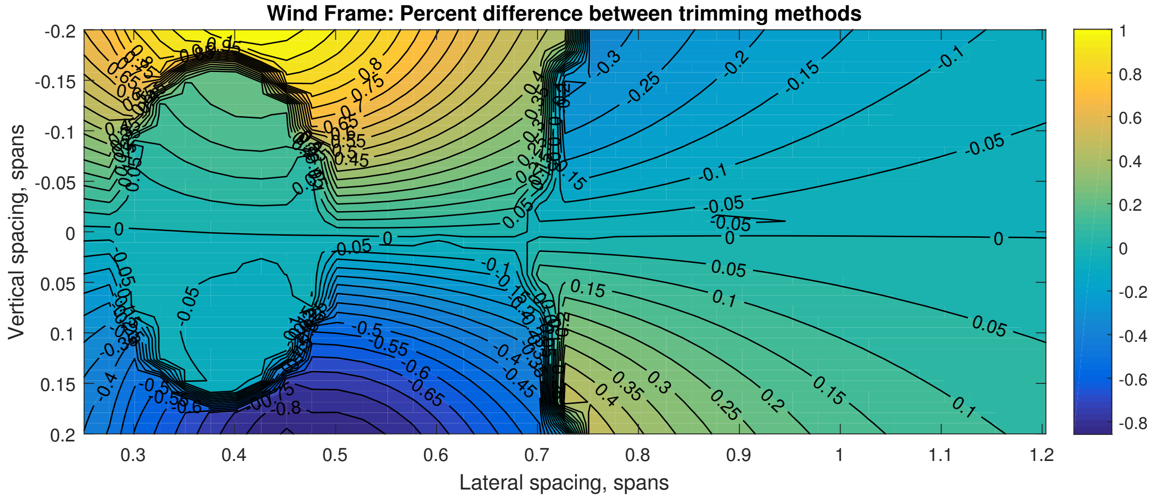

Figure 5.2. Change in Thrust Required (No Roll Trimming Method).

5.2.2 Zero Yaw Angle

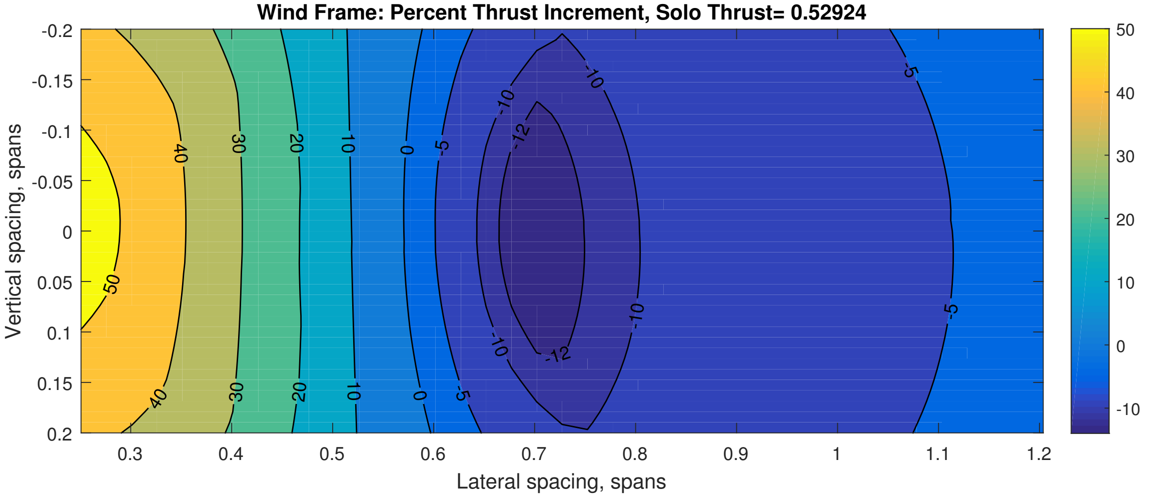

Figure 5.3. Change in Thrust Required (No Yaw Trimming Method).

Figure 5.3 shows the change in thrust for the heavy tanker full F-15C case with zero yaw angle trimming method. The figure shows that the dynamic sweet spot is at the same location as it is for the two other methods. The magnitude of the thrust reduction is smaller than it is for the other methods, at 13.98%. Figure 5.4 shows a comparison between the zero yaw angle and zero side slip method, where a negative number represents additional savings for the zero yaw angle method over the zero side slip method. It shows that the zero yaw angle trimming method is less efficient than the zero side slip method throughout in all formation flight positions. This means that for the heavy-heavy case the zero yaw angle trimming method is the least efficient. Again, the high-gradient oval region between 0.3 and 0.5 lateral spans is caused by the aileron saturation.

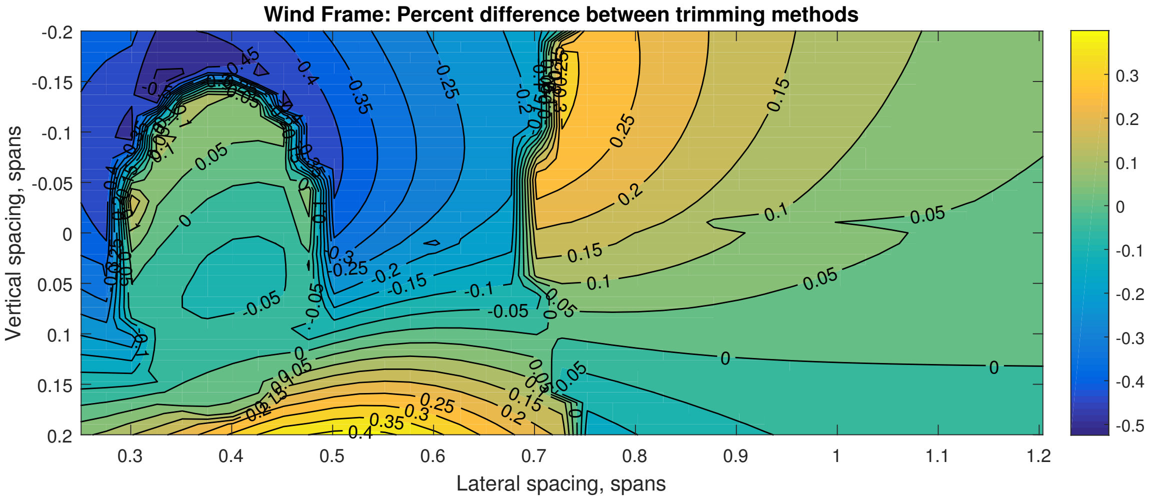

Figure 5.4. Comparison of Thrust Required (No Yaw Trimming Method).

5.2.3 Summary

The trimming method that provides the greatest benefit for the heavy tanker, full receiver case at each location is shown in Fig. 5.5. The blue region is where the zero yaw angle method works best, the green region is where the zero roll angle method works best and the yellow region is where the zero slip method works best.

The map again shows that in all formation flight and transition positions the zero roll angle method provides the greatest thrust reduction. Table 5.1 summarizes the results for all configurations. For a heavy tanker it is always best to use the the zero roll angle trimming method at the sweet spot, while the zero yaw angle method is the worst. The difference between the zero roll angle and zero side slip methods are very small, however. For a light tanker the zero yaw angle trimming method is the most efficient at the dynamic sweet spot.

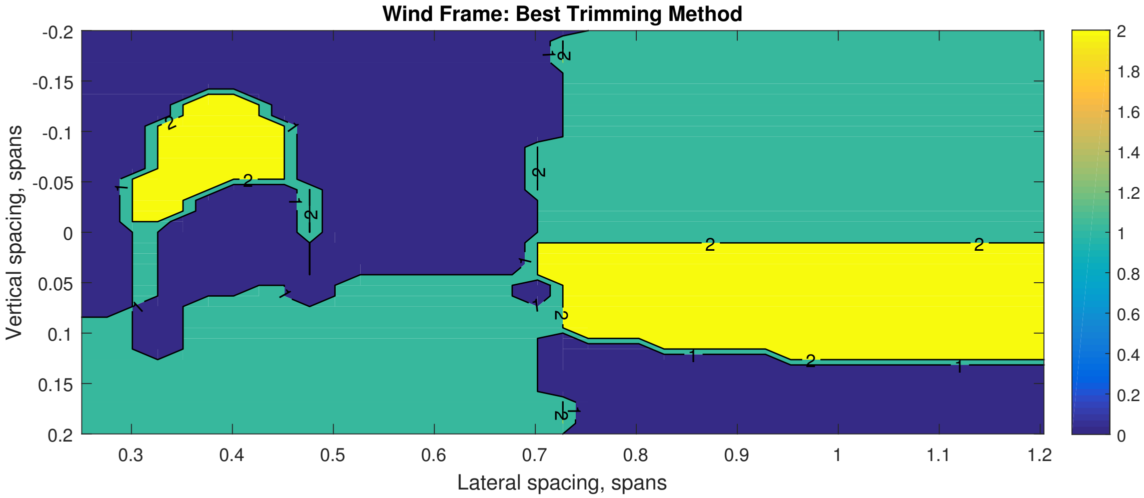

Figure 5.5. Best Trimming Method Map (Blue = Zero Yaw, Green = Zero Roll, Yellow = Zero Sideslip).

Table 5.1. Dynamic Sweet Spot Comparison

Tanker	Receiver	No Sideslip			No Roll Angle		No Yaw Angle	
Aircraft Mass	Fuel Mass	Position [tanker wingspan]		Thrust Reduction [%]	Position [tanker wingspan]	Thrust Reduction [%]	Position [tanker wingspan]	Thrust Reduction [%]
		Y	Z		Z		Z	
Heavy	Full	0.7022	0	14.15	-0.0105	14.17	-0.0105	13.98
	Empty	0.7022	0	12.59	0	12.62	0.0211	12.46
Empty	Full	0.6520	0	12.35	0.0105	12.36	0	12.38
	Empty	0.6520	0.0105	10.92	0.0105	10.94	0	11.04

5.3 Full Mission Analysis

The full mission simulation is run with the same mass and fuel configuration as outlined in Section 2.5. Simulations start when the fighter aircraft is at the sweet spot. The full mission is run for all three trimming methods.

The first plot in Fig. 5.6 shows the total fuel burnt by the tanker and receiver during a 15 hour mission using the zero roll angle and zero side slip trimming methods. The total fuel burnt is nearly identical for both cases. The second plot shows the difference between the two methods. At the end of a 15 hour flight a total of 88 tons of fuel are burnt, however the difference between the two methods is only 75kg. The third plot shows the percent difference in total fuel burnt between the two methods. At the end of the flight about the zero roll angle method burns about .1% less fuel. The final plot shows when the receiver comes in to be refueled for both methods. With the zero roll angle trimming method the F-15C comes in for refueling slightly later. The final refueling maneuver happens 2.4 minutes later for the zero roll angle trimming method. In a realistic mission this will not allow for a refueling maneuver to be removed from the mission, as the time interval is very small.

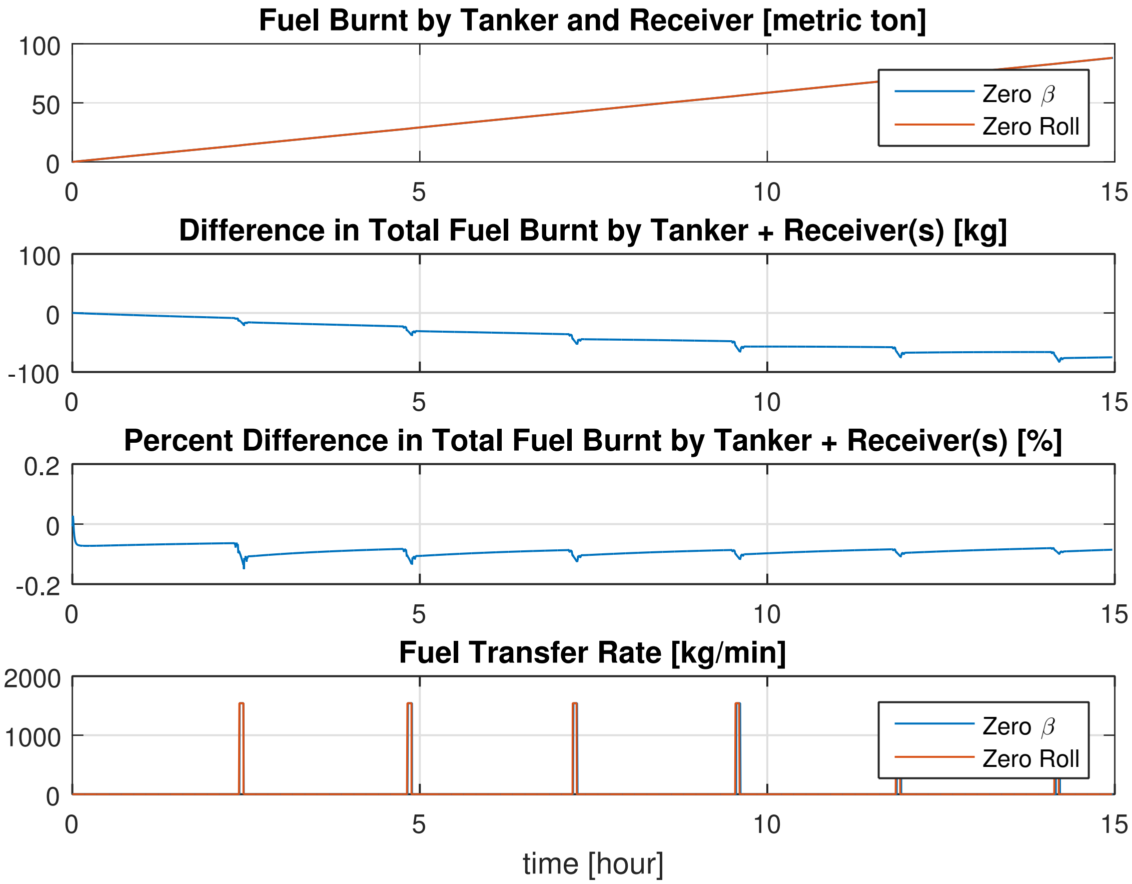

Figure 5.6. Comparison of Zero Side Slip and Zero Roll Angle Trimming Methods in Extended Formation Flight.

Figure 5.7 contains the same four plots as Fig. 5.6, using the zero yaw angle trimming method instead. The zero yaw angle method burns 83kg more fuel than the zero side slip method. The difference between the two methods is only .09%. From the results summarized in Table 5.1 it should be expected that the zero yaw angle trimming method requires less thrust as the tanker gets lighter, however that is only true at the sweet spot, which moves inboard. Since the sweet spot is not tracked, that effect is not visible in the results and the zero yaw angle method continues to require more thrust than the zero side slip method.

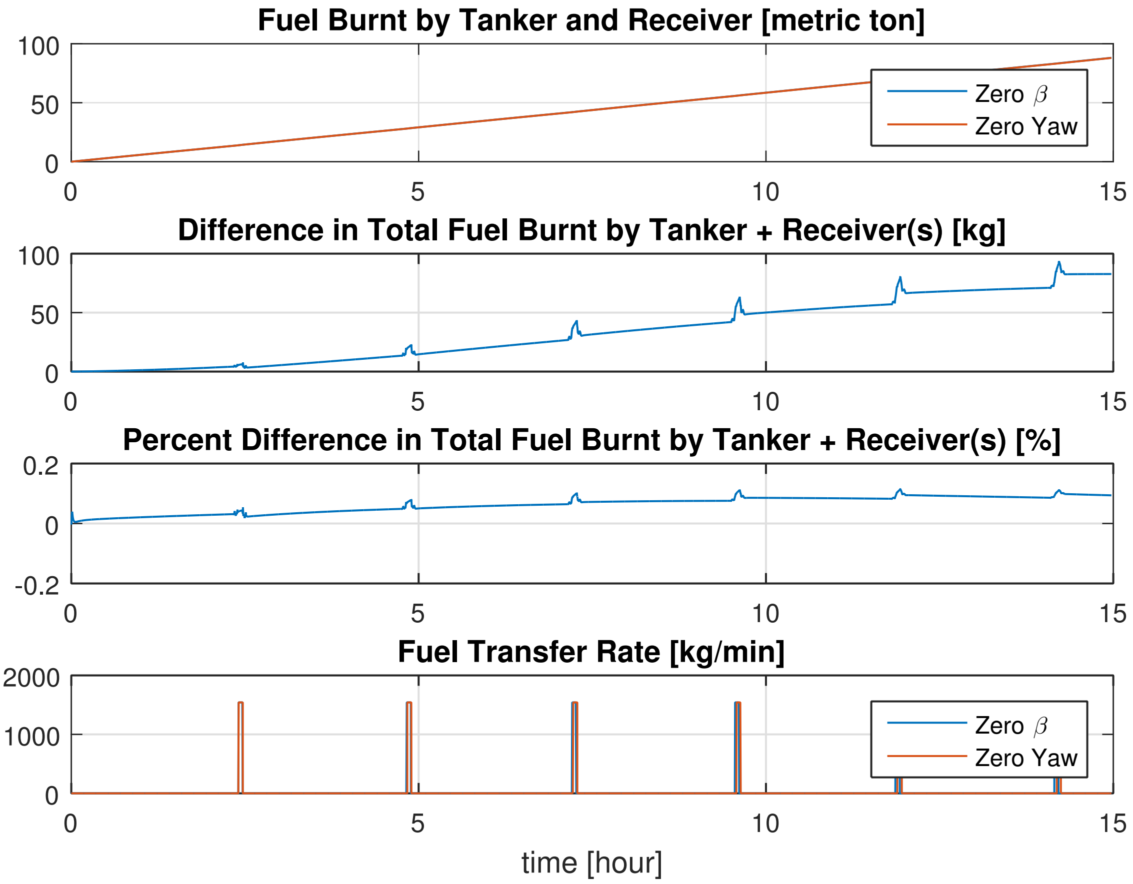

Figure 5.7. Comparison of Zero Side Slip and Zero Yaw Angle Trimming Methods in Extended Formation Flight.

CHAPTER 6

SWEET SPOT TRACKING

6.1 Setup

In Chapter 4 the coronet missions were run keeping the receiver in the heavy tanker sweet spot position. Chapter 3 shows that as the tanker gets lighter, the sweet spot moves inboard, therefore it should be possible to obtain additional savings by moving the receiver inboard as the tanker gets lighter and essentially tracking the sweet spot. To get a better idea of how the sweet spot changes with tanker weight, additional data points are necessary. The dynamic sweet spot analysis is run for 2 additional tanker weights, however to reduce computational requirements the Z-position is kept at 0. Additionally, the grid in the Y-direction is refined to 0.1m increments to increase the fidelity. The analysis is run for all 3 trimming methods. The output of this analysis is 4 sweet spot data points for each trimming method. The data points are linearly interpolated in the simulation based on tanker weight to obtain an updated commanded Y-position. The tanker weights used to obtain the 4 data points are 128660 kg (88% max mass), 88380 kg (60% max mass), 61866 kg (42% max mass) and 36369 kg (25% max mass), respectively. Note that the lightest weight chosen is significantly lighter than the empty gross weight of the KC-135R (54124kg or 37% max mass) to ensure the simulated tanker weight is never out of the bounds of the interpolation range. The results are summarized in Table 6.1.

Table 6.1. Sweet Spot Data Points

	No Sideslip	No Roll	No Yaw
128660 [kg]	27.9 [m]	28.0 [m]	27.8 [m]
88380 [kg]	26.1 [m]	26.1 [m]	26.0 [m]
61866 [kg]	24.7 [m]	24.7 [m]	24.6 [m]
36369 [kg]	23.2 [m]	23.2 [m]	23.1 [m]

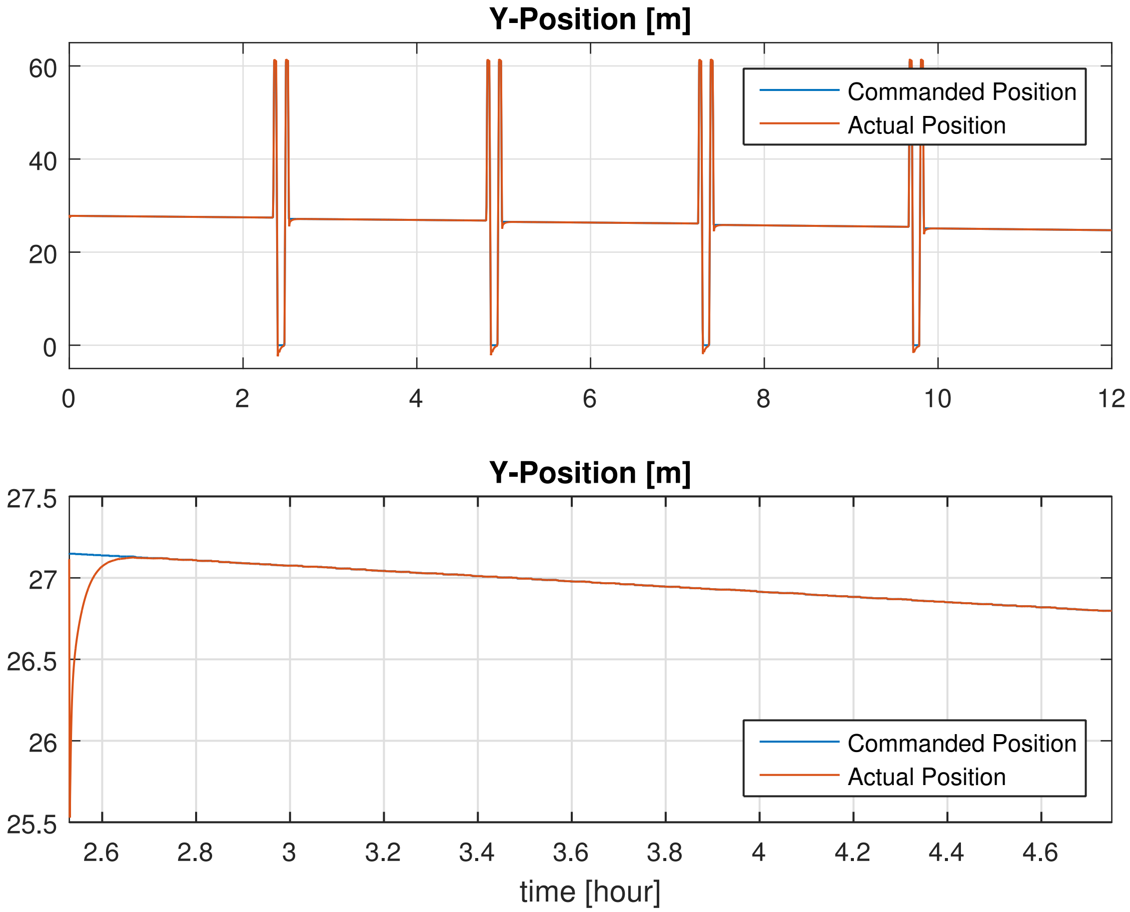

Figure 6.1. Y-Position Change and Tracking During Extend Formation Flight.

6.2 Results

Figure 6.1 shows the commanded and actual y-position during the coronet mission. As time goes on, the sweet commanded position moves inboard. The top plot shows that the controller is able to track the commanded position very well. The

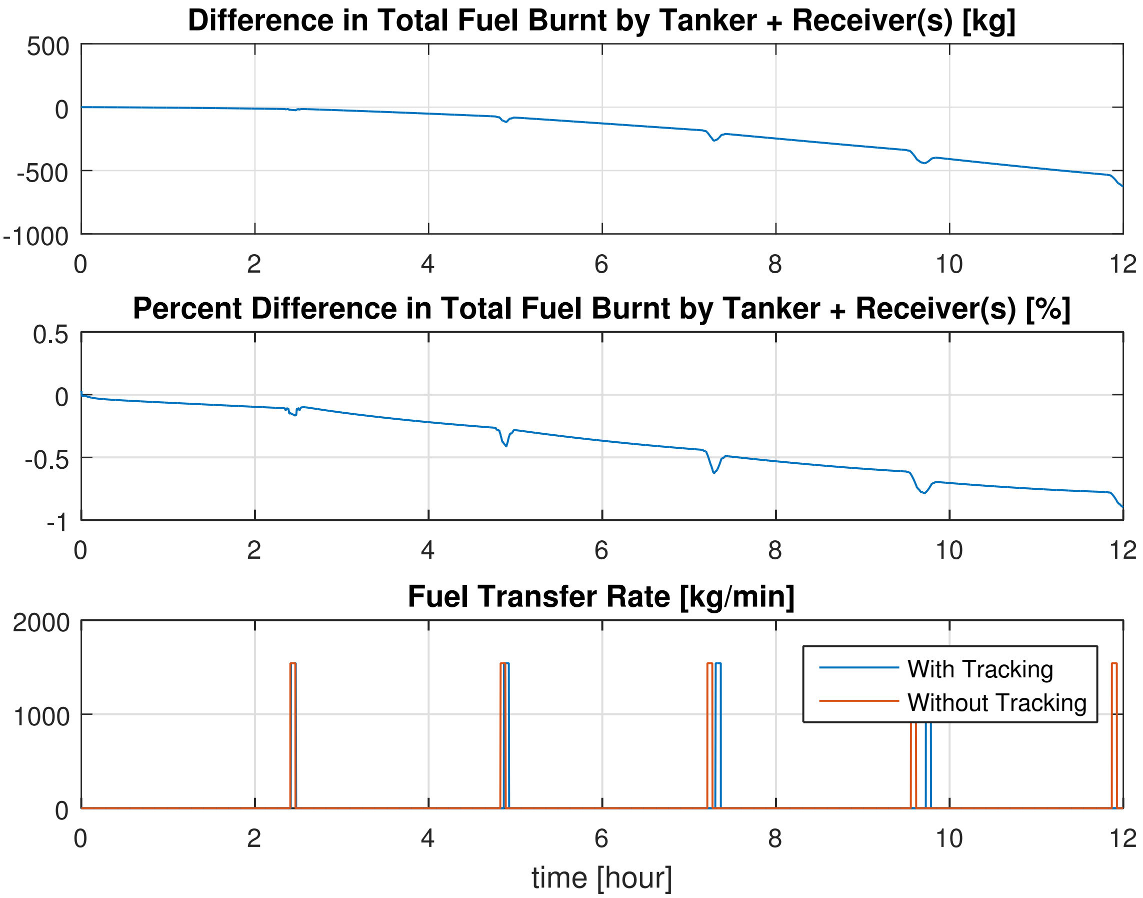

Figure 6.2. Comparison of Sweet Spot Tracking and no Tracking using the Zero Side Slip Trimming Method in Extended Formation Flight.

bottom plot is a zoomed-in version of the top plot showing the change in commanded position between the first and second refueling. Between refuelings, the commanded position shifts approximately 0.5 m. The plot also shows how well the controller tracks the commanded position. Figures 6.2-6.4 compare the sweet spot tracking controller to the non-tracking controller for all 3 trimming methods. All 3 cases show virtually the same results. Between 500-700 kg of fuel is saved, which is between 0.5% and 1% of the total fuel burned, depending on which controller is used. The zero yaw method shows the largest benefit from sweet spot tracking. The difference in total fuel burnt by tanker and receiver plot shows that the savings increase more as the tanker gets

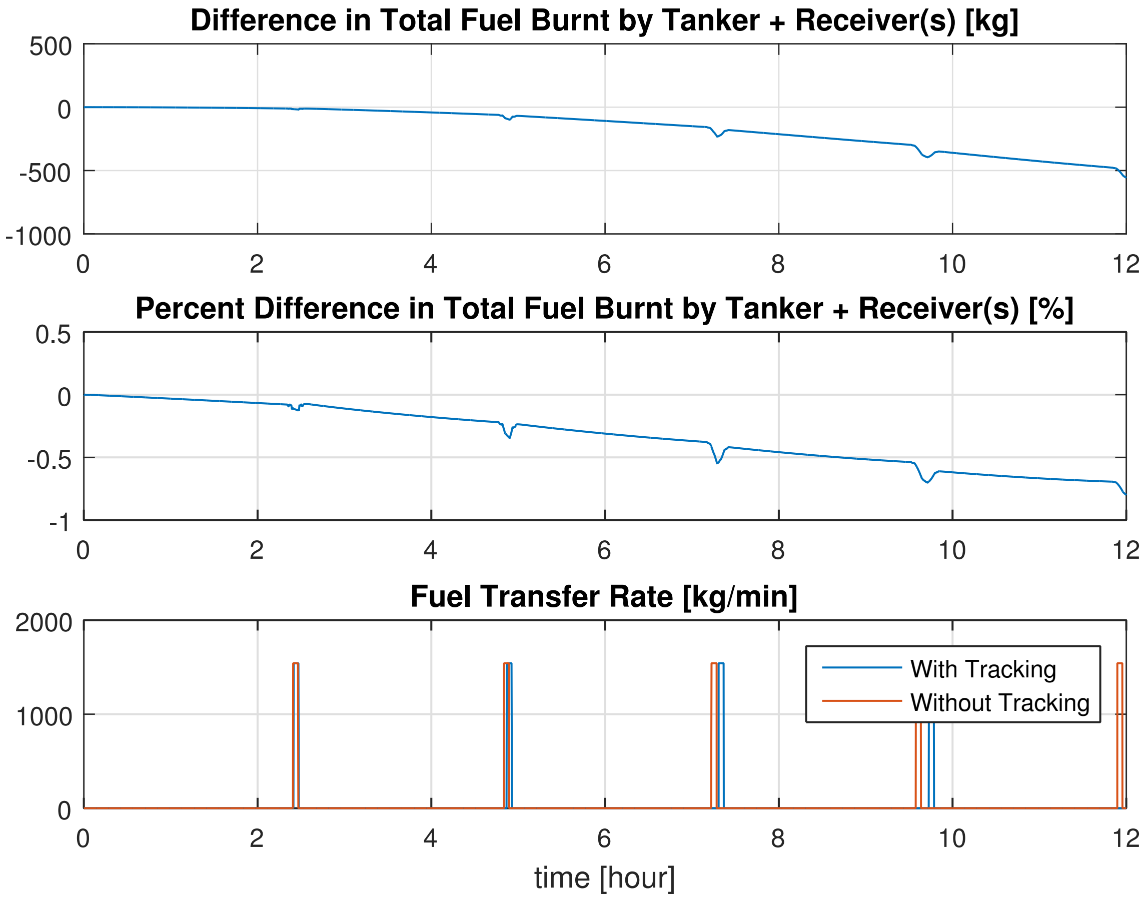

Figure 6.3. Comparison of Sweet Spot Tracking and no Tracking using the Zero Roll Angle Trimming Method in Extended Formation Flight.

lighter, which can be explained by the receiver being further away from the actual sweet spot as the tanker gets lighter when the sweet spot is not tracked. The data shows that after each refueling maneuver the rate of savings becomes larger. This can be explained by the tanker offloading fuel to the receiver and becoming significantly lighter and consequently the sweet spot moves inboard rapidly causing the actual sweet spot to drift further inboard from the heavy configuration sweet spot that is used for the non-tracking analysis. The fuel transfer plot within the figures shows that the time between refuelings is increasingly later than when the sweet spot is not tracked. Figure 6.5 shows the fuel burn of the receiver during the coronet mission with tracking and without tracking, respectively. The plot clearly shows that the fuel burn increases with each refueling maneuver, due to the weaker wake. In the non-tracking case this effect is amplified by flying at the heavy-heavy sweet spot location. The rate of increase in fuel burn after refuelings is drastically reduced by tracking the sweet spot.

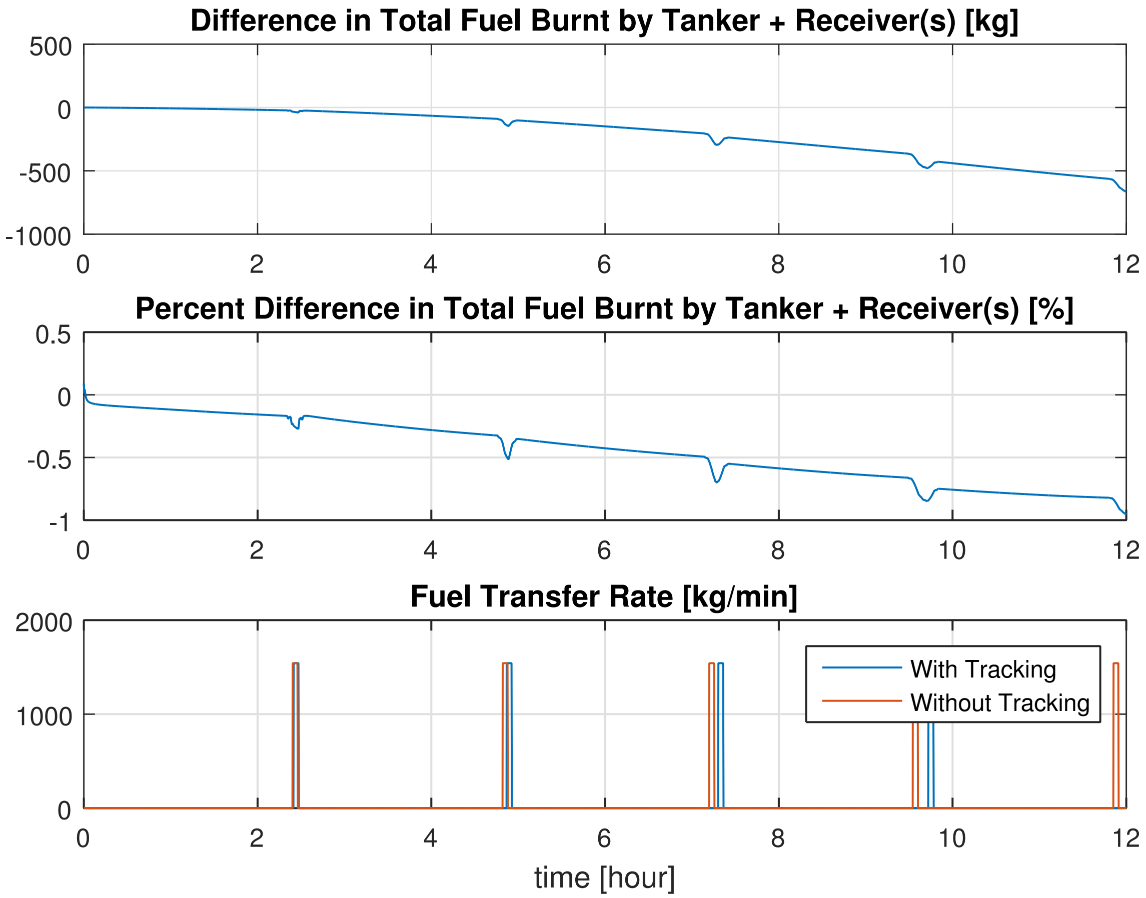

Figure 6.4. Comparison of Sweet Spot Tracking and no Tracking using the Zero Yaw Angle Trimming Method in Extended Formation Flight.

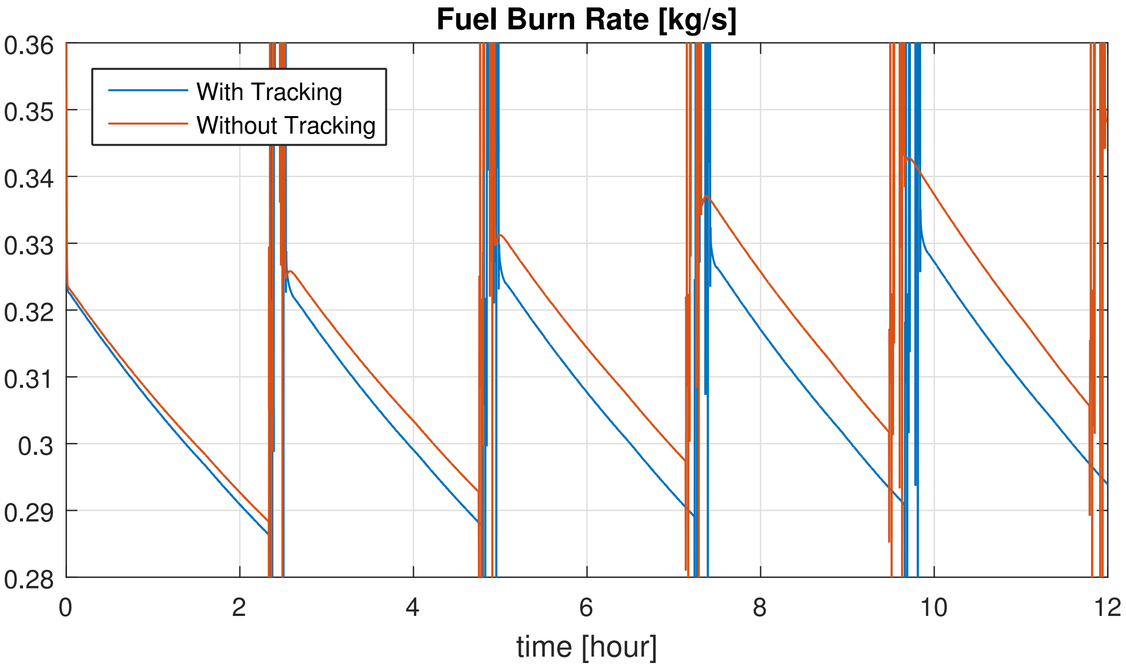

Figure 6.5. Fuel Burn Rate.

CHAPTER 7

CONCLUSION AND FUTURE WORK

The high fidelity simulation environment developed can successfully simulate various coronet missions for one or multiple receivers escorted by a tanker. The results generated by the simulations are adequate for quantifying the feasibility and the benefit of formation flight at sweet spot in coronet missions. Both the F-15C and the F-15E have the control authority to fly at the sweet spot and maneuver within the wake. The only exception observed is the case of a heavy F-15E right behind a heavy tanker, when the F-15E experiences thrust saturation since the aircraft is full weight and it is in the strong downwash region of the heavy tanker's wake. Significant fuel savings are obtained by flying receivers at the sweet spots of a tanker aircraft in Coronet missions. The F-15E can obtain a higher percent fuel saving compared to the F-15C. Flying two receivers at the sweet spots of a tanker compared to one receiver results in not only more fuel saved, but also a higher percentage relative to the case of aircraft flying out of the wake. Changing the trimming method has a very small effect on fuel burn. The results show that to take advantage of formation flight the sweet spot should be tracked. The benefit of sweet spot tracking increases when the tanker is light. When receivers fly at the sweet spots, they can fly longer before refueling. This can potentially eliminate the number of refueling needed, which leads to further fuel saving because the aircraft will not need to fly in the downwash region of the tanker and fly light longer. The smaller number of refueling needed may further potentially eliminate the number of tankers needed in missions requiring sequencing of multiple tankers.

In the coronet missions simulated in this thesis, the initial weight of the tanker is kept constant. However, it is known that the amount of fuel the tanker aircraft take off with depends on the specifics of the mission such as flight time, the number and type of receivers. Thus, the initial fuel amount should be adjusted depending on such mission specifics to better quantify the formation flight benefit. In the current project, only one tanker aircraft is considered and the simulation is stopped when the tanker is low on fuel. A follow-up study should be carried out to simulate sequence of multiple tankers for the same set of receivers for missions involving longer range than one tanker can provide. Other coronet missions that should be simulated may include (1) a fleet of multiple tankers and more than two receivers, (2) tanker-tanker formation, and (3) more than two receivers flying in the wake of one tanker. Another direction for future research is for developing simple formation analysis tools based on high fidelity dynamic simulation results obtained in this study. The simulations results can be used to construct simple relations/formulations/tables that can be used in operation analysis and mission planning.

APPENDIX A

DERIVATIVES OF MATRIX PRODUCTS

This section outlines how to take the partial derivatives of matrices with respect to a vector of multiple variables.

Suppose

$$y(x) = \mathbf{A}(x)v(x) \tag{A.1}$$

where $y(x) \epsilon \Re^{n\times 1}$, $\mathbf{A}(x) \epsilon \Re^{n\times n}$, $v \epsilon \Re^{n\times 1}$ and $x \epsilon \Re^{m\times 1}$. The derivative of $y(x)$ with respect to x is then defined by

$$\frac{\partial y}{\partial x} = \begin{bmatrix} \frac{\partial y}{\partial x_1} & \frac{\partial y}{\partial x_2} & \dots & \frac{\partial y}{\partial x_m} \end{bmatrix} \tag{A.2}$$

$$\frac{\partial y}{\partial x_i} = \frac{\partial \mathbf{A}}{\partial x_i} v + \mathbf{A}\frac{\partial v}{\partial x_i} \tag{A.3}$$

Plugging A.3 into A.2

$$\begin{aligned} \frac{\partial y}{\partial x} &= \begin{bmatrix} \frac{\partial \mathbf{A}}{\partial x_1} v + \mathbf{A}\frac{\partial v}{\partial x_1} & \frac{\partial \mathbf{A}}{\partial x_2} v + \mathbf{A}\frac{\partial v}{\partial x_2} & \dots & \frac{\partial \mathbf{A}}{\partial x_m} + \mathbf{A}\frac{\partial v}{\partial x_m} \end{bmatrix} \\ &= \begin{bmatrix} \frac{\partial \mathbf{A}}{\partial x_1} v & \frac{\partial \mathbf{A}}{\partial x_2} v & \dots & \frac{\partial \mathbf{A}}{\partial x_m} v \end{bmatrix} + \begin{bmatrix} \mathbf{A}\frac{\partial v}{\partial x_1} & \mathbf{A}\frac{\partial v}{\partial x_2} & \dots & \mathbf{A}\frac{\partial v}{\partial x_m} \end{bmatrix} \end{aligned} \tag{A.4}$$

$$\tag{A.5}$$

$$\frac{\partial y}{\partial x} = \frac{\partial \mathbf{A}}{\partial x}\mathbf{V_v} + \mathbf{A}\frac{\partial v}{\partial x} \tag{A.6}$$

where

$$\frac{\partial \mathbf{A}}{\partial x} = \begin{bmatrix} \frac{\partial \mathbf{A}}{\partial x_1} & \frac{\partial \mathbf{A}}{\partial x_2} & \dots & \frac{\partial \mathbf{A}}{\partial x_m} \end{bmatrix} \tag{A.7}$$

and

$$\mathbf{V_v} = \begin{bmatrix} v & 0_{n\times 1} & 0_{n\times 1} \dots 0_{n\times 1} & 0_{n\times 1} \\ 0_{n\times 1} & v & 0_{n\times 1} \dots 0_{n\times 1} & 0_{n\times 1} \\ \vdots & & & \vdots \\ 0_{n\times 1} & 0_{n\times 1} & 0_{n\times 1} \dots & v & 0_{n\times 1} \\ 0_{n\times 1} & 0_{n\times 1} & 0_{n\times 1} \dots 0_{n\times 1} & v \end{bmatrix} \tag{A.8}$$

For a more general case suppose that

$$\mathbf{A}(x) = \mathbf{B}(x)\mathbf{C}(x) \tag{A.9}$$

where $\mathbf{A}(x) \,\epsilon\, \Re^{n\times n}$, $\mathbf{B}(x) \,\epsilon\, \Re^{n\times n}$, $\mathbf{C}(x) \,\epsilon\, \Re^{n\times n}$ and $x \,\epsilon\, \Re^{m\times 1}$. The derivative of $\mathbf{A}(x)$ with respect to x is then defined by

$$\frac{\partial \mathbf{A}}{\partial x} = \left[\frac{\partial \mathbf{A}}{\partial x_1} \; \frac{\partial \mathbf{A}}{\partial x_2} \; \dots \; \frac{\partial \mathbf{A}}{\partial x_m}\right] \tag{A.10}$$

$$\frac{\partial \mathbf{A}}{\partial x_i} = \frac{\partial \mathbf{B}}{\partial x_i}\mathbf{C} + \mathbf{B}\frac{\partial \mathbf{C}}{\partial x_i} \tag{A.11}$$

Plugging A.11 into A.10

$$\begin{aligned}\frac{\partial \mathbf{A}}{\partial x} &= \left[\frac{\partial \mathbf{B}}{\partial x_1}\mathbf{C} + \mathbf{B}\frac{\partial \mathbf{C}}{\partial x_1} \quad \frac{\partial \mathbf{B}}{\partial x_2}\mathbf{C} + \mathbf{B}\frac{\partial \mathbf{C}}{\partial x_2} \quad \dots \quad \frac{\partial \mathbf{B}}{\partial x_m}\mathbf{C} + \mathbf{B}\frac{\partial \mathbf{C}}{\partial x_m}\right] \\ &= \left[\frac{\partial \mathbf{B}}{\partial x_1}\mathbf{C} \quad \frac{\partial \mathbf{B}}{\partial x_2}\mathbf{C} \quad \dots \quad \frac{\partial \mathbf{B}}{\partial x_m}\mathbf{C}\right] + \left[\mathbf{B}\frac{\partial \mathbf{C}}{\partial x_1} \quad \mathbf{B}\frac{\partial \mathbf{C}}{\partial x_2} \quad \dots \quad \mathbf{B}\frac{\partial \mathbf{C}}{\partial x_m}\right] \quad \text{(A.12)} \\ \frac{\partial \mathbf{A}}{\partial x} &= \frac{\partial \mathbf{B}}{\partial x}\mathbf{V_C} + \mathbf{B}\frac{\partial \mathbf{C}}{\partial x} \quad \text{(A.13)}\end{aligned}$$

where

$$\mathbf{V_C} = \begin{bmatrix} \mathbf{C} & 0_{n\times n} & 0_{n\times n} & \dots & 0_{n\times n} & 0_{n\times n} \\ 0_{n\times n} & \mathbf{C} & 0_{n\times n} & \dots & 0_{n\times n} & 0_{n\times n} \\ \vdots & & & & & \vdots \\ 0_{n\times n} & 0_{n\times n} & 0_{n\times n} & \dots & \mathbf{C} & 0_{n\times n} \\ 0_{n\times n} & 0_{n\times n} & 0_{n\times n} & \dots & 0_{n\times n} & \mathbf{C} \end{bmatrix} \quad \text{(A.14)}$$

Suppose it is desired to take the partial derivative of an inverse matrix with respect to a vector of multiple variables

$$\frac{\partial}{\partial x}\mathbf{A}^{-1} = -\mathbf{A}^{-1}\frac{\partial}{\partial x}\mathbf{A}\mathbf{V}_{\mathbf{A}^{-1}} \quad \text{(A.15)}$$

where

$$\mathbf{V_{A^{-1}}} = \begin{bmatrix} \mathbf{A^{-1}}\ 0_{n\times n}\ 0_{n\times n} \ldots 0_{n\times n}\ 0_{n\times n} \\ \\ 0_{n\times n}\ \mathbf{A^{-1}}\ 0_{n\times n} \ldots 0_{n\times n}\ 0_{n\times n} \\ \\ \vdots \qquad\qquad\qquad\qquad \vdots \\ \\ 0_{n\times n}\ 0_{n\times n}\ 0_{n\times n} \ldots \mathbf{A^{-1}}\ 0_{n\times n} \\ \\ 0_{n\times n}\ 0_{n\times n}\ 0_{n\times n} \ldots 0_{n\times n}\ \mathbf{A^{-1}} \end{bmatrix} \tag{A.16}$$

APPENDIX B

SKEW SYMMETRIC OPERATION

The skew symmetric matrix operation is used in place of cross products. It allows for having a matrix product instead of a cross product. Then the skew symmetric operation $\mathbf{S}(a)$ is defined as

$$a \times b = -\mathbf{S}(a)\ b \tag{B.1}$$

Let

$$a = \begin{bmatrix} a_1 \\ a_2 \\ a_3 \end{bmatrix} \tag{B.2}$$

Then

$$\mathbf{S}(a) = \begin{bmatrix} 0 & a_3 & -a_2 \\ -a_3 & 0 & a_1 \\ a_2 & -a_1 & 0 \end{bmatrix} \tag{B.3}$$

APPENDIX C

LINEARIZATION

C.1 Translational and Rotational Dynamics

The equations to be linearized for the **A** and **B** matrices are Eqs. (2.1) and (2.2), which are rewritten to indicate the dependencies of f_1, f_2, c_1, and c_2 on state vector x and applied force/moment vector v as

$$\dot{\mathcal{X}}_{\mathcal{R}} = \mathbf{f_1}(x)\dot{\omega}_{B_RB_T} + c_1(x,v) \tag{C.1}$$

$$\dot{\omega}_{B_RB_T} = \mathbf{f_2}(x)\dot{\mathcal{X}}_{\mathcal{R}} + c_2(x,v) \tag{C.2}$$

$$\Delta\dot{\mathcal{X}}_{\mathcal{R}} = \frac{\partial\dot{\mathcal{X}}_{\mathcal{R}}}{\partial x}\Delta x + \frac{\partial\dot{\mathcal{X}}_{\mathcal{R}}}{\partial v}\Delta v + \frac{\dot{\mathcal{X}}_{\mathcal{R}}}{\partial\dot{\omega}_{B_RB_T}}\Delta\dot{\omega}_{B_RB_T} \tag{C.3}$$

$$\Delta\dot{\omega}_{B_RB_T} = \frac{\partial\dot{\omega}_{B_RB_T}}{\partial x}\Delta x + \frac{\partial\dot{\omega}_{B_RB_T}}{\partial v}\Delta v + \frac{\partial\dot{\omega}_{B_RB_T}}{\partial\dot{\mathcal{X}}_{\mathcal{R}}}\Delta\dot{\mathcal{X}}_{\mathcal{R}} \tag{C.4}$$

The method for the derivatives of matrix products outlined in Appendix A is used to take the partial derivatives.

$$\frac{\partial\dot{\mathcal{X}}_{\mathcal{R}}}{\partial x} = \frac{\partial}{\partial x}\left[\mathbf{f_1}(x)\dot{\omega}_{B_RB_T}\right] + \frac{\partial}{\partial x}c_1(x,v) \tag{C.5}$$

$$\frac{\partial}{\partial x}\left[\mathbf{f_1}(x)\dot{\omega}_{B_RB_T}\right] = \frac{\partial\mathbf{f_1}(x)}{\partial x}\mathbf{V}_{\dot{\omega}_{\mathbf{B_RB_T}}} \tag{C.6}$$

where $\mathbf{V}_{\dot{\omega}_{\mathbf{B_RB_T}}}$ is a 36x12 matrix constructed by using the "V-matrix" operation defined in Eqs. (A.8) and (A.14). This operation will be used throughout this section. The term in the subscript is the term that the operation will be performed on, unless noted otherwise.

$$\frac{\partial\mathbf{f_1}(x)}{\partial x} = -\frac{\partial\mathcal{E}_R^{-1}}{\partial x}\mathbf{V}_{\mathbf{S}(\rho_{\mathbf{cm,t}})} \tag{C.7}$$

$$\frac{\partial\mathcal{E}_R^{-1}}{\partial x} = \begin{bmatrix} \frac{\partial\mathcal{E}_R^{-1}}{\partial V} & \frac{\partial\mathcal{E}_R^{-1}}{\partial\alpha} & \frac{\partial\mathcal{E}_R^{-1}}{\partial\beta} & 0_{3\times17} \end{bmatrix} \tag{C.8}$$

where $\mathbf{S}(\rho_{cm,t})$ is the skew symmetric operation on $\rho_{cm,t}$ defined in Appendix B. The skew symmetric operation is used throughout this section and is denoted by **S**.

$$\frac{\partial\dot{\mathcal{X}}_{\mathcal{R}}}{\partial v} = \frac{\partial c_1(x,v)}{\partial v} \tag{C.9}$$

$$\frac{\partial\dot{\mathcal{X}}_{\mathcal{R}}}{\partial\dot{\omega}_{B_RB_T}} = \mathbf{f_1}(x) \tag{C.10}$$

Putting the equations together

$$\begin{aligned}\Delta\dot{\mathcal{X}}_{\mathcal{R}} &= \left[-\frac{\partial \mathcal{E}_R^{-1}}{\partial x}\mathbf{V}_{\mathbf{S}(\rho_{\mathbf{cm,t}})}\mathbf{V}_{\dot{\omega}_{\mathbf{B_R B_T}}} + \frac{\partial c_1(x,v)}{\partial x}\right]\Delta x \\ &\quad + \frac{\partial c_1(x,v)}{\partial v}\Delta v + \mathbf{f_1}(x)\Delta\dot{\omega}_{B_R B_T}\end{aligned} \tag{C.11}$$

Next, the partial derivatives in Eq. (C.4) are worked out.

$$\frac{\partial \dot{\omega}_{B_R B_T}}{\partial x} = \frac{\partial}{\partial x}\left[\mathbf{f_2}(x)\dot{\omega}_{B_R B_T}\right] + \frac{\partial}{\partial x}c_2(x,v) \tag{C.12}$$

$$\frac{\partial}{\partial x}\left[\mathbf{f_2}(x)\dot{\omega}_{B_R B_T}\right] = \frac{\mathbf{f_2}(x)}{\partial x}\mathbf{V}_{\dot{\omega}_{\mathbf{B_R B_T}}} \tag{C.13}$$

$$\frac{\partial \mathbf{f_2}(\mathbf{x})}{\partial x} = \underline{\underline{\mathbf{I}}}_{\mathbf{t}}^{-\mathbf{1}} m_t \mathbf{S}(\rho_{cm,t})\frac{\partial \mathcal{E}_R}{\partial x} \tag{C.14}$$

$$\frac{\partial \dot{\omega}_{B_R B_T}}{\partial v} = \frac{\partial c_2}{\partial v} \tag{C.15}$$

$$\frac{\partial \dot{\omega}_{BR}}{\partial \dot{\mathcal{X}}_R} = \mathbf{f_2}(x) \tag{C.16}$$

Putting the equations together

$$\begin{aligned}\Delta\dot{\omega}_{B_R B_T} &= \left[\underline{\underline{\mathbf{I}}}_{\mathbf{t}}^{-\mathbf{1}} m_t \mathbf{S}(\rho_{cm,t})\frac{\partial \mathcal{E}_R}{\partial x}\mathbf{V}_{\dot{\omega}_{\mathbf{B_R B_T}}} + \frac{\partial c_2(x,v)}{\partial x}\right]\Delta x \\ &\quad + \frac{\partial c_2(x,v)}{\partial v}\Delta v + \mathbf{f_2}(x)\Delta\dot{\mathcal{X}}_{\mathcal{R}}\end{aligned} \tag{C.17}$$

Assuming constant mass and inertia and no wind, Eqs. (2.7) and (2.9) become

$$\begin{aligned}c_1 &= \mathcal{E}_{\mathbf{R}}^{-\mathbf{1}}\Bigg\{\frac{1}{m_t}F_{B_R} + \Big[\mathbf{S}(\omega_{\mathbf{B_R B_T}} + \mathbf{R_{B_R B_T}}\omega_{\mathbf{B_T}})\Big]\big(\mathbf{R_{B_R W_R}}\,U\big) \\ &\quad - \Big[\mathbf{S^2}(\omega_{\mathbf{B_R B_T}} + \mathbf{R_{B_R B_T}}\omega_{\mathbf{B_T}}) - \mathbf{S}\left(\mathbf{S}(\omega_{B_R B_T})\mathbf{R_{B_R B_T}}\omega_{B_T}\right) \\ &\quad - \mathbf{S}(\mathbf{R_{B_R B_T}}\dot{\omega}_{B_T})\Big]\rho_{cm,t}\Bigg\}\end{aligned} \tag{C.18}$$

$$\begin{aligned}c_2 &= \underline{\underline{\mathbf{I}}}_{\mathbf{t}}^{-\mathbf{1}} M_{B_R} + \underline{\underline{\mathbf{I}}}_{\mathbf{t}}^{-\mathbf{1}}\mathbf{S}\big(\omega_{B_R B_T} + \mathbf{R_{B_R B_T}}\omega_{B_T}\big)\underline{\underline{\mathbf{I}}}_{\mathbf{t}}\big(\omega_{B_R B_T} + \mathbf{R_{B_R B_T}}\omega_{B_T}\big) \\ &\quad - m_t \underline{\underline{\mathbf{I}}}_{\mathbf{t}}^{-\mathbf{1}}\mathbf{S}\big(\rho_{cm,t}\big)\mathbf{S}\big(\omega_{B_R B_T} + \mathbf{R_{B_R B_T}}\omega_{B_T}\big)\mathbf{R_{B_R W_R}}U \\ &\quad - \mathbf{S}\big(\omega_{B_R B_T}\big)\mathbf{R_{B_R B_T}}\omega_{B_T} - \mathbf{R_{B_R B_T}}\dot{\omega}_{B_T}\end{aligned} \tag{C.19}$$

The partial derivatives of c_1 and c_2 needed in Eqs. (C.11) and (C.17), respectively, are formulated below using Eqs. (C.18) and (C.19).

$$\frac{\partial c_1}{\partial v} = \left[\frac{1}{m_t}\mathcal{E}_R^{-1} \;\; \mathbf{0_{3\times 3}}\right] \tag{C.20}$$

$$\frac{\partial c_2}{\partial v} = \left[\mathbf{0_{3\times 3}} \;\; \underline{\underline{\mathbf{I}}}_{\mathbf{t}}^{\mathbf{-1}}\right] \tag{C.21}$$

Splitting c_1 into 3 parts to simplify differentiation gives

$$L_1 = \frac{1}{m_t}\mathcal{E}_R^{-1}F_{B_R} \tag{C.22}$$

$$L_2 = \mathcal{E}_R^{-1}\mathbf{S}(\omega_{B_RB_T} + \mathbf{R_{B_RB_T}}\omega_{BT})\mathbf{R_{B_RW_R}}U \tag{C.23}$$

$$L_3 = -\mathcal{E}_R^{-1}\Big[\mathbf{S}^2(\omega_{B_RB_T} + \mathbf{R_{B_RB_T}}\omega_{B_T}) - \mathbf{S}\big(\mathbf{S}(\omega_{B_RB_T})\mathbf{R_{B_RB_T}}\omega_{B_T}\big) \tag{C.24}$$

$$-\mathbf{S}(\mathbf{R_{B_RB_T}}\dot{\omega}_{B_T})\Big]\rho_{cm,t} \tag{C.25}$$

The partial derivatives of each of L_1, L_2, and L_3 are formulated below.

$$\frac{\partial L_1}{\partial x} = \frac{1}{m_t}\frac{\partial \mathcal{E}_R^{-1}}{\partial x}\mathbf{V_{F_{B_R}}} \tag{C.26}$$

Writing L_2 as

$$L_2 = \mathcal{E}_{\mathbf{R}}^{\mathbf{-1}}L_{21} \tag{C.27}$$

where

$$L_{21} = \mathbf{S}(\omega_{B_RB_T} + \mathbf{R_{B_RB_T}}\omega_{B_T})\mathbf{R_{B_RW_R}}U \tag{C.28}$$

$$\begin{aligned}
\frac{\partial L_{21}}{\partial x} &= \frac{\partial}{\partial x}\big[\mathbf{S}(\omega_{B_RB_T} + \mathbf{R_{B_RB_T}}\omega_{B_T})\mathbf{R_{B_RB_T}}\big]\mathbf{V_U} + \mathbf{S}(\omega_{B_RB_T} + \mathbf{R_{B_RB_T}}\omega_{B_T})\mathbf{R_{B_RB_T}}\frac{\partial U}{\partial x} \\
&= \left\{\mathbf{S}\Big(\frac{\partial}{\partial x}\big[\omega_{B_RB_T} + \mathbf{R_{B_RB_T}}\omega_{B_T}\big]\Big)\mathbf{V_{R_{B_RB_T}}} + \mathbf{S}(\omega_{B_RB_T} + \mathbf{R_{B_RB_T}}\omega_{B_T})\frac{\partial \mathbf{R_{B_RW_R}}}{\partial x}\right\}\mathbf{V_U} \\
&\quad + \mathbf{S}(\omega_{B_RB_T} + \mathbf{R_{B_RB_T}}\omega_{B_T})\mathbf{R_{B_RB_T}}\frac{\partial U}{\partial x}
\end{aligned} \tag{C.29}$$

$\frac{\partial L_2}{\partial x}$ in Eq. (C.27) is then

$$\frac{\partial L_2}{\partial x} = \frac{\partial \mathcal{E}_R^{-1}}{\partial x}\mathbf{V_{L_{21}}} + \mathcal{E}_R^{-1}\frac{\partial L_{21}}{\partial x} \tag{C.30}$$

To facilitate its partial derivation, L_3 is split up into three components such that

$$\begin{aligned} L_3 &= -\mathcal{E}_R^{-1}\big[\mathbf{S_1} - \mathbf{S_2} - \mathbf{S_3}\big]\rho_{cm,t} && \text{(C.31)}\\ \mathbf{S_1} &= \mathbf{S}^2(\omega_{B_RB_T} + \mathbf{R_{B_RB_T}}\omega_{B_T}) && \text{(C.32)}\\ \mathbf{S_2} &= \mathbf{S}\big(\mathbf{S}(\omega_{B_RB_T})\mathbf{R_{B_RB_T}}\omega_{B_T}\big) && \text{(C.33)}\\ \mathbf{S_3} &= \mathbf{S}(\mathbf{R_{B_RB_T}}\dot{\omega}_{B_T}) && \text{(C.34)} \end{aligned}$$

The partial derivatives are then

$$\begin{aligned} \frac{\partial \mathbf{S_1}}{\partial x} &= \mathbf{S}\big(\frac{\partial}{\partial x}\big[\omega_{B_RB_T} + \mathbf{R_{B_RB_T}}\omega_{B_T}\big]\big)\mathbf{V}_{\mathbf{S}(\omega_{\mathbf{B_RB_T}}+\mathbf{R_{B_RB_T}}\omega_{\mathbf{B_T}})}\\ &\quad +\mathbf{S}(\omega_{B_RB_T} + \mathbf{R_{B_RB_T}}\omega_{\mathbf{B_T}})\mathbf{S}\big(\frac{\partial}{\partial x}\big[\omega_{B_RB_T}\\ &\quad +\mathbf{R_{B_RB_T}}\omega_{B_T}\big]\big) && \text{(C.35)} \end{aligned}$$

where $\mathbf{V_S}$ is a 36x36 matrix constructed by performing the V-Matrix operation on $\mathbf{S}(\omega_{B_RB_T} + \mathbf{R_{B_RB_T}}\omega_{B_T})$.

$$\begin{aligned} \frac{\partial \mathbf{S_2}}{\partial x} &= \mathbf{S}\Bigg(\mathbf{S}(\frac{\partial \omega_{B_RB_T}}{\partial x})\mathbf{V_{R_{B_RB_T}}}\omega_{\mathbf{B_T}}\\ &\quad +\mathbf{S}(\omega_{B_RB_T})\frac{\partial}{\partial x}[\mathbf{R_{B_RB_T}}\omega_{B_T}]\Bigg) && \text{(C.36)}\\ \frac{\partial \omega_{B_RB_T}}{\partial x} &= \Big[0_{3\times3} \quad \mathbf{I}_{3\times3} \quad 0_{3\times6}\Big] && \text{(C.37)}\\ \frac{\partial}{\partial x}[\mathbf{R_{B_RB_T}}\omega_{B_T}] &= \Bigg[0_{3\times6} \quad \frac{\partial \mathbf{R_{B_RB_T}}}{\partial \psi}\omega_{B_T} \quad \frac{\partial \mathbf{R_{B_RB_T}}}{\partial \theta}\omega_{B_T} \quad \frac{\partial \mathbf{R_{B_RB_T}}}{\partial \phi}\omega_{B_T}\\ &\quad 0_{3\times3}\Bigg] && \text{(C.38)}\\ \frac{\partial \mathbf{S_3}}{\partial x} &= \mathbf{S}\Bigg(\frac{\partial}{\partial x}[\mathbf{R_{B_RB_T}}\dot{\omega}_{B_T}]\Bigg)\\ &= \Bigg[0_{3\times18} \quad \mathbf{S}\Bigg(\frac{\partial \mathbf{R_{B_RB_T}}}{\partial \psi}\dot{\omega}_{B_T}\Bigg) \quad \mathbf{S}\Bigg(\frac{\partial \mathbf{R_{B_RB_T}}}{\partial \theta}\dot{\omega}_{B_T}\Bigg)\\ &\quad \mathbf{S}\Bigg(\frac{\partial \mathbf{R_{B_RB_T}}}{\partial \phi}\dot{\omega}_{B_T}\Bigg) \quad 0_{3\times9}\Bigg] && \text{(C.39)} \end{aligned}$$

$\frac{\partial L_3}{\partial x}$ is then

$$\frac{\partial L_3}{\partial x} = -\left[\frac{\partial \mathcal{E}_R^{-1}}{\partial x}\mathbf{V}_{\mathbf{S_{123}}} + \mathcal{E}_R^{-1}\left(\frac{\partial \mathbf{S_1}}{\partial x} - \frac{\partial \mathbf{S_2}}{\partial x} - \frac{\partial \mathbf{S_3}}{\partial x}\right)\right]\mathbf{V}_{\rho_{\mathbf{cm,t}}} \tag{C.40}$$

where $\mathbf{V}_{\mathbf{S_{123}}}$ is a 36x36 matrix constructed by performing the V-Matrix operation on $\mathbf{S_1} - \mathbf{S_2} - \mathbf{S_3}$. $\frac{\partial c_1}{\partial x}$ is then

$$\frac{\partial c_1}{\partial x} = \frac{\partial L_1}{\partial x} + \frac{\partial L_2}{\partial x} + \frac{\partial L_3}{\partial x} \tag{C.41}$$

where $\frac{\partial L_1}{\partial x}$, $\frac{\partial L_2}{\partial x}$, and $\frac{\partial L_2}{\partial x}$ are given in Eqs. (C.26), (C.30), and (C.40), respectively. Similarly c_2 is split into several components to facilitate its partial derivation such that

$$c_2 = \underline{\underline{\mathbf{I}}}_{\mathbf{t}}^{\mathbf{-1}} M_{B_R} + Y_1 - Y_2 - Y_3 \tag{C.42}$$

$$Y_1 = \underline{\underline{\mathbf{I}}}_{\mathbf{t}}^{\mathbf{-1}}\mathbf{S}\big(\omega_{B_R B_T} + \mathbf{R_{B_R B_T}}\omega_{B_T}\big)\underline{\underline{\mathbf{I}}}_{\mathbf{t}}\big(\omega_{B_R B_T} + \mathbf{R_{B_R B_T}}\omega_{B_T}\big) \tag{C.43}$$

$$Y_2 = m_t \underline{\underline{\mathbf{I}}}_{\mathbf{t}}^{\mathbf{-1}}\mathbf{S}\big(\rho_{cm,t}\big)\mathbf{S}\big(\omega_{B_R B_T} + \mathbf{R_{B_R B_T}}\omega_{B_T}\big)\mathbf{R_{B_R W_R}} U \tag{C.44}$$

$$Y_3 = \mathbf{S}\big(\omega_{B_R B_T}\big)\mathbf{R_{B_R B_T}}\omega_{B_T} - \mathbf{R_{B_R B_T}}\dot{\omega}_{B_T} \tag{C.45}$$

$$\begin{aligned}\frac{\partial Y_1}{\partial x} = \underline{\underline{\mathbf{I}}}_{\mathbf{t}}^{\mathbf{-1}}\Big[&\frac{\partial}{\partial x}\mathbf{S}\big(\omega_{B_R B_T} + \mathbf{R_{B_R B_T}}\omega_{B_T}\big)\mathbf{V}_{\underline{\underline{\mathbf{I}}}_{\mathbf{t}}(\omega_{\mathbf{B_R B_T}} + \mathbf{R_{B_R B_T}}\omega_{\mathbf{B_T}})} \\ &+\mathbf{S}\big(\omega_{B_R B_T} + \mathbf{R_{B_R B_T}}\omega_{B_T}\big)\underline{\underline{\mathbf{I}}}_{\mathbf{t}}\frac{\partial}{\partial x}\big(\omega_{B_R B_T} + \mathbf{R_{B_R B_T}}\omega_{B_T}\big)\Big]\end{aligned} \tag{C.46}$$

where $\frac{\partial}{\partial x}\mathbf{S}\big(\omega_{B_R B_T} + \mathbf{R_{B_R B_T}}\omega_{B_T}\big)$ is given as

$$\frac{\partial}{\partial x}\mathbf{S}\big(\omega_{B_R B_T} + \mathbf{R_{B_R B_T}}\omega_{B_T}\big) = \mathbf{S}\big(\frac{\partial}{\partial x}[\omega_{B_R B_T} + \mathbf{R_{B_R B_T}}\omega_{B_T}]\big) \tag{C.47}$$

The components of $\frac{\partial}{\partial x}\big(\omega_{B_R B_T} + \mathbf{R_{B_R B_T}}\omega_{B_T}\big)$ are given in Eqs. (C.37) and (C.38).

$$\frac{\partial Y_2}{\partial x} = m_t \underline{\underline{\mathbf{I}}}_{\mathbf{t}}^{\mathbf{-1}}\mathbf{S}(\rho_{cm,t})\frac{\partial L_{21}}{\partial x} \tag{C.48}$$

where $\frac{\partial L_{21}}{\partial x}$ is given in Eq. (C.29).

$$\frac{\partial Y_3}{\partial x} = \frac{\partial}{\partial x}\Big[\mathbf{S}\big(\omega_{B_R B_T}\big)\mathbf{R_{B_R B_T}}\omega_{B_T}\Big] - \frac{\partial \mathbf{R_{B_R B_T}}}{\partial x}\mathbf{V}_{\dot{\omega}_{\mathbf{B_T}}} \tag{C.49}$$

where $\frac{\partial}{\partial x}\Big[\mathbf{S}\big(\omega_{B_RB_T}\big)\mathbf{R}_{\mathbf{B_RB_T}}\omega_{B_T}\Big]$ is given in Eq. (C.50) and $\frac{\partial \mathbf{R}_{\mathbf{B_RB_T}}}{\partial x}$ is in Eq. (C.51).

$$
\begin{aligned}
\frac{\partial}{\partial x}\Big[\mathbf{S}\big(\omega_{B_RB_T}\big)\mathbf{R}_{\mathbf{B_RB_T}}\omega_{B_T}\Big] \quad &= \quad \mathbf{S}(\frac{\partial \omega_{B_RB_T}}{\partial x})\mathbf{V}_{\mathbf{R_{B_RB_T}\omega_{B_T}}} \\
&\quad +\mathbf{S}(\omega_{B_RB_T})\frac{\partial}{\partial x}[R_{B_RB_T}\omega_{B_T}]
\end{aligned}
\tag{C.50}
$$

where $\frac{\partial \omega_{B_RB_T}}{\partial x}$ is given in Eq. (C.37) and $\frac{\partial}{\partial x}[R_{B_RB_T}\omega_{B_T}$ is given in Eq. (C.38).

$$
\frac{\partial \mathbf{R}_{\mathbf{B_RB_T}}}{\partial x} \quad = \quad \begin{bmatrix} 0_{3\times 18} & \dfrac{\partial R_{B_RB_T}}{\partial \psi} & \dfrac{\partial R_{B_RB_T}}{\partial \theta} & \dfrac{\partial R_{B_RB_T}}{\partial \phi} & 0_{3\times 9} \end{bmatrix} \tag{C.51}
$$

$$
\frac{\partial c_2}{\partial x} = \frac{\partial Y_1}{\partial x} - \frac{\partial Y_2}{\partial x} - \frac{\partial Y_3}{\partial x} \tag{C.52}
$$

Recall from Eqs. (C.11) and (C.17) that $\Delta\dot{\omega}_{B_RB_T}$ appears in the $\Delta\dot{\mathcal{X}}_R$ equation and vice versa. In the following, the linearized equations are put in state-space form. Substituting Eq. (C.17) into Eq. (C.11) yields

$$
\begin{aligned}
\Delta\dot{\mathcal{X}}_R \quad = \quad & \Big[-\frac{\partial \mathcal{E}_R^{-1}}{\partial x}\mathbf{V}_{\mathbf{S}_{\rho_{cm,t}}}\mathbf{V}_{\dot{\omega}_{B_RB_T}} + \frac{\partial c_1}{\partial x}\Big]\Delta x \\
& +\frac{\partial c_1}{\partial v}\Delta v \\
& +\mathbf{f_1}\Big[m_t\underline{\underline{\mathbf{I}}}_{\mathbf{t}}^{\mathbf{-1}}S(\rho_{cm,t})\frac{\partial \mathcal{E}_R}{\partial x}\mathbf{V}_{\dot{\omega}_{\mathbf{B_RB_T}}} + \frac{\partial c_2}{\partial x}\Big]\Delta x \\
& +\mathbf{f_1}\frac{\partial c_2}{\partial v}\Delta v + \mathbf{f_1}\mathbf{f_2}\Delta\dot{\mathcal{X}}_R
\end{aligned}
\tag{C.53}
$$

which is rearranged to have

$$
\begin{aligned}
\Big[\underline{\underline{\mathbf{I}}}_{\mathbf{3\times 3}} - \mathbf{f_1}\mathbf{f_2}\Big]\Delta\dot{\mathcal{X}}_R \quad = \quad & \Big\{\Big[-\frac{\partial \mathcal{E}_R^{-1}}{\partial x}\mathbf{V}_{\mathbf{S}(\boldsymbol{\rho}_{\mathbf{cm,t}})} + m_t\mathbf{f_1}\underline{\underline{\mathbf{I}}}_{\mathbf{t}}^{\mathbf{-1}}\mathbf{S}(\rho_{cm,t})\frac{\partial \mathcal{E}_R}{\partial x}\Big]\mathbf{V}_{\dot{\omega}_{\mathbf{B_RB_T}}} \\
& +\frac{\partial c_1}{\partial x} + \mathbf{f_1}\frac{\partial c_2}{\partial x}\Big\}\Delta x + \Big[\frac{\partial c_1}{\partial v} + \mathbf{f_1}\frac{\partial c_2}{\partial v}\Big]\Delta v
\end{aligned}
\tag{C.54}
$$

which is further rearranged to have

$$
\Delta\dot{\mathcal{X}}_R = \mathbf{A_x}\Delta x + \mathbf{B_x}\Delta v \tag{C.55}
$$

where

$$\begin{aligned}\mathbf{A_x} &= \left[I_{3\times3} - \mathbf{f_1 f_2}\right]^{-1}\Bigg\{\left[-\frac{\partial\mathcal{E}_R^{-1}}{\partial x}\mathbf{V}_{\mathbf{S}(\rho_{\mathbf{cm,t}})} + m_t \mathbf{f_1}\underline{\underline{\mathbf{I}}}_{\mathbf{t}}^{-\mathbf{1}}\mathbf{S}(\rho_{cm,t})\frac{\partial\mathcal{E}_R}{\partial x}\right]\mathbf{V}_{\dot\omega_{\mathbf{B_R B_T}}} \\ &\quad + \frac{\partial c_1}{\partial x} + \mathbf{f_1}\frac{\partial c_2}{\partial x}\Bigg\} \end{aligned} \tag{C.56}$$

$$\mathbf{B_x} = \left[I_{3\times3} - \mathbf{f_1 f_2}\right]^{-1}\left[\frac{\partial c_1}{\partial v} + \mathbf{f_1}\frac{\partial c_2}{\partial v}\right] \tag{C.57}$$

Similarly, substituting Eq. (C.11) into Eq. (C.17) leads to

$$\begin{aligned}\Delta\dot\omega_{B_R B_T} &= \left[m_t\underline{\underline{\mathbf{I}}}_{\mathbf{t}}^{-\mathbf{1}}\mathbf{S}(\rho_{cm,t})\frac{\partial\mathcal{E}_R}{\partial x}\mathbf{V}_{\dot\omega_{\mathbf{B_R B_T}}} + \frac{\partial c_2}{\partial x}\right]\Delta x \\ &\quad + \frac{\partial c_2}{\partial v}\Delta v \\ &\quad + \mathbf{f_2}\left[-\frac{\partial\mathcal{E}_R^{-1}}{\partial x}\mathbf{V}_{\mathbf{S}(\rho_{\mathbf{cm,t}})}\mathbf{V}_{\dot\omega_{\mathbf{B_R B_T}}} + \frac{\partial c_1}{\partial x}\right]\Delta x \\ &\quad + \mathbf{f_2}\frac{\partial c_1}{\partial v}\Delta v + \mathbf{f_2 f_1}\Delta\dot\omega_{B_R B_T} \end{aligned} \tag{C.58}$$

which is rearranged to have

$$\begin{aligned}\left[I_{3\times3} - \mathbf{f_2 f_1}\right]\Delta\dot\omega_{B_R B_T} &= \Bigg\{\left[m_t\underline{\underline{\mathbf{I}}}_{\mathbf{t}}^{-\mathbf{1}}\mathbf{S}(\rho_{cm,t})\frac{\partial\mathcal{E}_R}{\partial x} - \mathbf{f_2}\frac{\partial\mathcal{E}_R^{-1}}{\partial x}\mathbf{V}_{\mathbf{S}(\rho_{\mathbf{cm,t}})}\right]\mathbf{V}_{\dot\omega_{\mathbf{B_R B_T}}} \\ &\quad + \frac{\partial c_2}{\partial x} + \mathbf{f_2}\frac{\partial c_1}{\partial x}\Bigg\}\Delta x \\ &\quad + \left[\frac{\partial c_2}{\partial v} + \mathbf{f_2}\frac{\partial c_1}{\partial v}\right]\Delta v \end{aligned} \tag{C.59}$$

which is further rearranged to have

$$\Delta\dot\omega_{B_R B_T} = \mathbf{A}_\omega\Delta x + \mathbf{B}_\omega\Delta v \tag{C.60}$$

where

$$\begin{aligned}\mathbf{A}_\omega &= \left[I_{3\times3} - \mathbf{f_2 f_1}\right]^{-1}\Bigg\{\left[m_t\underline{\underline{\mathbf{I}}}_{\mathbf{t}}^{-\mathbf{1}}\mathbf{S}(\rho_{cm,t})\frac{\partial\mathcal{E}_R}{\partial x} - \mathbf{f_2}\frac{\partial\mathcal{E}_R^{-1}}{\partial x}\mathbf{V}_{\mathbf{S}(\rho_{\mathbf{cm,t}})}\right]\mathbf{V}_{\dot\omega_{\mathbf{B_R B_T}}} \\ &\quad + \frac{\partial c_2}{\partial x} + \mathbf{f_2}\frac{\partial c_1}{\partial x}\Bigg\} \end{aligned} \tag{C.61}$$

$$\mathbf{B}_\omega = \left[I_{3\times 3} - \mathbf{f_2 f_1} \right]^{-1} \left[\frac{\partial c_2}{\partial v} + \mathbf{f_2} \frac{\partial c_1}{\partial v} \right] \tag{C.62}$$

where note that $\mathbf{f_2 f_1} = -m_t \underline{\underline{\mathbf{I}}}_{\mathbf{t}}^{-\mathbf{1}} \mathbf{S}^2(\rho_{cm,t})$. When this identity is used, the above two equations can be rewritten to be

$$\begin{aligned} \mathbf{A}_\omega \;=\; & \left[I_{3\times 3} + m_t \underline{\underline{\mathbf{I}}}_{\mathbf{t}}^{-\mathbf{1}} \mathbf{S}^2(\rho_{cm,t}) \right]^{-1} \left\{ \left[m_t \underline{\underline{\mathbf{I}}}_{\mathbf{t}}^{-\mathbf{1}} \mathbf{S}(\rho_{cm,t}) \frac{\partial \mathcal{E}_R}{\partial x} - \mathbf{f_2} \frac{\partial \mathcal{E}_R^{-1}}{\partial x} \mathbf{V}_{\mathbf{S}(\rho_{\mathbf{cm,t}})} \right] \mathbf{V}_{\dot{\omega}_{\mathbf{B_R B_T}}} \right. \\ & \left. + \frac{\partial c_2}{\partial x} + \mathbf{f_2} \frac{\partial c_1}{\partial x} \right\} \end{aligned} \tag{C.63}$$

$$B_\omega = \left[I_{3\times 3} + m_t \underline{\underline{\mathbf{I}}}_{\mathbf{t}}^{-\mathbf{1}} \mathbf{S}^2(\rho_{cm,t}) \right]^{-1} \left[\frac{\partial c_2}{\partial v} + \mathbf{f_2} \frac{\partial c_1}{\partial v} \right] \tag{C.64}$$

C.2 Rotational Kinematics

The rotational kinematics in terms of 3-2-1 Euler angles is

$$\dot{\psi} = (q \sin\phi + r \cos\phi) \sec\theta \tag{C.65}$$

$$\dot{\theta} = q \cos\phi - r \sin\phi \tag{C.66}$$

$$\dot{\phi} = p + q \sin\phi \tan\theta + r \cos\phi \tan\theta \tag{C.67}$$

The matrix form of this is repeated from Eq. (2.14) as

$$\dot{E}_{\psi\theta\phi} = \mathbf{L}\, \omega_{B_R B_T} \tag{C.68}$$

where

$$E_{\psi\theta\phi} = \begin{bmatrix} \psi \\ \theta \\ \phi \end{bmatrix} \tag{C.69}$$

$$\mathbf{L} = \begin{bmatrix} 0 & \sin\theta\sec\theta & \cos\phi\sec\theta \\ 0 & \cos\phi & -\sin\phi \\ 1 & \sin\phi\tan\theta & \cos\phi\tan\theta \end{bmatrix} \tag{C.70}$$

$$\omega_{B_R B_T} = \begin{bmatrix} p \\ q \\ r \end{bmatrix} \tag{C.71}$$

The linearization of Eq. (C.68) should be in the form of

$$\Delta\dot{E}_{\psi\theta\phi} = \mathbf{A}_{\psi\theta\phi}\Delta x + \mathbf{B}_{\psi\theta\phi}\Delta v \tag{C.72}$$

Since $E_{\psi\theta\phi}$ does not depend on forces or moments

$$\mathbf{B}_{\psi\theta\phi} = \mathbf{0_{3\times6}} \tag{C.73}$$

$$\mathbf{A}_{\psi\theta\phi} = \frac{\partial\mathbf{L}}{\partial x}\mathbf{V}_{\omega_{\mathbf{B_R B_T}}} + \mathbf{L}\frac{\partial\omega_{B_R B_T}}{\partial x} \tag{C.74}$$

where $\frac{\partial\omega_{B_R B_T}}{\partial x}$ is given in Eq. (C.37).

C.3 Translational Kinematics

The translational kinematics from Eq. (2.16) is rewritten, without the wind term, as

$$\dot{\xi} = \mathbf{R^T_{B_R B_T}}\mathbf{R_{B_R W_R}}U - \mathbf{R_{B_T I}}\dot{r}_{B_T} + \mathbf{S}(\omega_{B_T})\xi \tag{C.75}$$

$$\Delta\dot{\xi} = \mathbf{A}_\xi\Delta x + \mathbf{B}_\xi\Delta v \tag{C.76}$$

ξ does not depend on forces or moments

$$\mathbf{B}_\xi = \mathbf{0_{3\times 6}} \tag{C.77}$$

Since the second term in Eq. (C.75) is of tanker variables,

$$\mathbf{A}_\xi \;=\; \frac{\partial}{\partial x}\left[\mathbf{R^T_{B_R B_T}} \mathbf{R_{B_R W_R}} U + \mathbf{S}(\omega_{B_T})\xi\right] \tag{C.78}$$

where

$$\begin{aligned}
\frac{\partial}{\partial x}\left[\mathbf{R^T_{B_R B_T}}\mathbf{R_{B_R W_R}}U\right] &= \frac{\partial}{\partial x}(\mathbf{R^T_{B_R B_T}}\mathbf{R_{B_R W_R}})V_U + \mathbf{R^T_{B_R B_T}}\mathbf{R_{B_R W_R}}\frac{\partial U}{\partial x} && \text{(C.79)}\\
\frac{\partial}{\partial x}(\mathbf{R^T_{B_R B_T}}\mathbf{R_{B_R W_R}}) &= \frac{\partial \mathbf{R^T_{B_R B_T}}}{\partial x}V_{\mathbf{R_{B_R W_R}}} + \mathbf{R^T_{B_R B_T}}\frac{\partial \mathbf{R_{B_R W_R}}}{\partial x} && \text{(C.80)}\\
\frac{\partial}{\partial x}\left[\mathbf{S}(\omega_{B_T})\xi\right] &= \mathbf{S}(\omega_{B_T})\frac{\partial \xi}{\partial x} && \text{(C.81)}\\
\frac{\partial \xi}{\partial x} &= \left[\mathbf{0_{3\times 9}}\ \mathbf{I_{3\times 3}}\right] && \text{(C.82)}\\
\frac{\partial}{\partial x}\left[\mathbf{S}(\omega_{\omega_{B_T}})\xi\right] &= \left[\mathbf{0_{3\times 9}}\ \mathbf{S}(\omega_{B_T})\right] && \text{(C.83)}
\end{aligned}$$

Putting the above equations back together leads to

$$\begin{aligned}
\mathbf{A}_\xi \;=\; & \left(\frac{\partial \mathbf{R^T_{B_R B_T}}}{\partial x}\mathbf{V_{R_{B_R W_R}}} + \mathbf{R^T_{B_R B_T}}\frac{\partial \mathbf{R_{B_R W_R}}}{\partial x}\right)\mathbf{V_U}\\
& + \mathbf{R^T_{B_R B_T}}\mathbf{R_{B_R W_R}}\frac{\partial U}{\partial x} + \left[\mathbf{0_{3\times 9}}\ \mathbf{S}(\omega_{B_T})\right]
\end{aligned} \tag{C.84}$$

where $\frac{\partial \mathbf{R^T_{B_R B_T}}}{\partial x}$ is given in Eq. (C.85), $\frac{\partial \mathbf{R_{B_R W_R}}}{\partial x}$ is given in Eq. (C.86) and $\frac{\partial U}{\partial x}$ is given in Eq. (C.87).

$$\begin{aligned}
\frac{\partial \mathbf{R^T_{B_R B_T}}}{\partial x} &= \begin{bmatrix} 0_{3\times 18} & \frac{\partial \mathbf{R_{B_R W_R}}}{\partial \psi} & \frac{\partial \mathbf{R_{B_R W_R}}}{\partial \theta} & \frac{\partial \mathbf{R_{B_R W_R}}}{\partial \phi} & 0_{3\times 9}\end{bmatrix} && \text{(C.85)}\\
\frac{\partial \mathbf{R_{B_R W_R}}}{\partial x} &= \begin{bmatrix} 0_{3\times 3} & \frac{\partial \mathbf{R_{B_R W_R}}}{\partial \beta} & \frac{\partial \mathbf{R_{B_R W_R}}}{\partial \alpha} & 0_{3\times 27}\end{bmatrix} && \text{(C.86)}\\
\frac{\partial U}{\partial x} &= \begin{bmatrix} 1 & 0_{1\times 11}\\ 0 & 0_{1\times 11}\\ 0 & 0_{1\times 11}\end{bmatrix} && \text{(C.87)}
\end{aligned}$$

C.4 Applied Force and Moment Expression

Next Eq. (2.12) is linearized, which is rewritten in compact form as

$$F_{B_R} = -\mathbf{R_{B_RW_R}}F_a + F_p + \mathbf{R_{B_RB_T}}\mathbf{R_{B_TI}}F_g \tag{C.88}$$

In the following, the partial derivatives of each term is taken separately.

$$\frac{\partial}{\partial x}\left[\mathbf{R_{B_RW_R}}F_a\right] = \frac{\partial \mathbf{R_{B_RW_R}}}{\partial x}\mathbf{V_a} + \mathbf{R_{B_RW_R}}\frac{\partial F_a}{\partial x} \tag{C.89}$$

where $\frac{\partial \mathbf{R_{B_RW_R}}}{\partial x}$ is formulated in Eq. (C.86).

$$\frac{\partial}{\partial x}\left[\mathbf{R_{B_RB_T}}\mathbf{R_{B_TI}}F_g\right] = \frac{\partial \mathbf{R_{B_RB_T}}}{\partial x}\mathbf{V_{R_{B_TI}F_g}} \tag{C.90}$$

where $\frac{\partial \mathbf{R_{B_RB_T}}}{\partial x}$ is formulated in Eq. (C.51). Putting everything together

$$\frac{\partial F_{B_R}}{\partial x} = -\frac{\partial \mathbf{R_{B_RW_R}}}{\partial x}\mathbf{V_{F_a}} - \mathbf{R_{B_RW_R}}\frac{\partial F_a}{\partial x} + \frac{\partial \mathbf{R_{B_RB_T}}}{\partial x}\mathbf{V_{R_{B_TI}F_g}} \tag{C.91}$$

where $\frac{\partial \mathbf{R_{B_RW_R}}}{\partial x}$ is formulated in Eq. (C.86).

$$\frac{\partial F_{B_R}}{\partial u_0} = -\mathbf{R_{B_RW_R}}\frac{\partial F_a}{\partial u_0} + \frac{\partial F_p}{\partial u_0} \tag{C.92}$$

The following formulates the partial derivatives of applied moment, given in Eq. (2.13).

$$M_{B_R} = M_a + M_p + \mathbf{S}_m\mathbf{R_{B_RB_T}}\mathbf{R_{B_TI}}G \tag{C.93}$$

where

$$M_a = \begin{bmatrix} \mathcal{L} \\ \mathcal{M} \\ \mathcal{N} \end{bmatrix} \tag{C.94}$$

$$M_p = \begin{bmatrix} M_{x_p} \\ M_{y_p} \\ M_{z_p} \end{bmatrix} \tag{C.95}$$

$$\mathbf{S_m} = \sum_{j=0}^{k} m_j \mathbf{S}(\rho_{m_j}) \tag{C.96}$$

$$G = \begin{bmatrix} 0 \\ 0 \\ g \end{bmatrix} \tag{C.97}$$

$$\frac{\partial M_{B_R}}{\partial x} = \frac{\partial M_a}{\partial x} - \mathbf{S}_m \frac{\partial}{\partial x}\left[\mathbf{R_{B_R B_T}} \mathbf{R_{B_T I}} G\right] \tag{C.98}$$

$$\frac{\partial}{\partial x}\left[\mathbf{R_{B_R B_T}} \mathbf{R_{B_T I}} G\right] = \frac{\partial \mathbf{R_{B_R B_T}}}{\partial x} \mathbf{V_{R_{B_T I} G}} + \mathbf{R_{B_R B_T}} \frac{\partial}{\partial x}\left(\mathbf{R_{B_T I}} G\right) \tag{C.99}$$

$$\frac{\partial}{\partial x}\left(\mathbf{R_{B_T I}} G\right) = \mathbf{0_{3\times 12}} \tag{C.100}$$

$$\frac{\partial M_{B_R}}{\partial x} = \frac{\partial M_a}{\partial x} - \mathbf{S}_m \frac{\partial \mathbf{R_{B_R B_T}}}{\partial x} \mathbf{V_{R_{B_T I} G}} \tag{C.101}$$

where $\frac{\partial \mathbf{R_{B_R B_T}}}{\partial x}$ is given in Eq. (C.51).

$$\frac{\partial M_{B_R}}{\partial u_0} = \frac{\partial M_a}{\partial u_0} + \frac{\partial M_p}{\partial u_0} \tag{C.102}$$

From Eq. (2.20), v is written as

$$v = \begin{bmatrix} F_{B_R} \\ M_{B_R} \end{bmatrix} \tag{C.103}$$

Matrices **E** and **F** in Eq. (2.55) are then written as

$$\mathbf{E} = \begin{bmatrix} \frac{\partial F_{B_R}}{\partial x} \\ \frac{\partial M_{B_R}}{\partial x} \end{bmatrix} \tag{C.104}$$

$$\mathbf{F} = \begin{bmatrix} \frac{\partial F_{B_R}}{\partial U_0} \\ \frac{\partial M_{B_R}}{\partial U_0} \end{bmatrix} \tag{C.105}$$

APPENDIX D

F-15 DATA

The values for the aerodynamic coefficients are given in Table D.8. The origin of the body frame is given in Table D.1. The nose of the aircraft is at fuselage station 116.3. The center of mass of the empty F15 is given in Table D.2. The moment arms of the fuel tanks are given in Tables D.3, D.4 and D.5, respectively. The thrust inclination angles are given in Table D.6. The thrust moment arms are given in Table D.7. The fuel burn rate is given in Eq. (D.1). Additional geometric parameters are given in Table D.9

$$\dot{m}_{fuel} = (2.21 \times 10^{-5} T + 0.0558) kg/s \tag{D.1}$$

where T is the thrust of a single engine. The inertia matrices for the full F-15C and F-15E with respect to the full aircraft center of mass are given as

$$\underline{\underline{\mathbf{I}}}^{\mathbf{C}}_{\mathbf{CM,FULL}} = \begin{bmatrix} 88886 & 0 & -470 \\ 0 & 256511 & 0 \\ -470 & 0 & 327165 \end{bmatrix} kgm^2$$

$$\underline{\underline{\mathbf{I}}}^{\mathbf{E}}_{\mathbf{CM,FULL}} = \begin{bmatrix} 114519 & 0 & -3171 \\ 0 & 314283 & 0 \\ -3171 & 0 & 407049 \end{bmatrix} kgm^2$$

Table D.1. Body Frame Origin

Fuselage Station	555.9
Waterline	128.1
Butt-line	0

Table D.2. Rigid Aircraft Center of Mass

Fuselage Station	554.6
Waterline	118.5
Butt-line	0

Table D.3. Wing Tank Moment Arm

X	3.9 in
Y	± 115.25 in
Z	40.4 in

Table D.4. Fuselage Tank Moment Arm

X	16.1 in
Y	0.0 in
Z	67.5 in

Table D.5. Conformal Tank Moment Arm

X	-19.6 in
Y	± 75.0 in
Z	27.6 in

Table D.6. Engine Inclination Angle

$\delta_{T_{yi}}$	0.0 deg
$\delta_{T_{zi}}$	0.8 deg

Table D.7. Engine Moment Arm

l_{xi}	-266.4 in
l_{yi}	±25.3 in
l_{zi}	2.3 in

Table D.8. F-15 Aerodynamic Coefficients

C_{L0}	0.05
$C_{L\alpha}$	3.84
$C_{L\delta_h}$	0.05
C_{Lq}	6.2
C_{D0}	0.0218
$C_{D\alpha^2}$	1.696
$C_{D\beta^2}$	0
$C_{D,Stores}$	0.0054
$C_{D\delta^2_{dh}}$	0.01215
$C_{D\delta_{dh}}$	0.00465
$C_{D\delta^2_a}$	0.0115
$C_{D\delta_a}$	0.0186
$C_{D\delta^2_r}$	0.049
$C_{D\delta_r}$	0
$C_{Y\beta}$	-0.86
$C_{Y\delta_r}$	0.229
$C_{Y\delta_{dh}}$	-0.057
$C_{l\beta}$	-0.092
$C_{l\delta_r}$	0.006
$C_{l\delta_{dh}}$	0.043
$C_{l\delta_a}$	0.03
C_{lp}	-0.275
C_{lq}	0.1
C_{m0}	0
$C_{m\alpha}$	-0.344
$C_{m\delta_{dh}}$	-0.573
C_{mq}	-4.25
$C_{n\beta}$	0.143
$C_{n\delta_r}$	-0.092
$C_{n\delta_{dh}}$	0.029
$C_{n\delta_a}$	0.001
C_{np}	0
C_{nr}	-0.4

Table D.9. Addition Geometric Parameters

$\mathcal{S}$	$56.6m^2$
b	$13.0m$
c	$4.86m$

APPENDIX E

STATIC SWEET SPOT PLOTS

E.1 F-15C

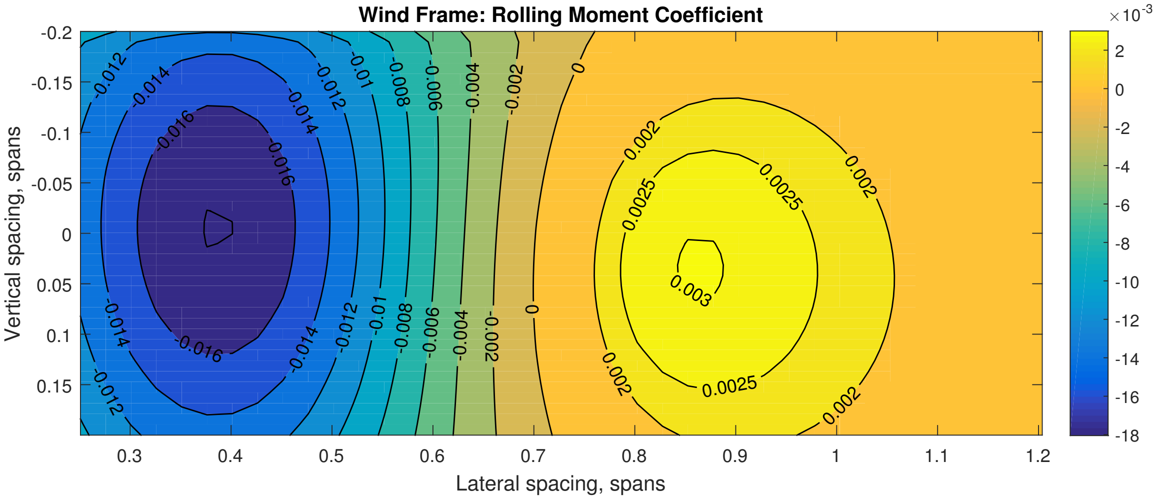

Figure E.1. Rolling Moment Simulation Results for the Empty F-15C Heavy Tanker Case.

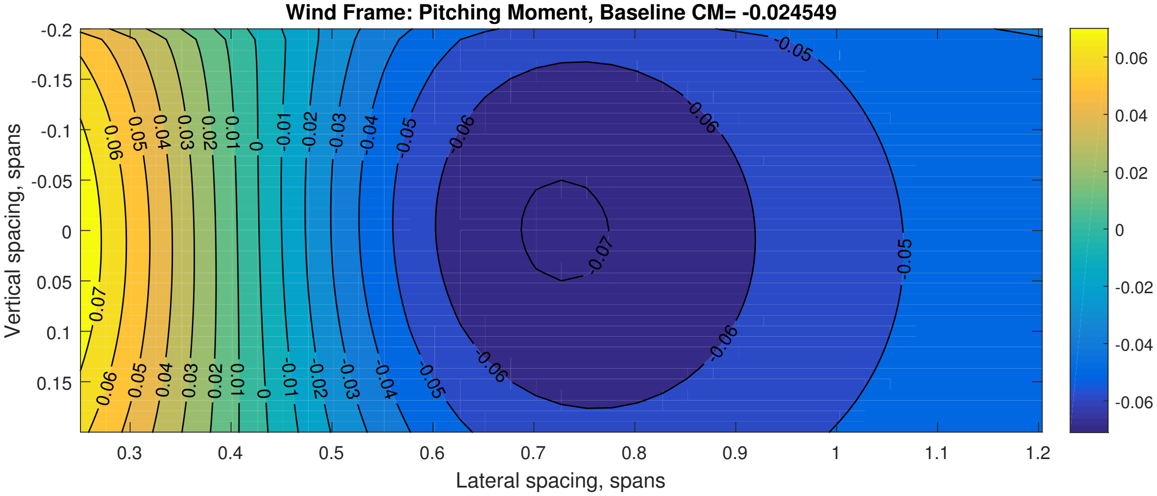

Figure E.2. Pitching Moment Simulation Results for the Empty F-15C Heavy Tanker Case.

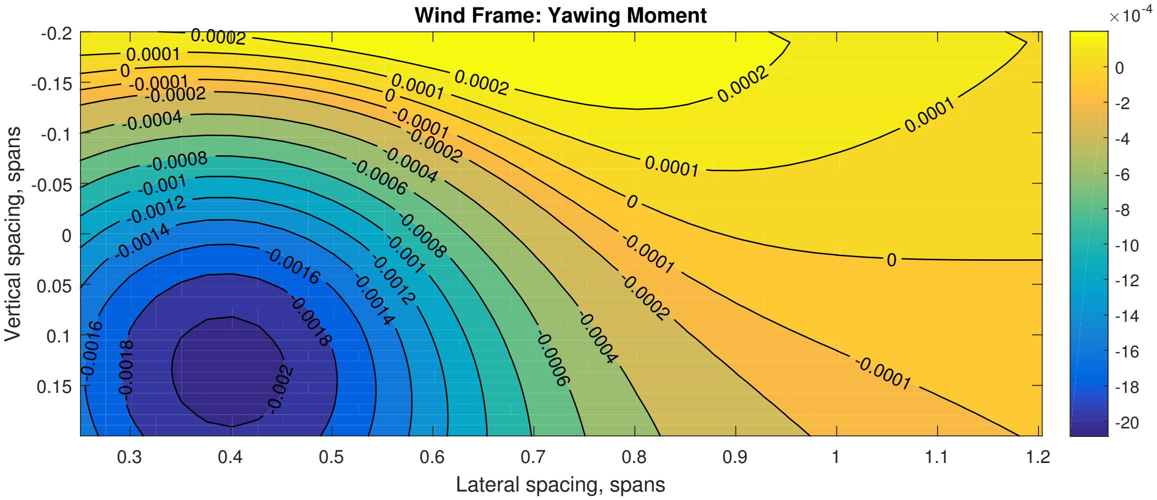

Figure E.3. Yawing Moment Simulation Results for the Empty F-15C Heavy Tanker Case.

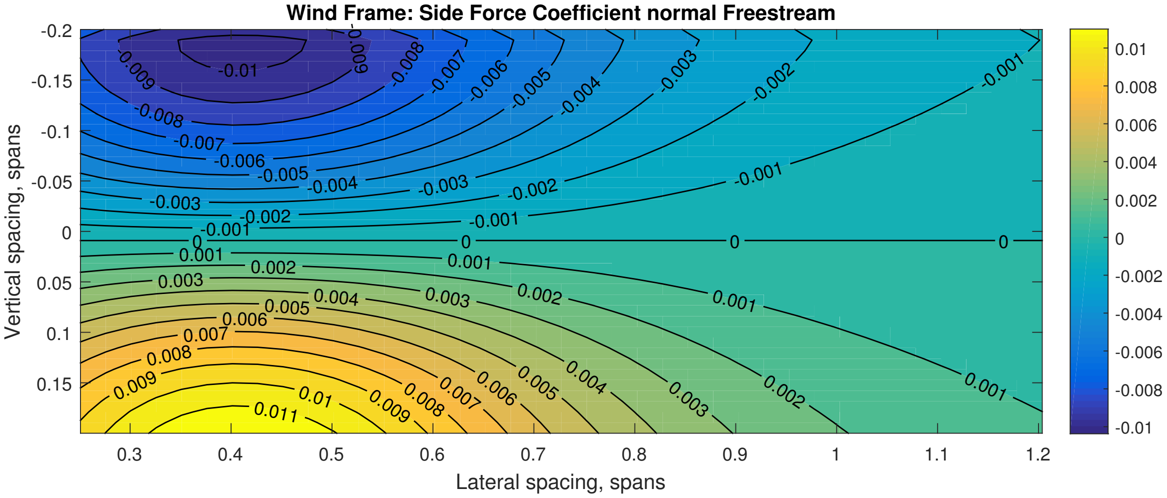

Figure E.4. Side Force Simulation Results for the Empty F-15C Heavy Tanker Case.

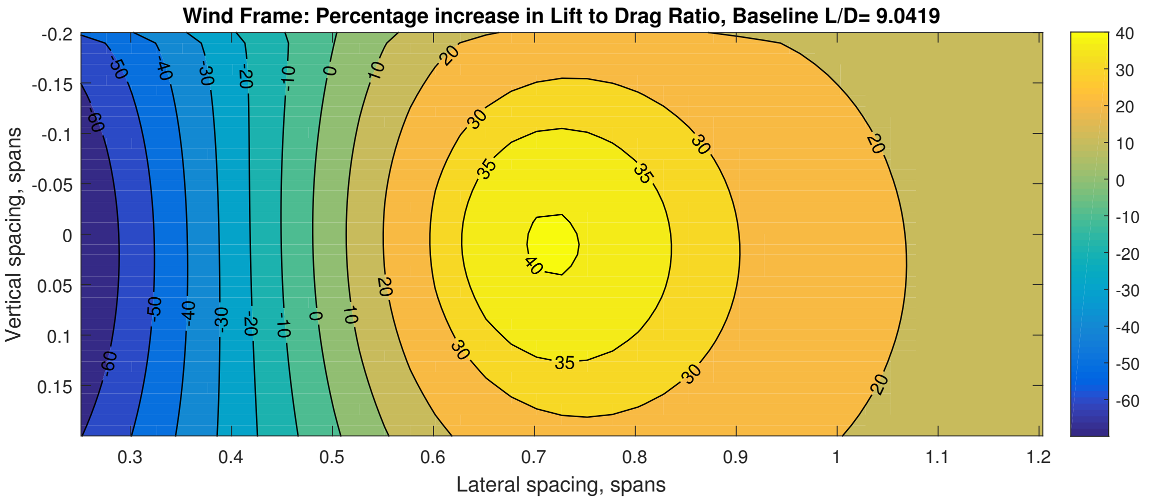

Figure E.5. Lift-to-Drag Ratio Simulation Results for the Empty F-15C Heavy Tanker Case.

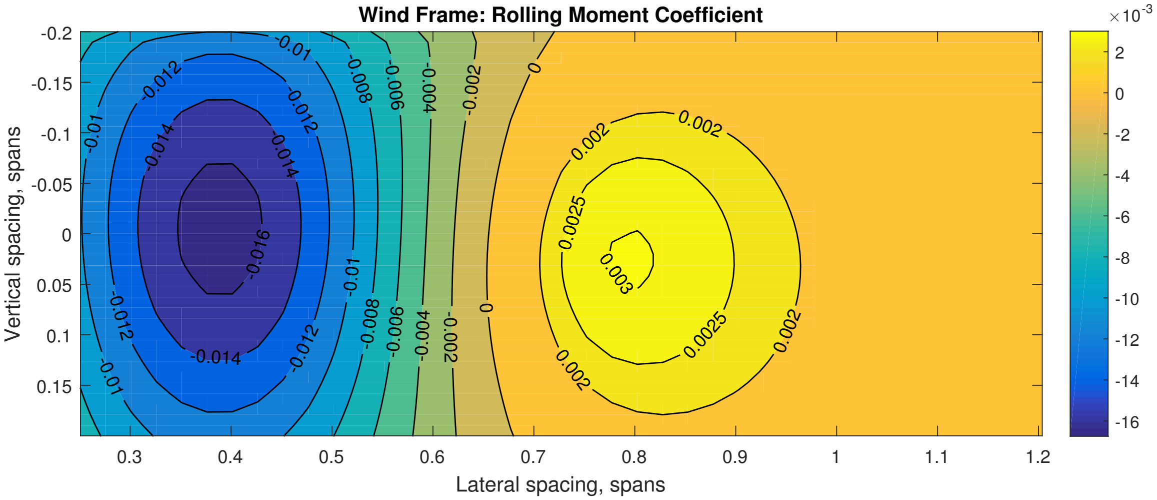

Figure E.6. Rolling Moment Simulation Results for the Full F-15C Light Tanker Case.

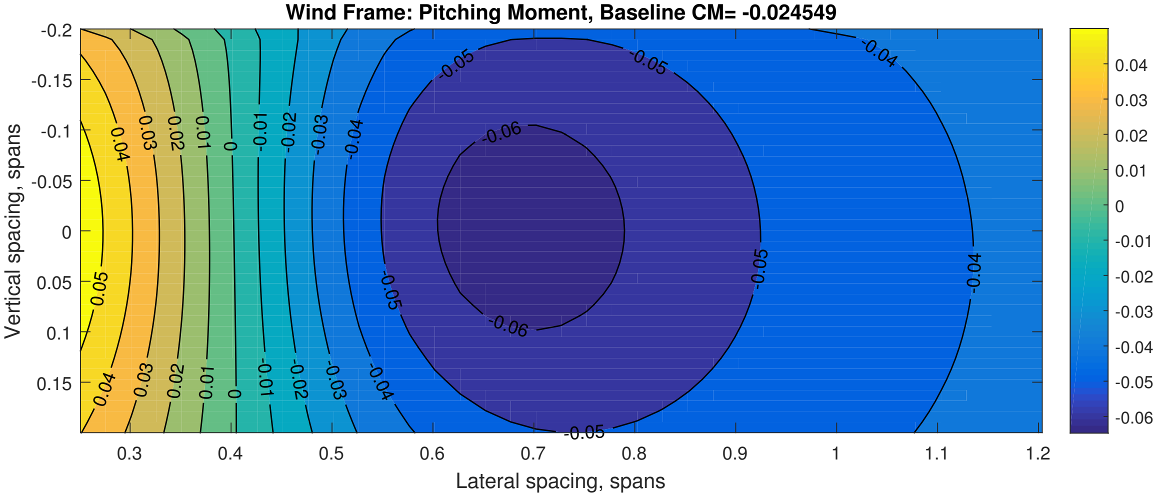

Figure E.7. Pitching Moment Simulation Results for the Full F-15C Light Tanker Case.

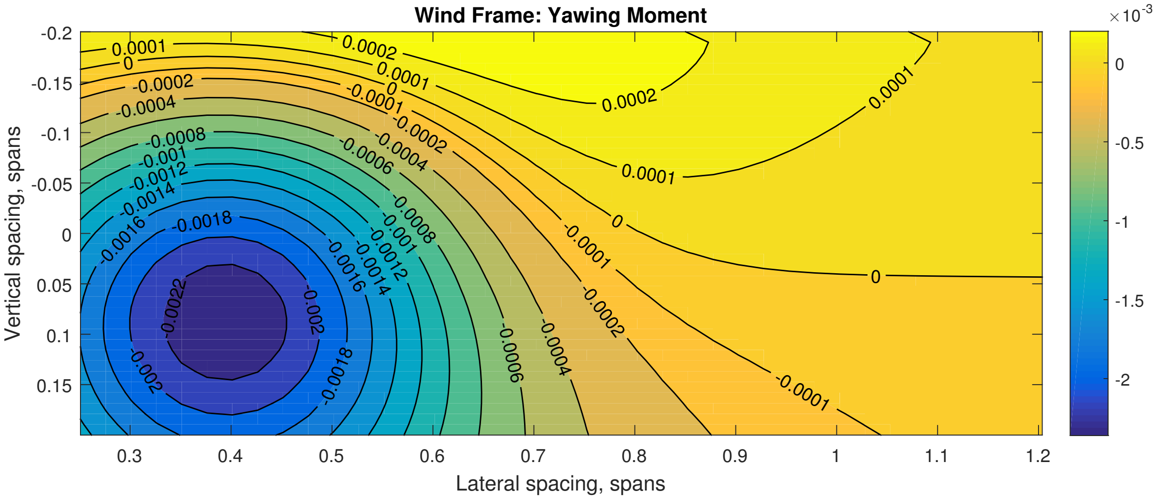

Figure E.8. Yawing Moment Simulation Results for the Full F-15C Light Tanker Case.

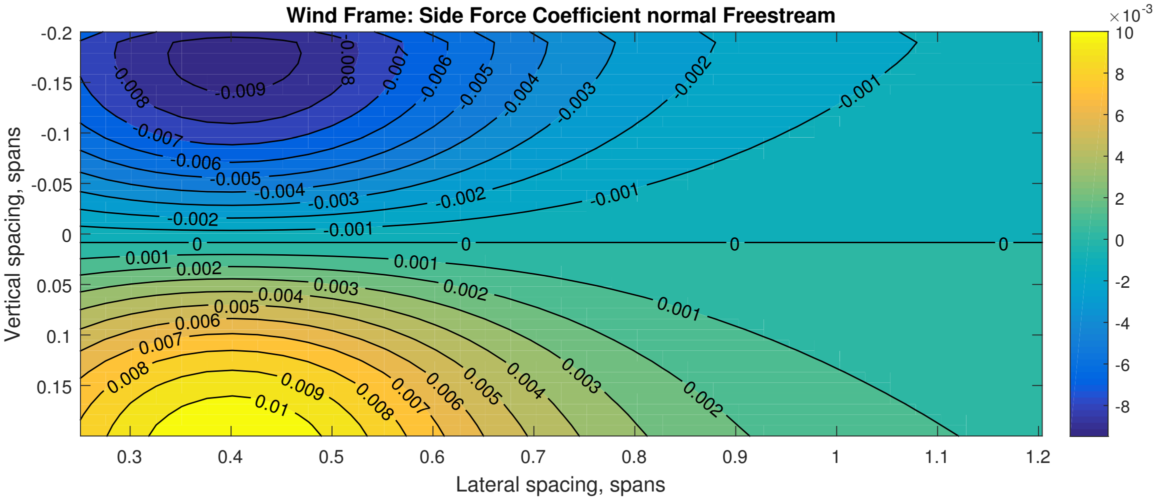

Figure E.9. Side Force Simulation Results for the Full F-15C Light Tanker Case.

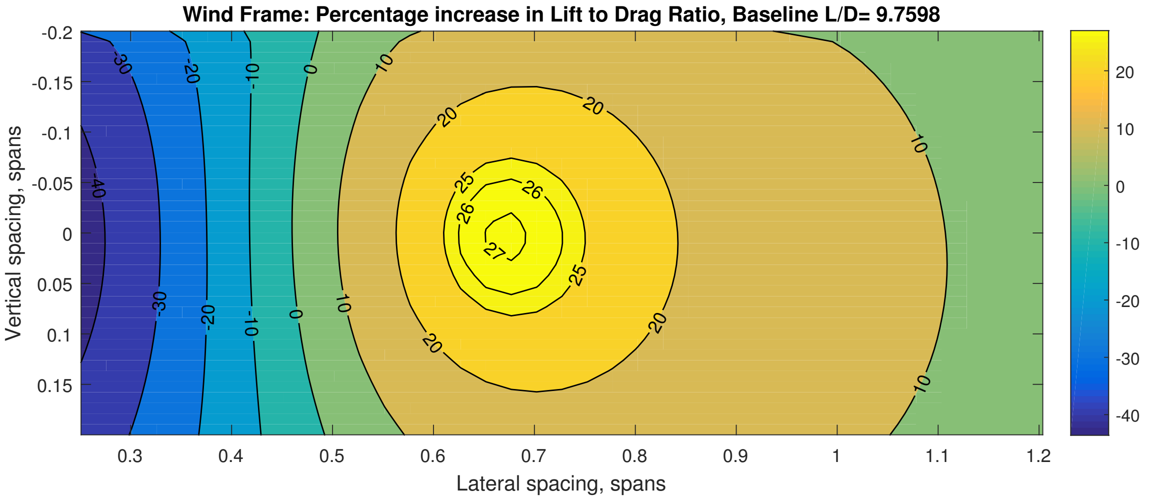

Figure E.10. Lift-to-Drag Ratio Simulation Results for the Full F-15C Light Tanker Case.

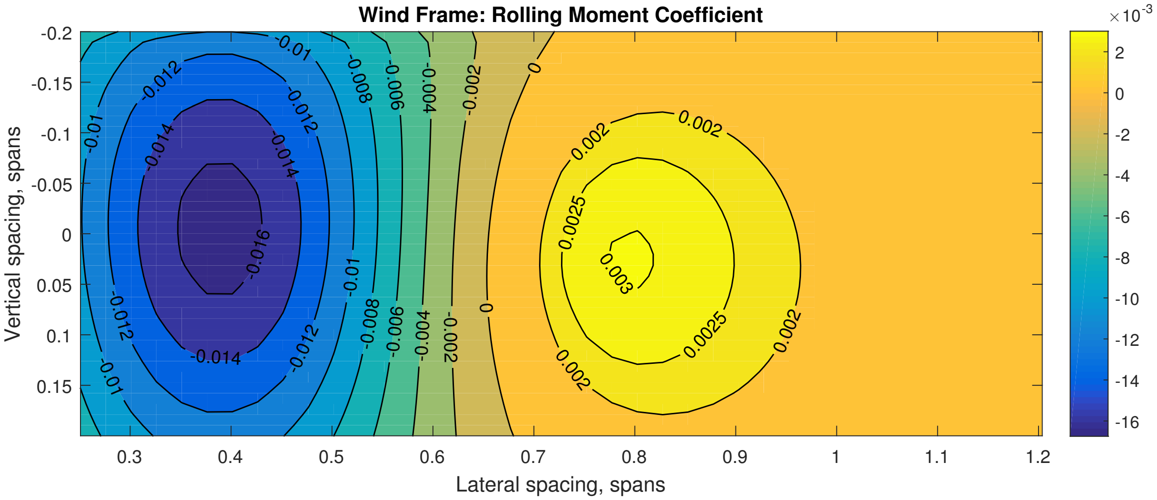

Figure E.11. Rolling Moment Simulation Results for the Empty F-15C Light Tanker Case.

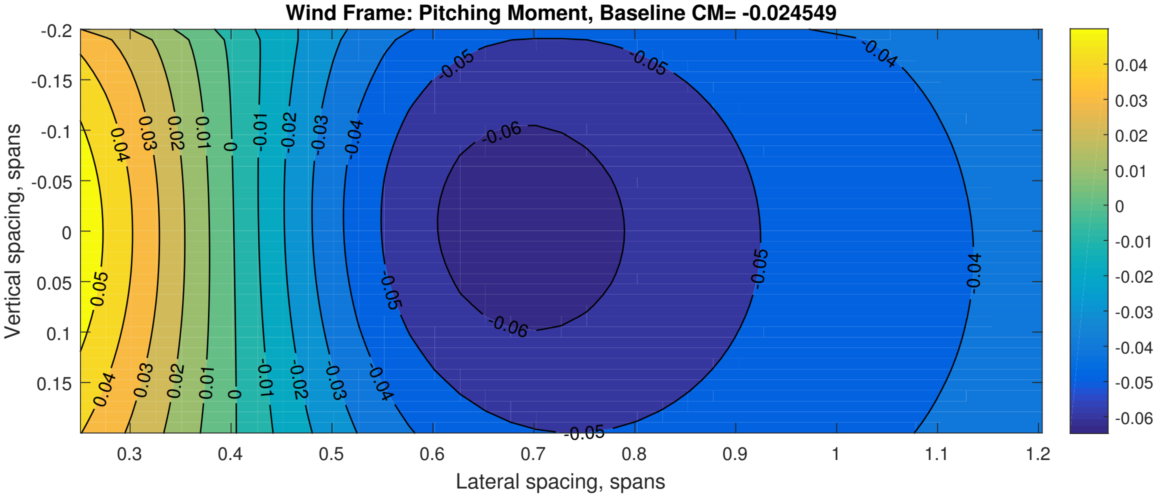

Figure E.12. Pitching Moment Simulation Results for the Empty F-15C Light Tanker Case.

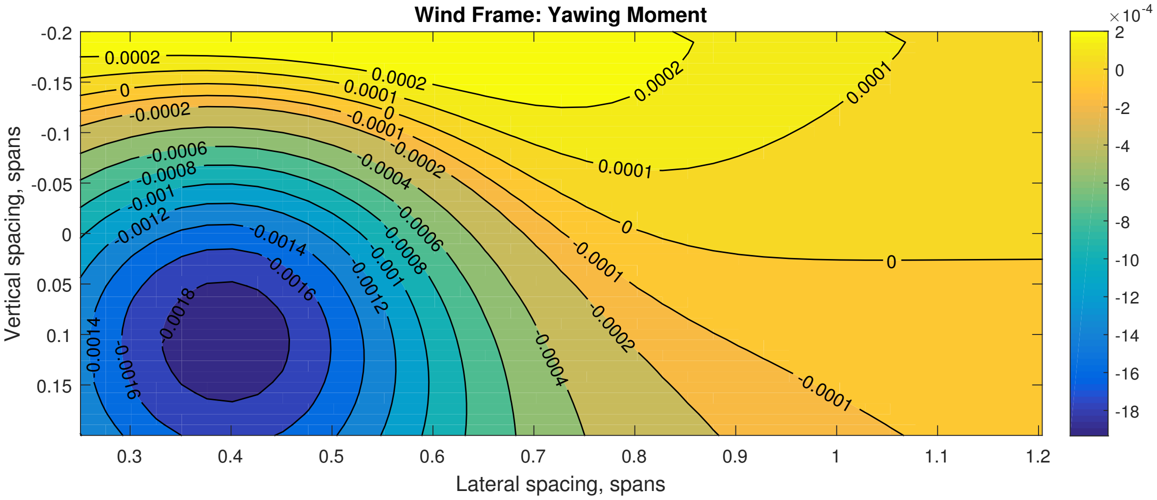

Figure E.13. Yawing Moment Simulation Results for the Empty F-15C Light Tanker Case.

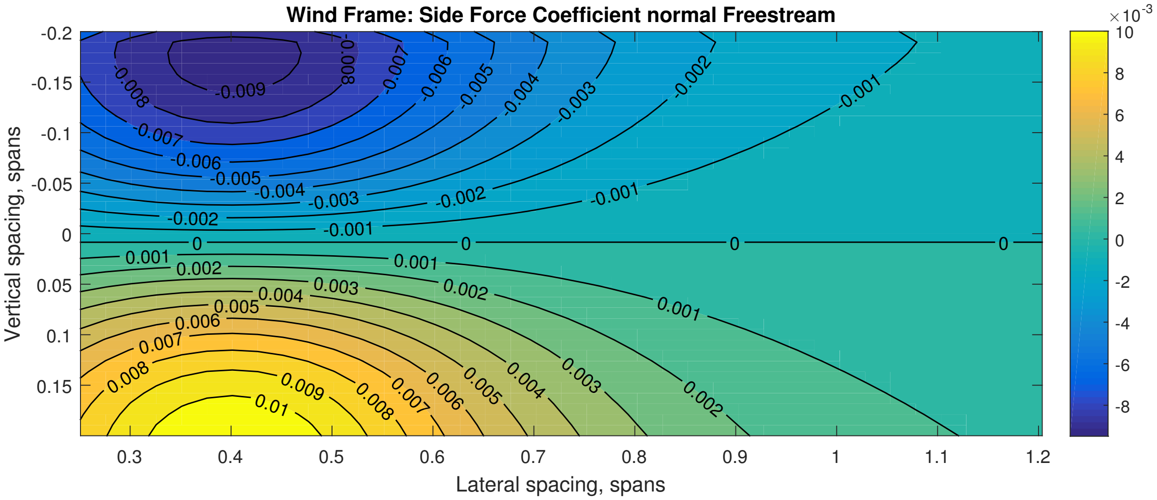

Figure E.14. Side Force Simulation Results for the Empty F-15C Light Tanker Case.

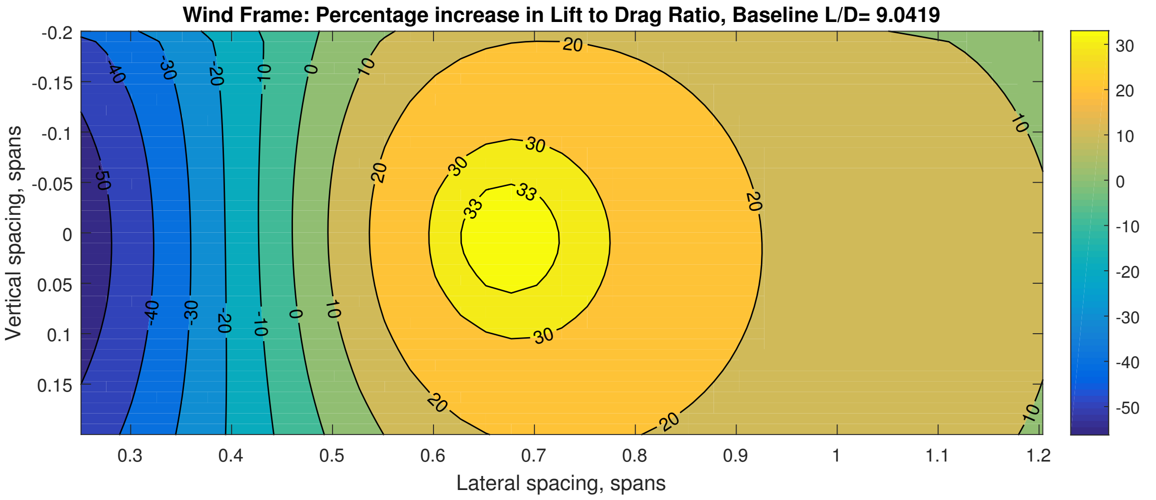

Figure E.15. Lift-to-Drag Ratio Simulation Results for the Empty F-15C Light Tanker Case.

E.1.1 F-15E

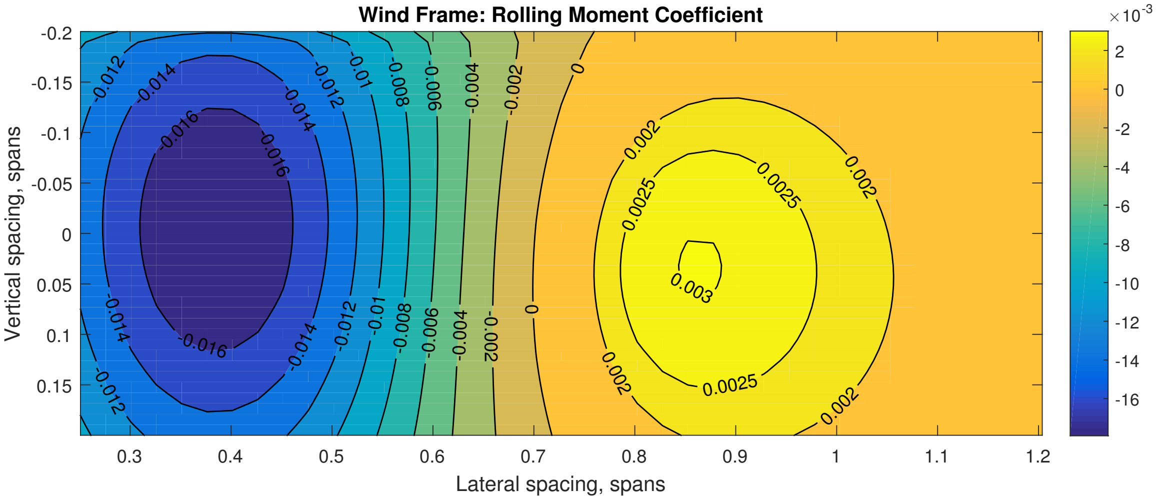

Figure E.16. Rolling Moment Simulation Results for the Empty F-15E Heavy Tanker Case.

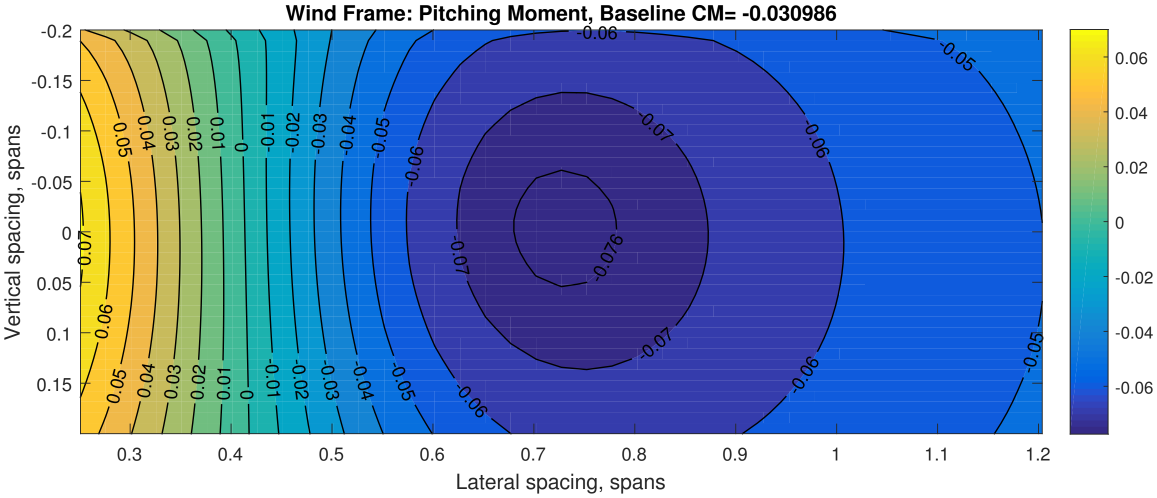

Figure E.17. Pitching Moment Simulation Results for the Empty F-15E Heavy Tanker Case.

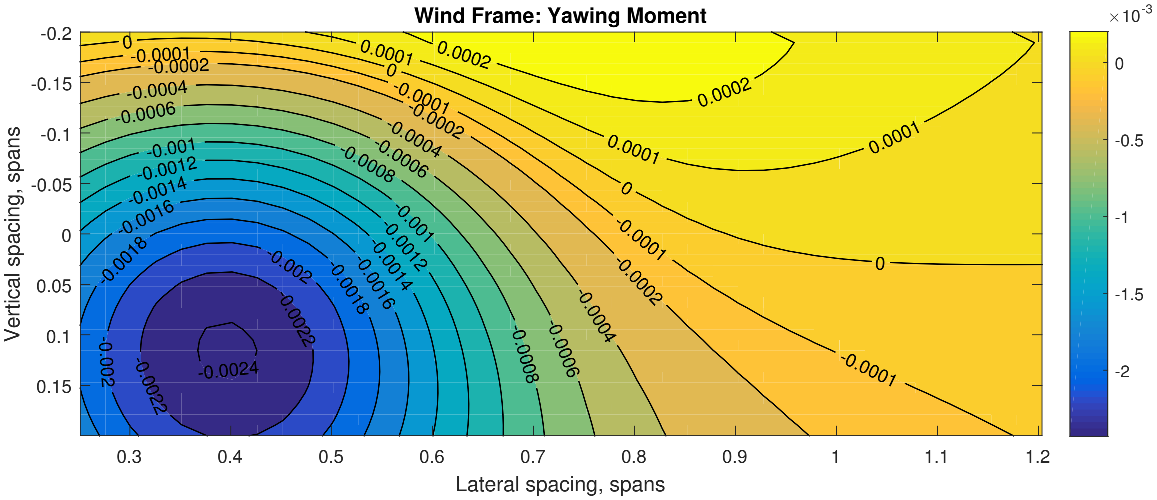

Figure E.18. Yawing Moment Simulation Results for the Empty F-15E Heavy Tanker Case.

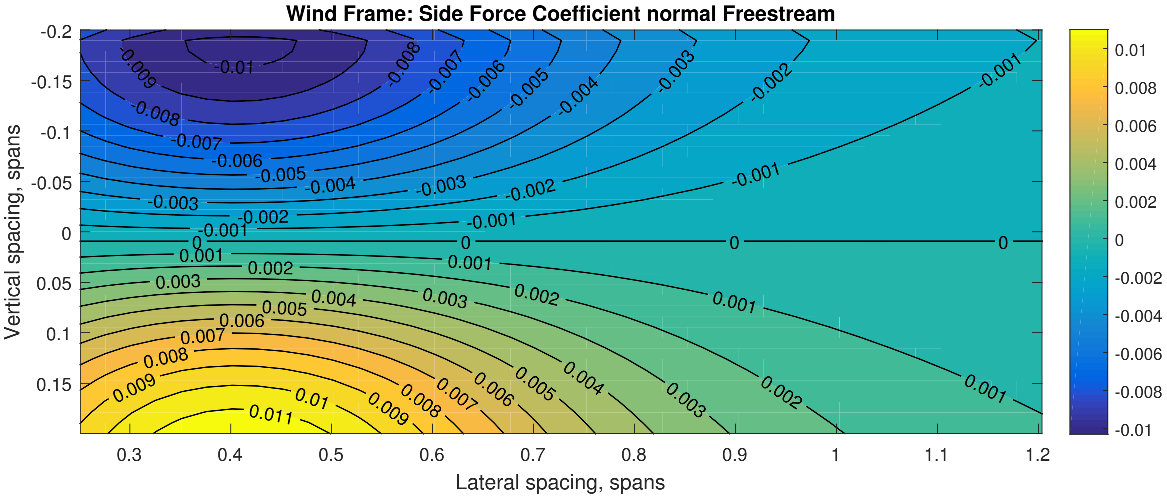

Figure E.19. Side Force Simulation Results for the Empty F-15E Heavy Tanker Case.

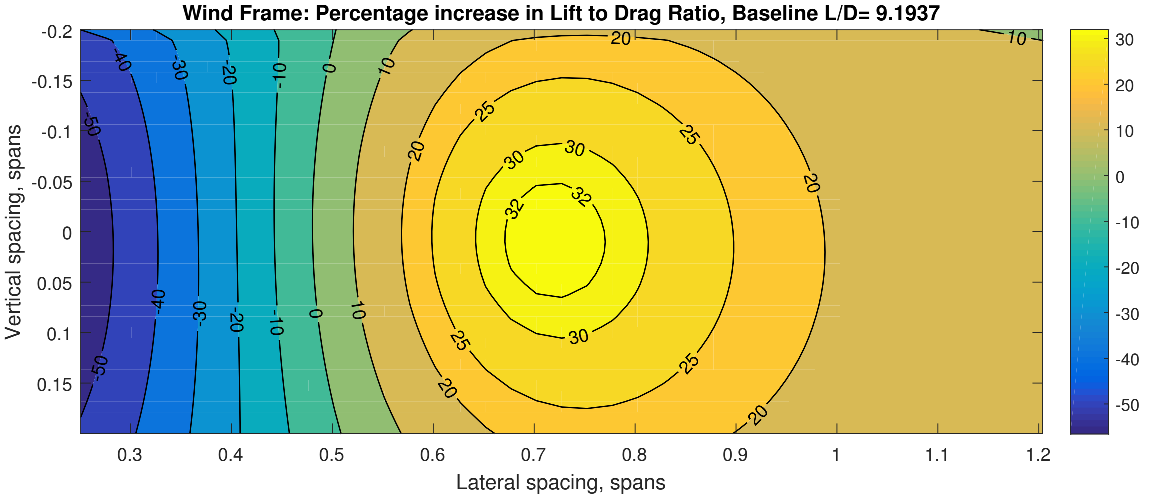

Figure E.20. Lift-to-Drag Ratio Simulation Results for the Empty F-15E Heavy Tanker Case.

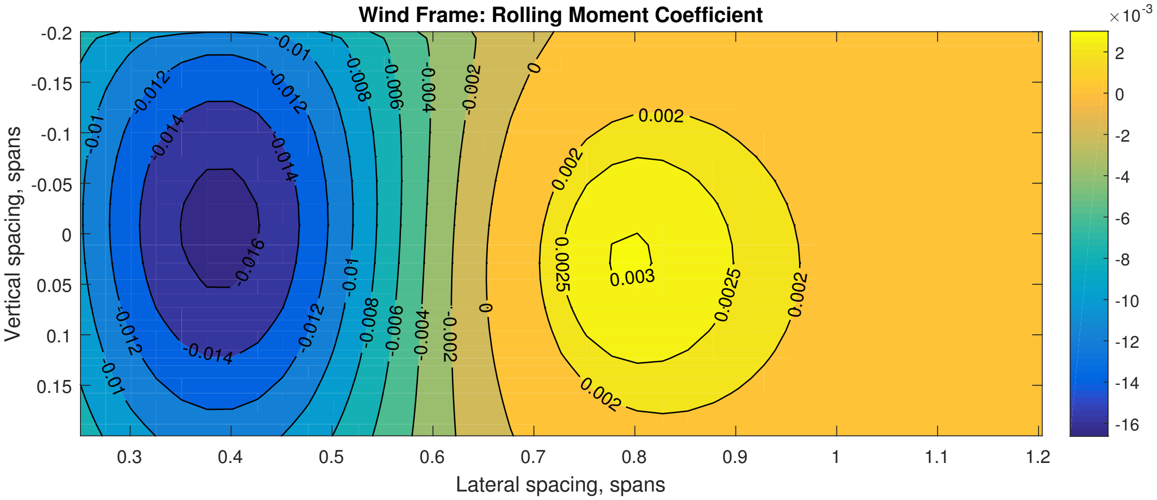

Figure E.21. Rolling Moment Simulation Results for the Full F-15E Light Tanker Case.

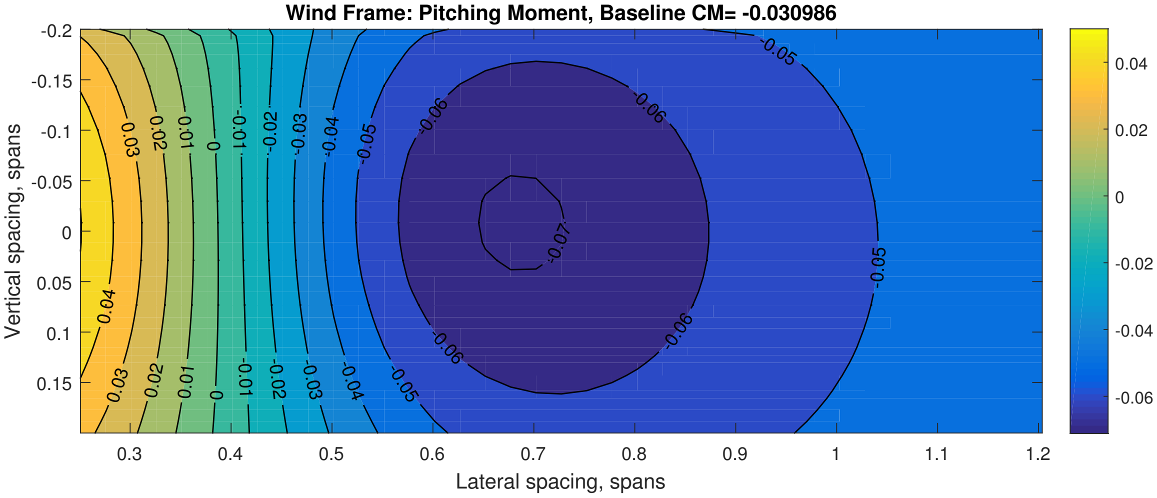

Figure E.22. Pitching Moment Simulation Results for the Full F-15E Light Tanker Case.

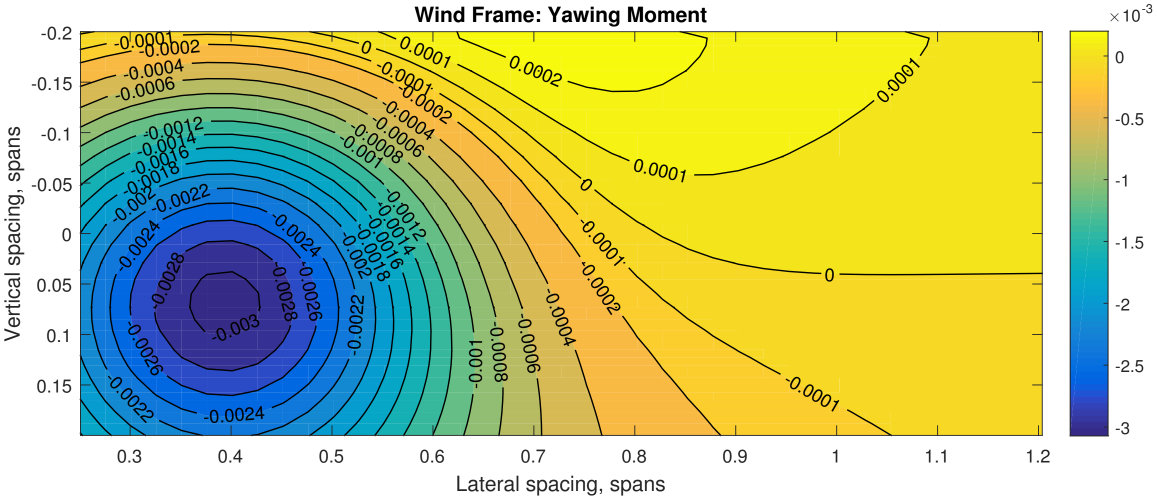

Figure E.23. Yawing Moment Simulation Results for the Full F-15E Light Tanker Case.

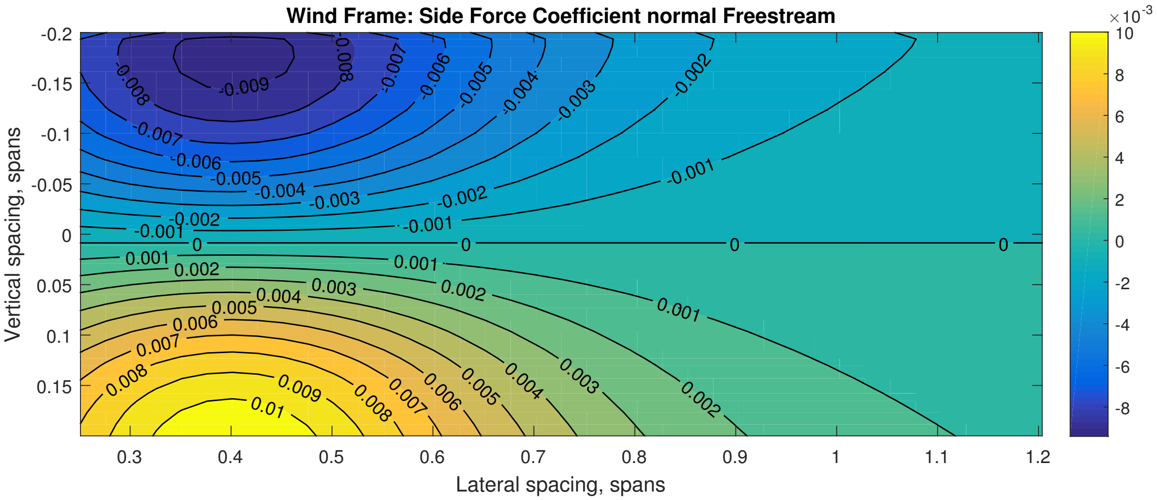

Figure E.24. Side Force Simulation Results for the Full F-15E Light Tanker Case.

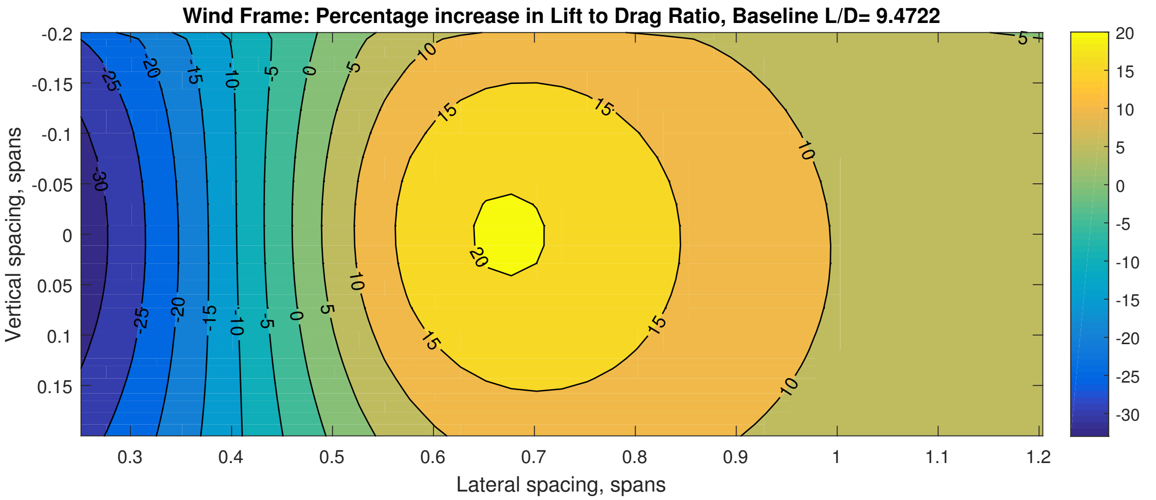

Figure E.25. Lift-to-Drag Ratio Simulation Results for the Full F-15E Light Tanker Case.

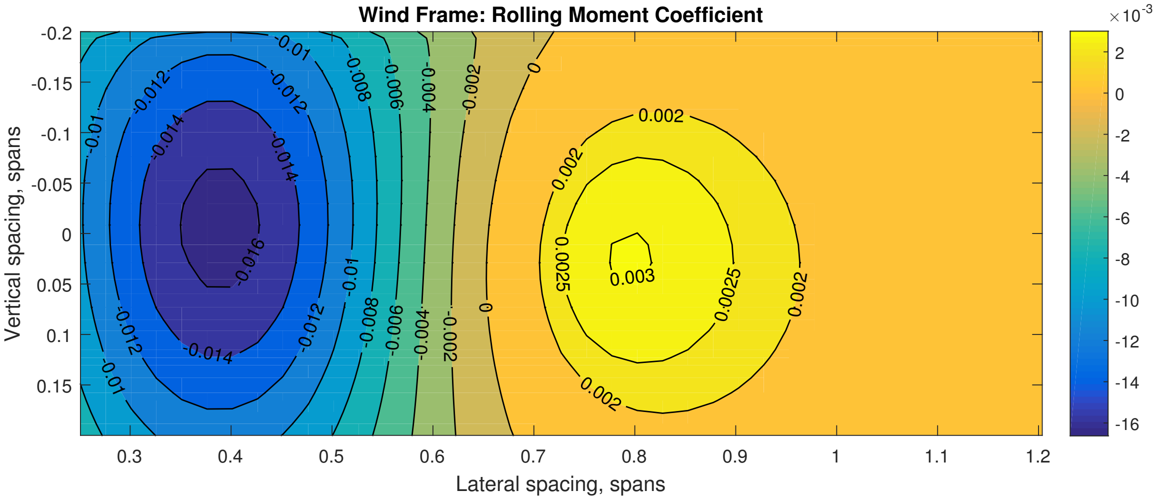

Figure E.26. Rolling Moment Simulation Results for the Empty F-15E Light Tanker Case.

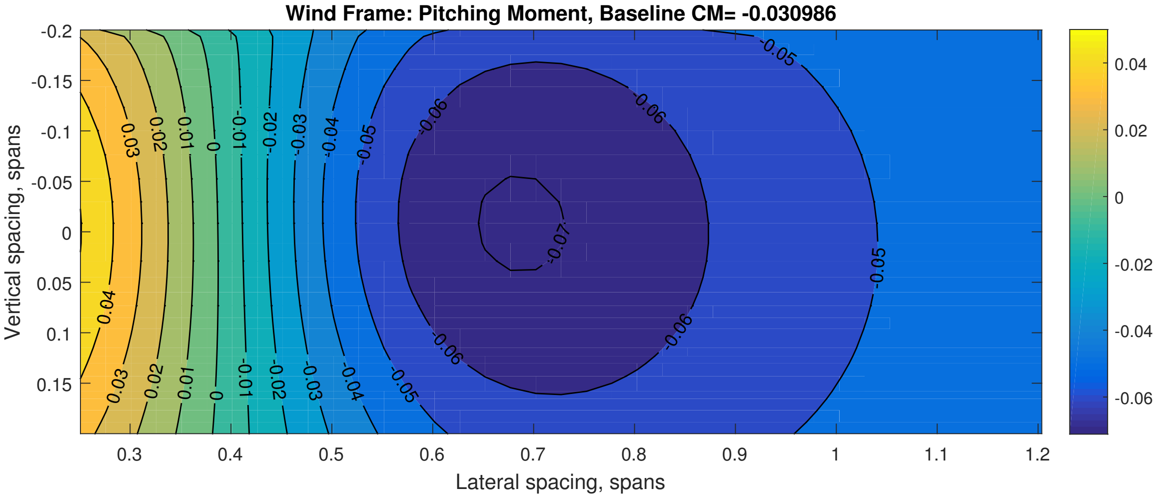

Figure E.27. Pitching Moment Simulation Results for the Empty F-15E Light Tanker Case.

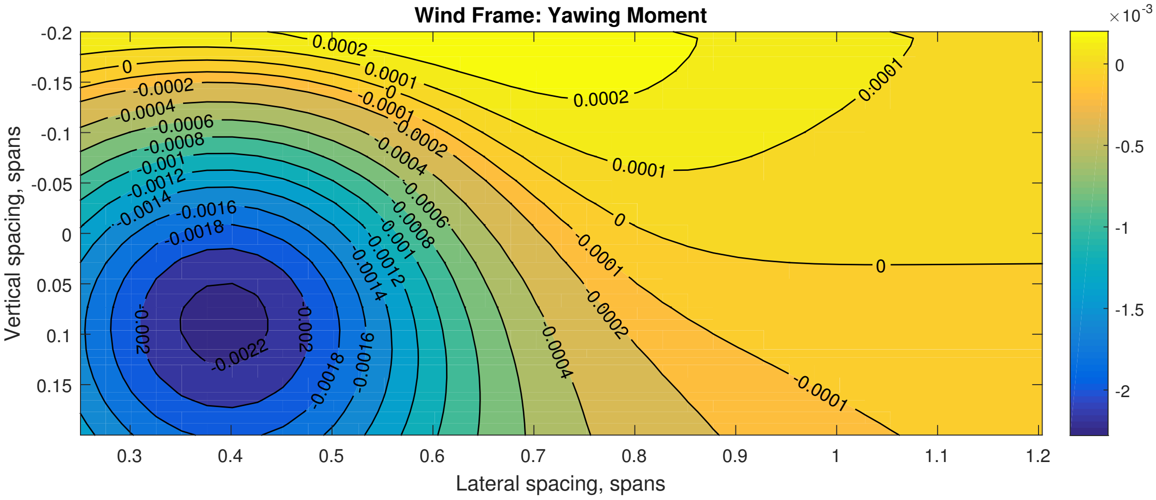

Figure E.28. Yawing Moment Simulation Results for the Empty F-15E Light Tanker Case.

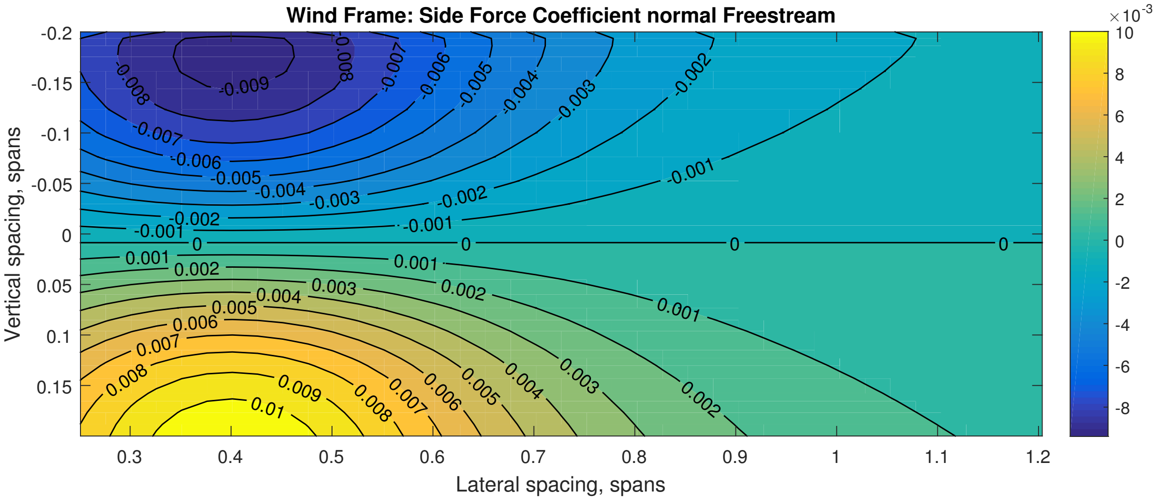

Figure E.29. Side Force Simulation Results for the Empty F-15E Light Tanker Case.

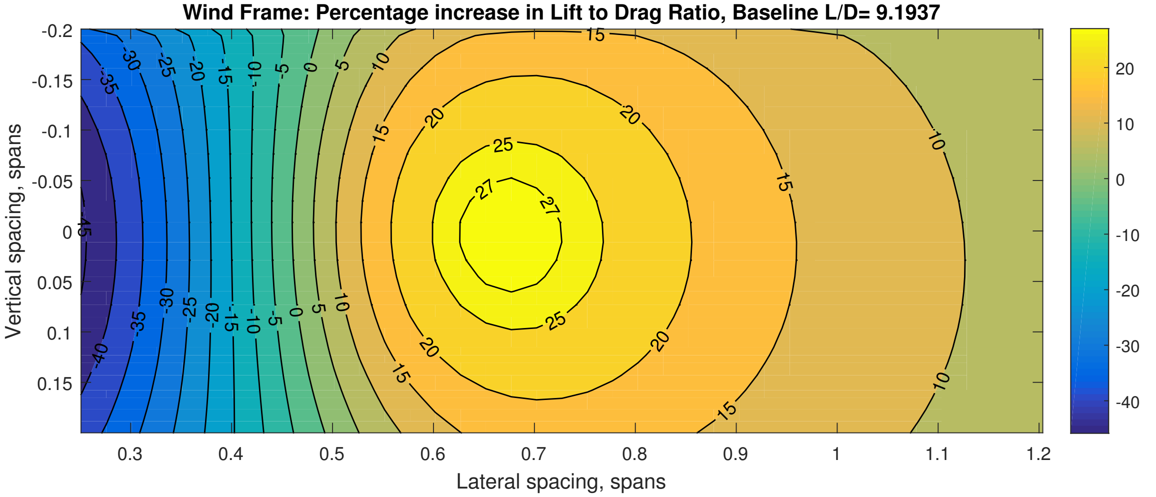

Figure E.30. Lift-to-Drag Ratio Simulation Results for the Empty F-15E Light Tanker Case.

E.2 Dynamic Sweet Spot Plots

E.2.1 F-15C

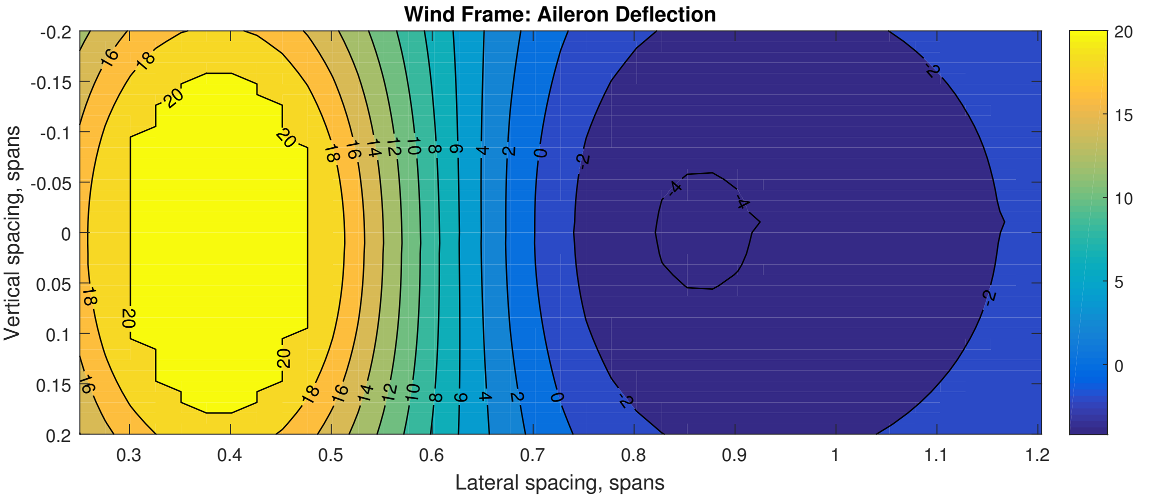

Figure E.31. Aileron Deflection Simulation Results for the Empty F-15C Heavy Tanker Case.

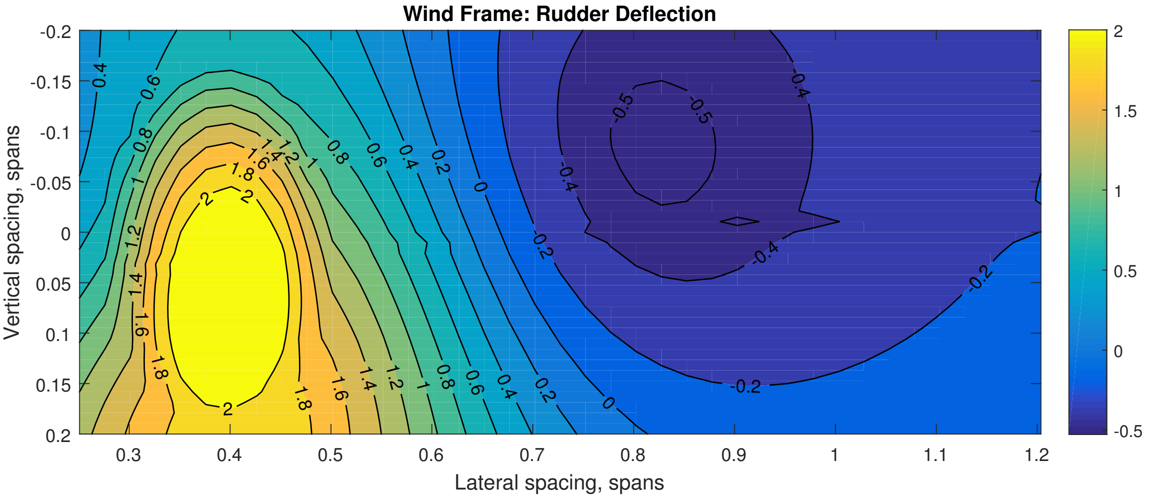

Figure E.32. Rudder Deflection Simulation Results for the Empty F-15C Heavy Tanker Case.

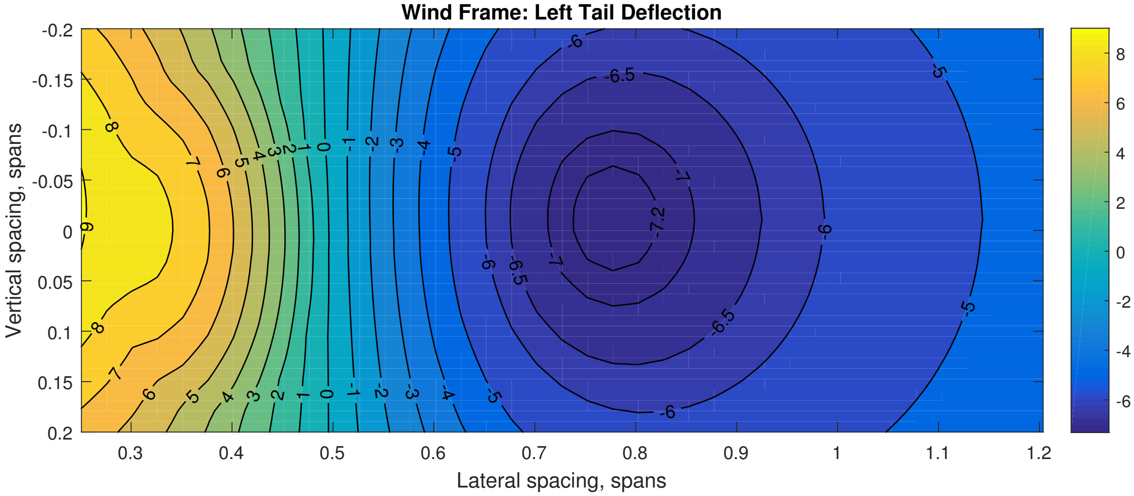

Figure E.33. Left Tail Deflection Simulation Results for the Empty F-15C Heavy Tanker Case.

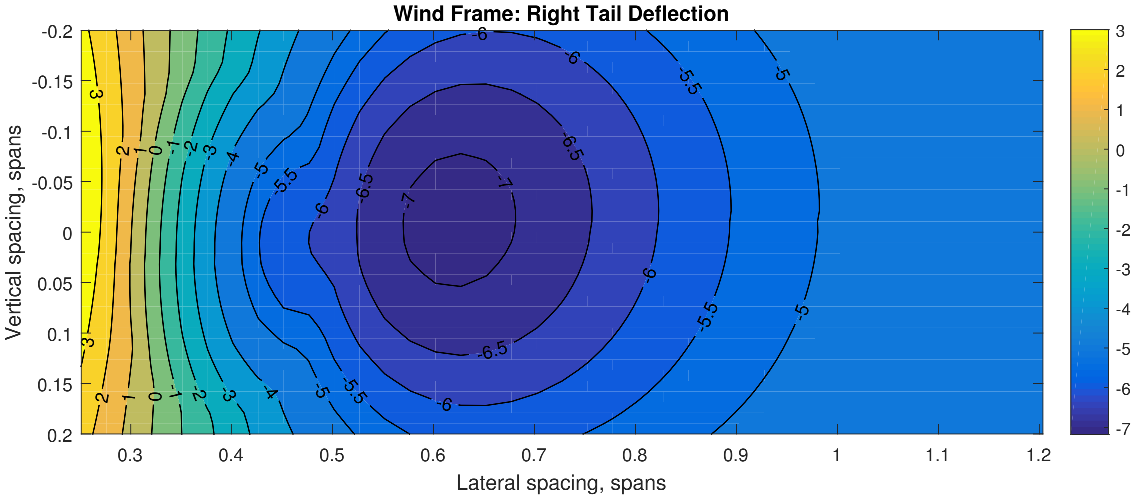

Figure E.34. Right Tail Deflection Simulation Results for the Empty F-15C Heavy Tanker Case.

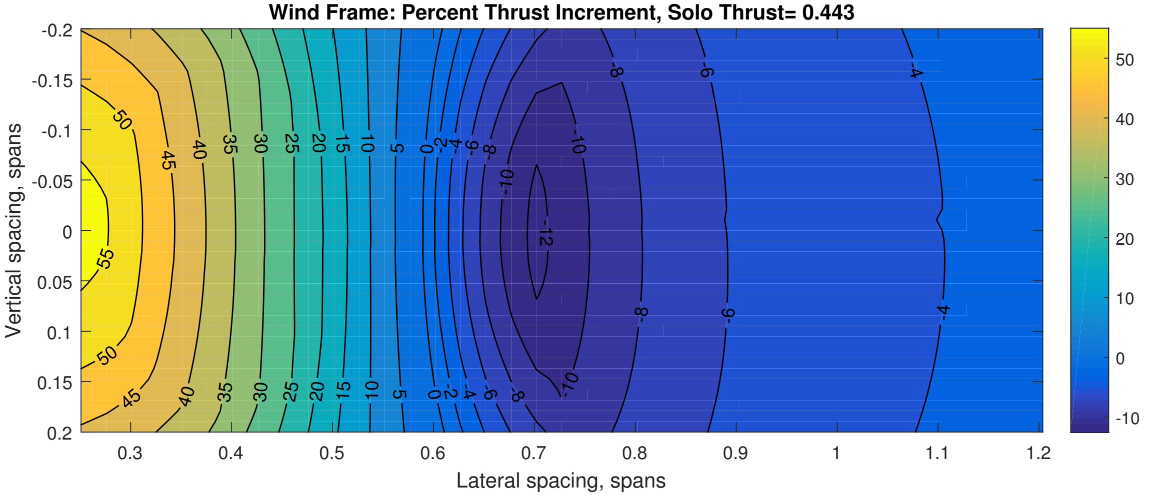

Figure E.35. Thrust Increment Simulation Results for the Empty F-15C Heavy Tanker Case.

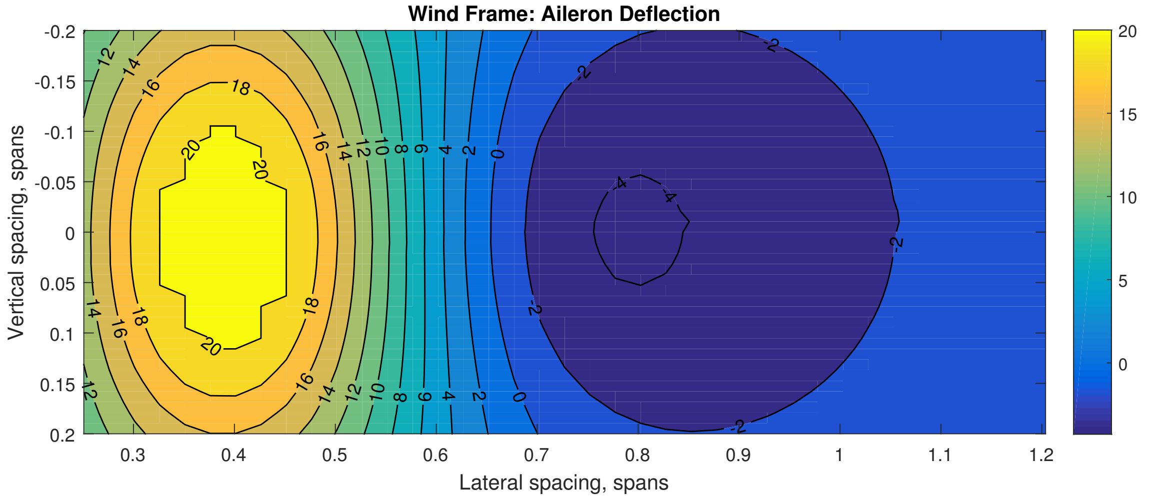

Figure E.36. Aileron Deflection Simulation Results for the Full F-15C Light Tanker Case.

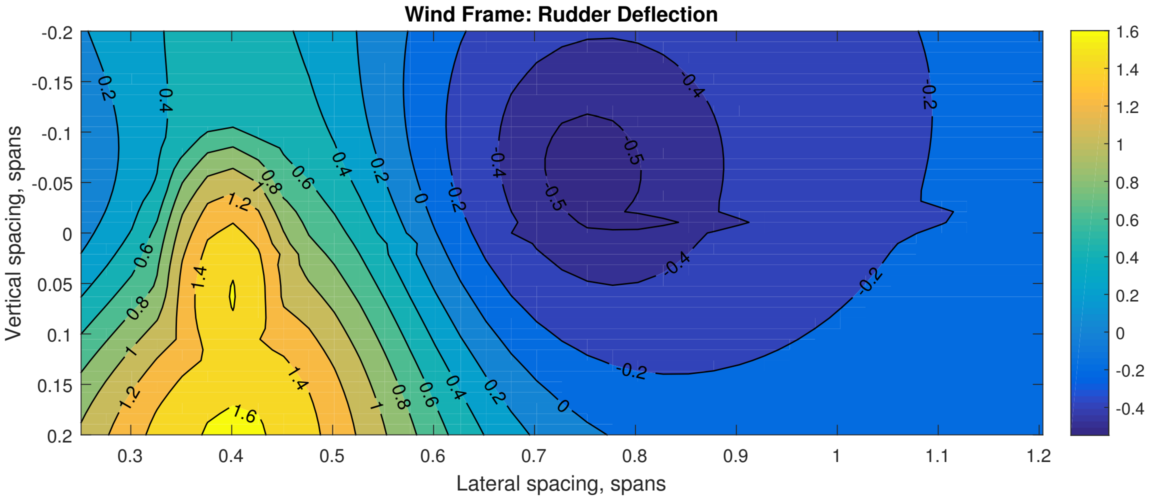

Figure E.37. Rudder Deflection Simulation Results for the Full F-15C Light Tanker Case.

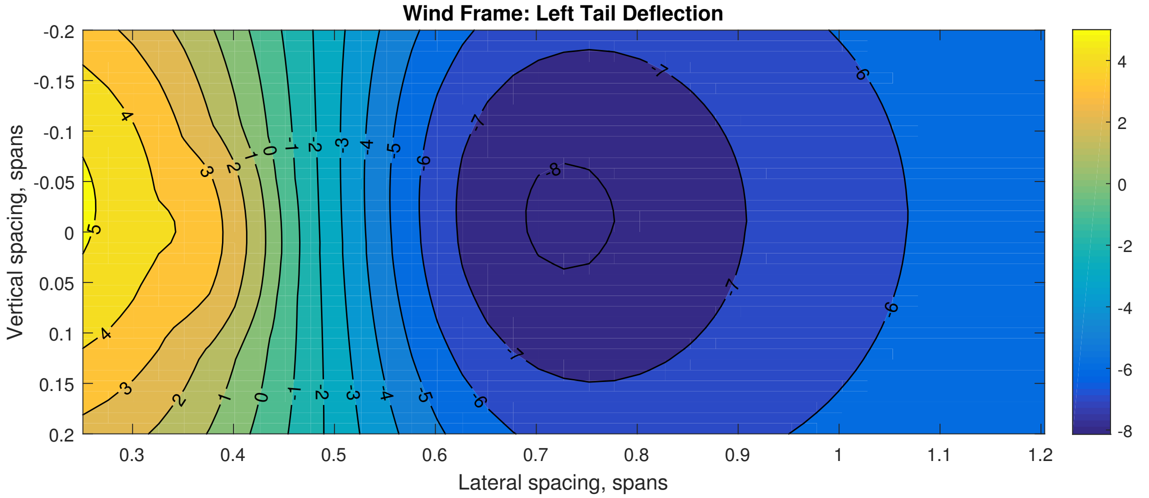

Figure E.38. Left Tail Deflection Simulation Results for the Full F-15C Light Tanker Case.

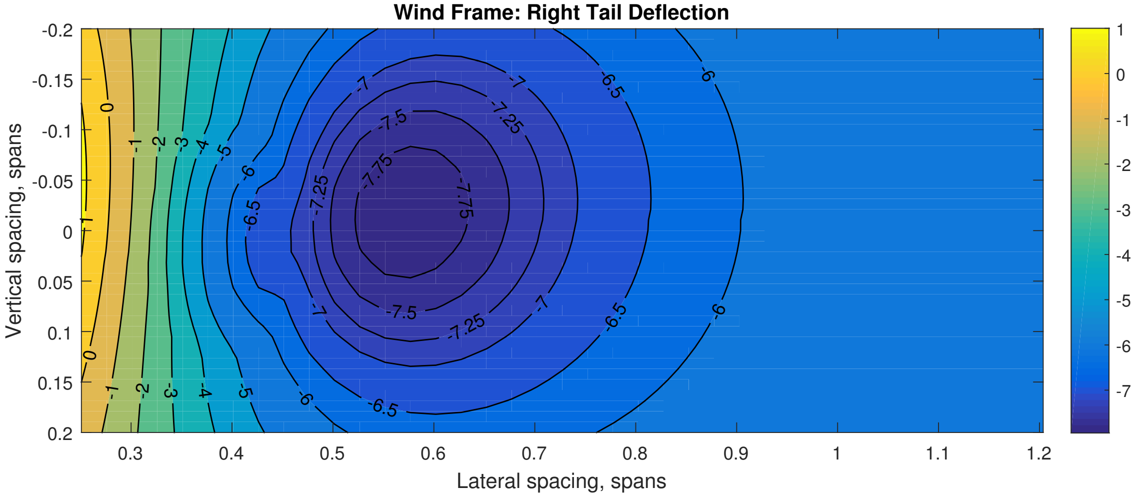

Figure E.39. Right Tail Deflection Simulation Results for the Full F-15C Light Tanker Case.

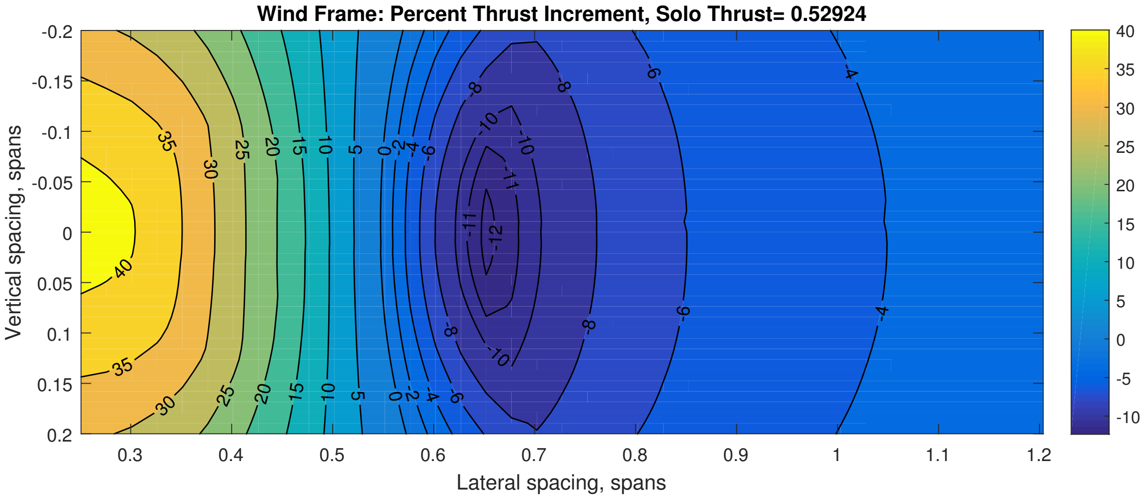

Figure E.40. Thrust Increment Simulation Results for the Full F-15C Light Tanker Case.

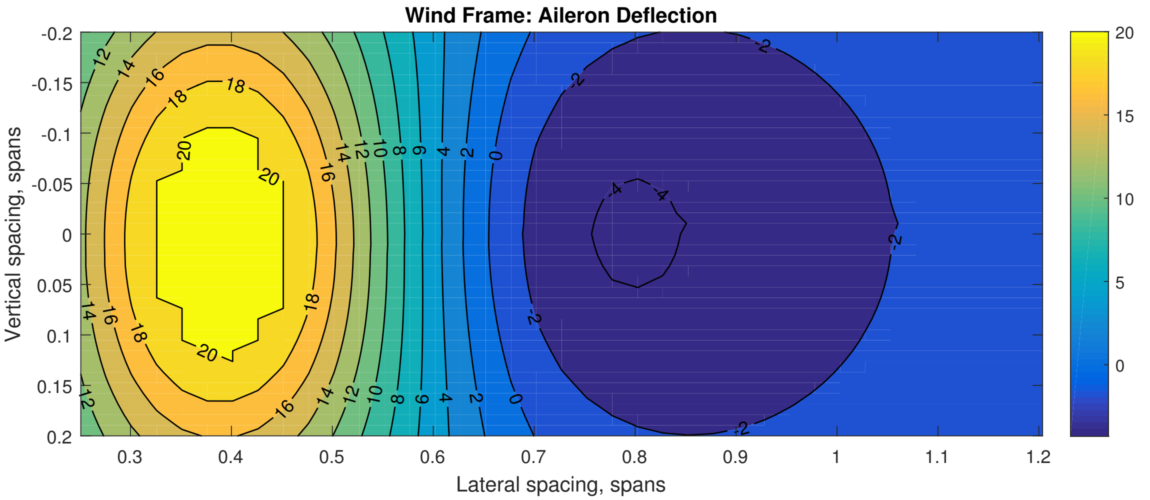

Figure E.41. Aileron Deflection Simulation Results for the Empty F-15C Light Tanker Case.

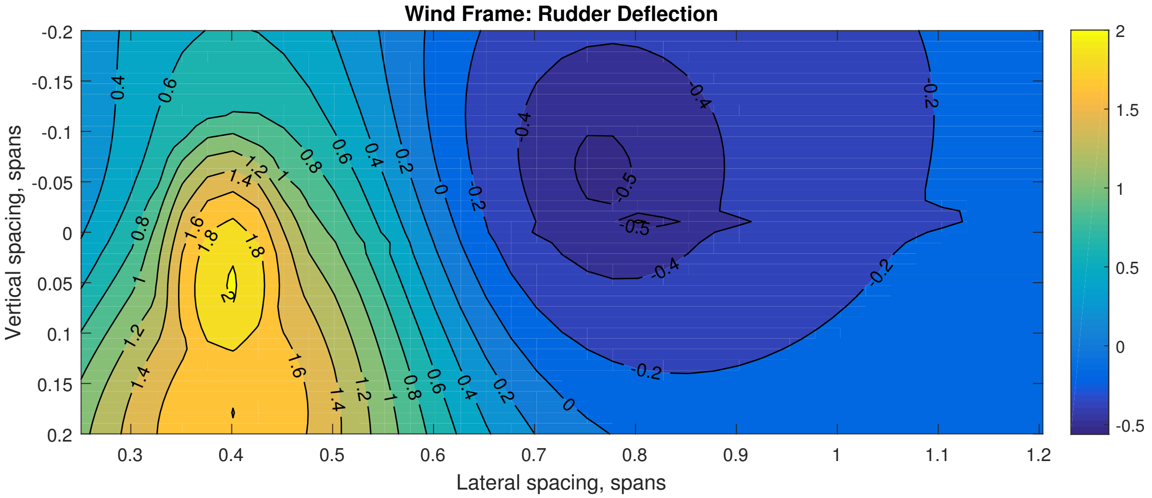

Figure E.42. Rudder Deflection Simulation Results for the Empty F-15C Light Tanker Case.

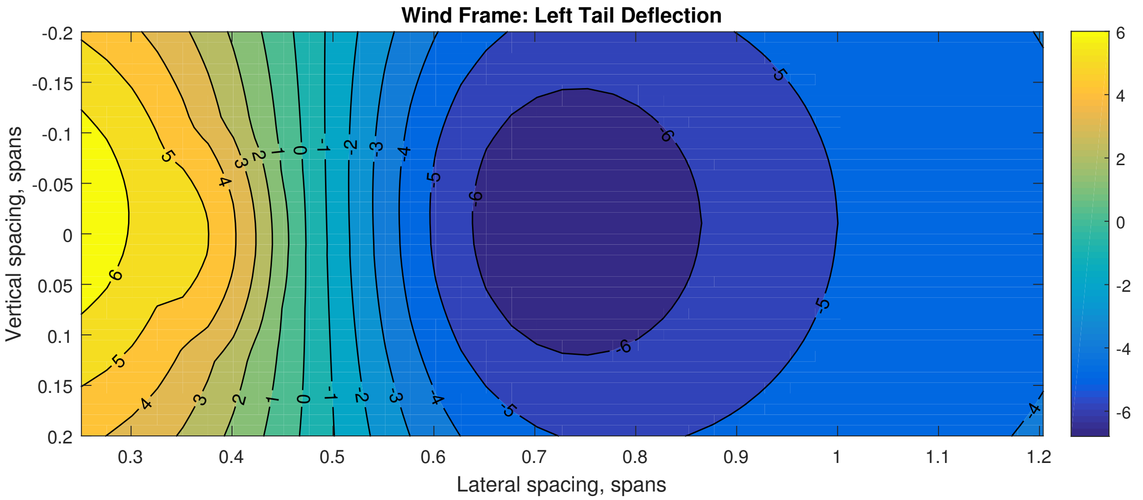

Figure E.43. Left Tail Deflection Simulation Results for the Empty F-15C Light Tanker Case.

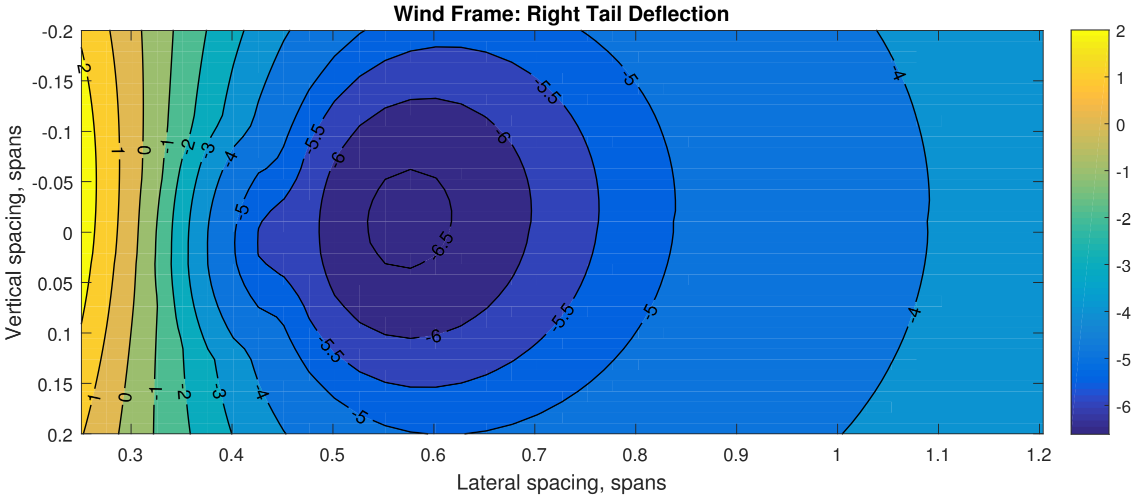

Figure E.44. Right Tail Deflection Simulation Results for the Empty F-15C Light Tanker Case.

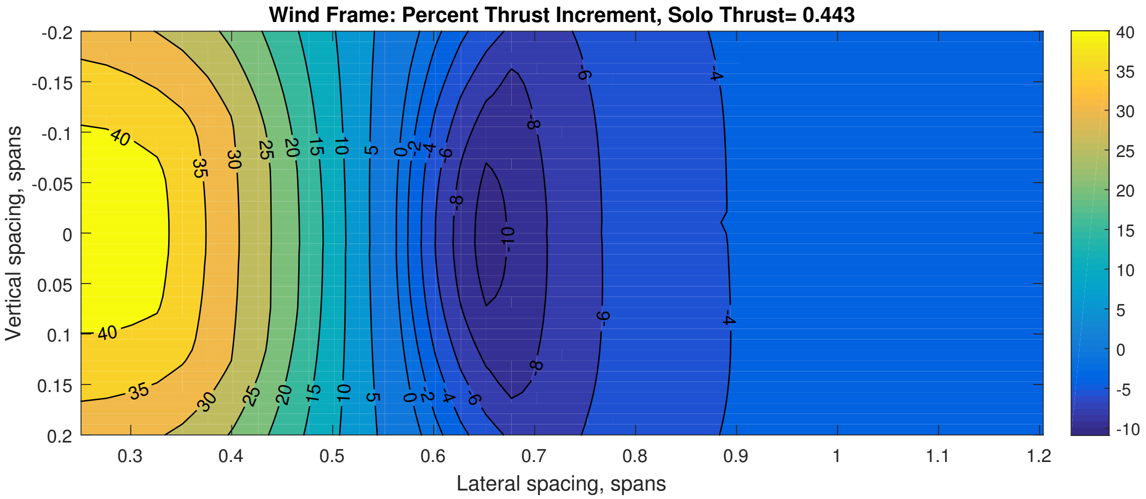

Figure E.45. Thrust Increment Simulation Results for the Empty F-15C Light Tanker Case.

E.3 F-15E

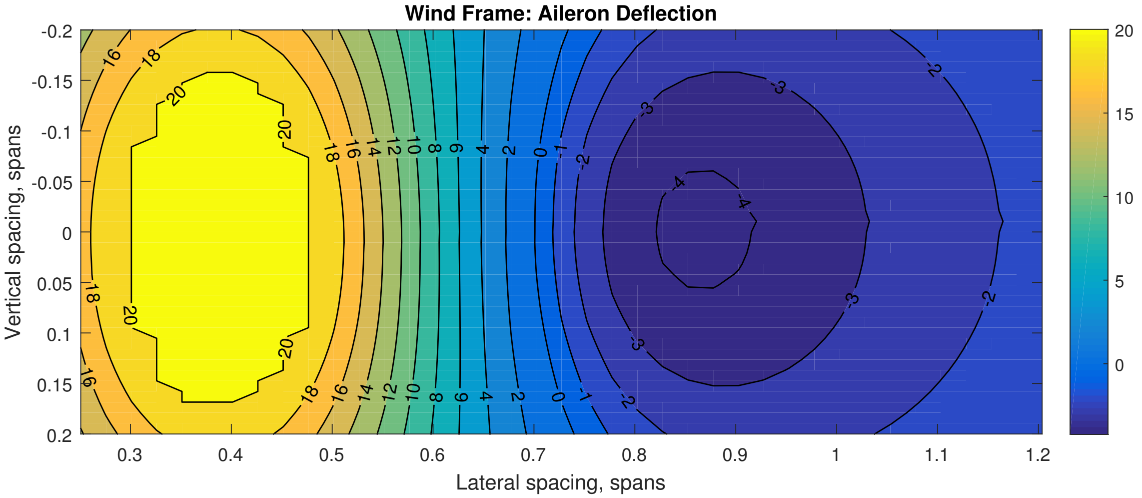

Figure E.46. Aileron Deflection Simulation Results for the Empty F-15E Heavy Tanker Case.

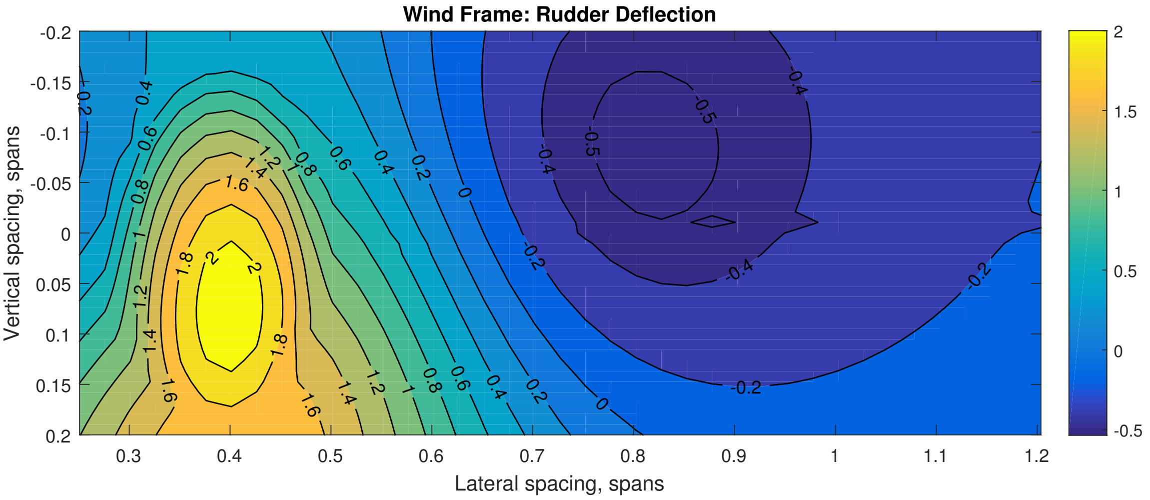

Figure E.47. Rudder Deflection Simulation Results for the Empty F-15E Heavy Tanker Case.

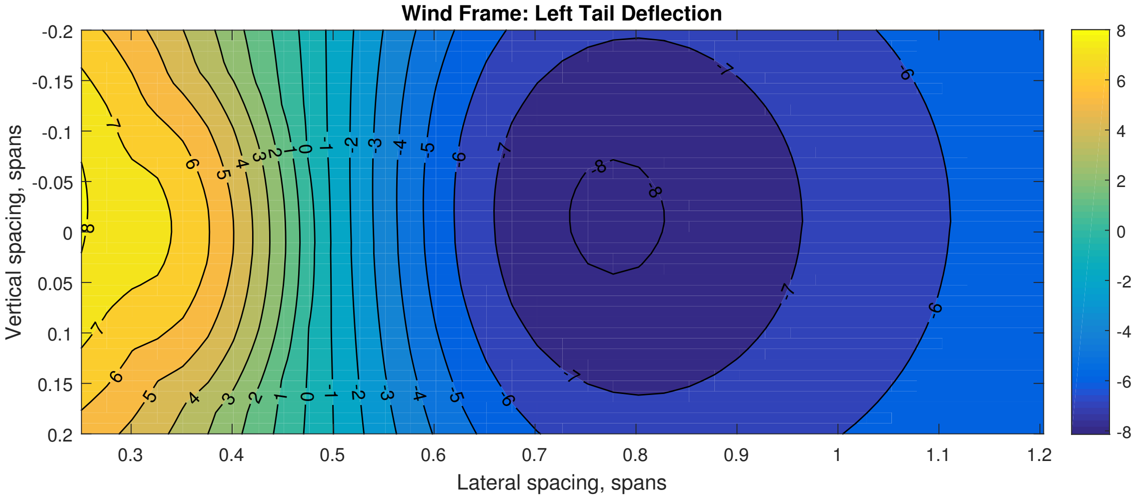

Figure E.48. Left Tail Deflection Simulation Results for the Empty F-15E Heavy Tanker Case.

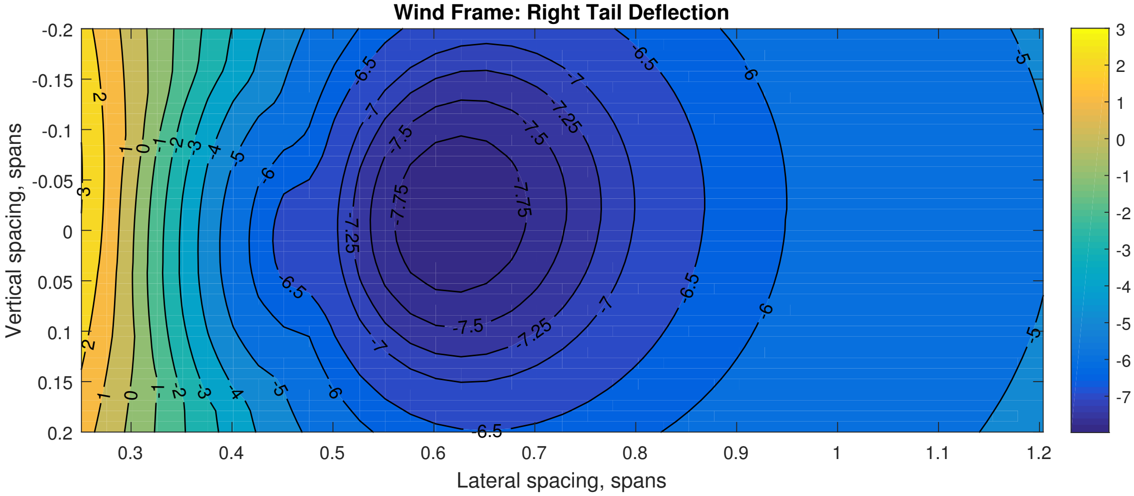

Figure E.49. Right Tail Deflection Simulation Results for the Empty F-15E Heavy Tanker Case.

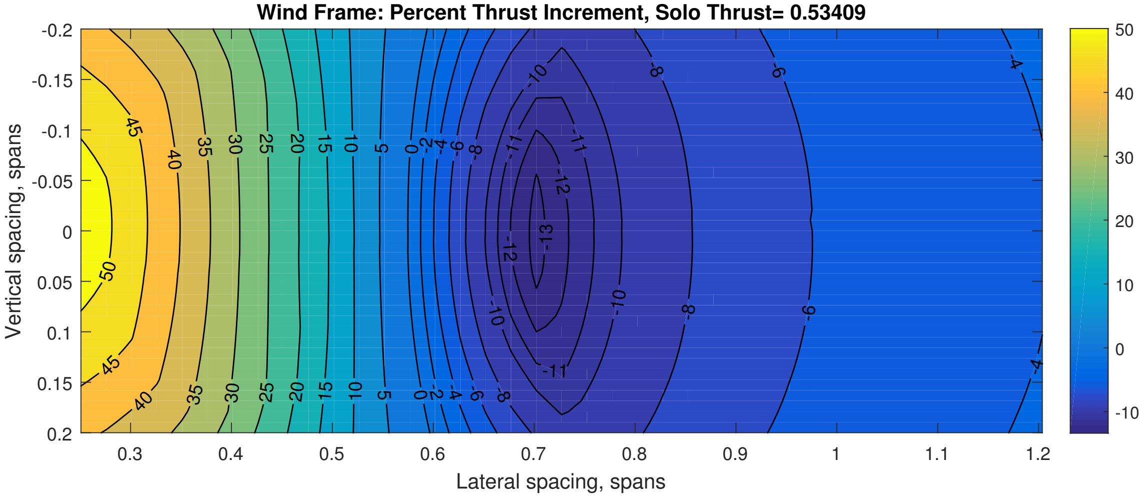

Figure E.50. Thrust Increment Simulation Results for the Empty F-15E Heavy Tanker Case.

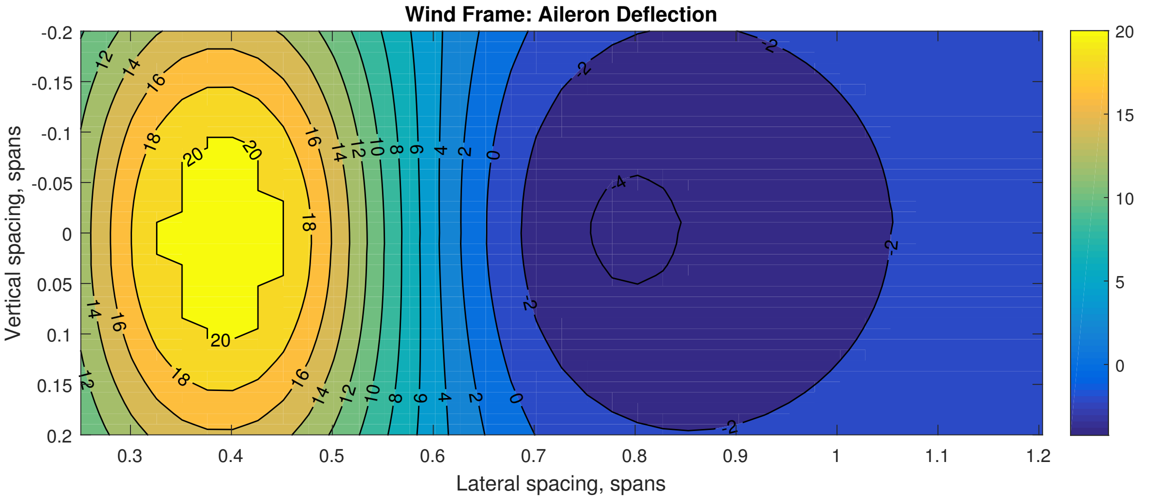

Figure E.51. Aileron Deflection Simulation Results for the Full F-15E Light Tanker Case.

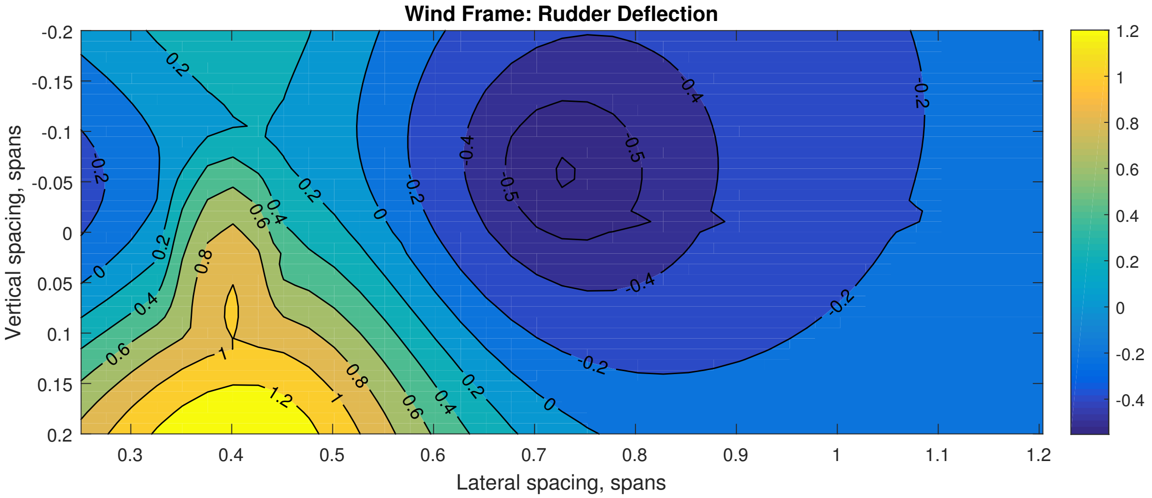

Figure E.52. Rudder Deflection Simulation Results for the Full F-15E Light Tanker Case.

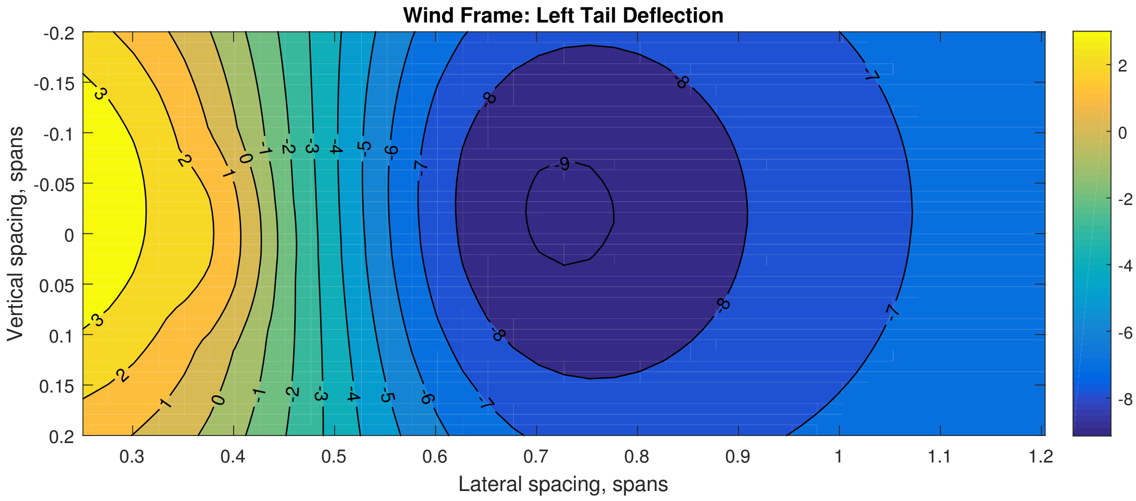

Figure E.53. Left Tail Deflection Simulation Results for the Full F-15E Light Tanker Case.

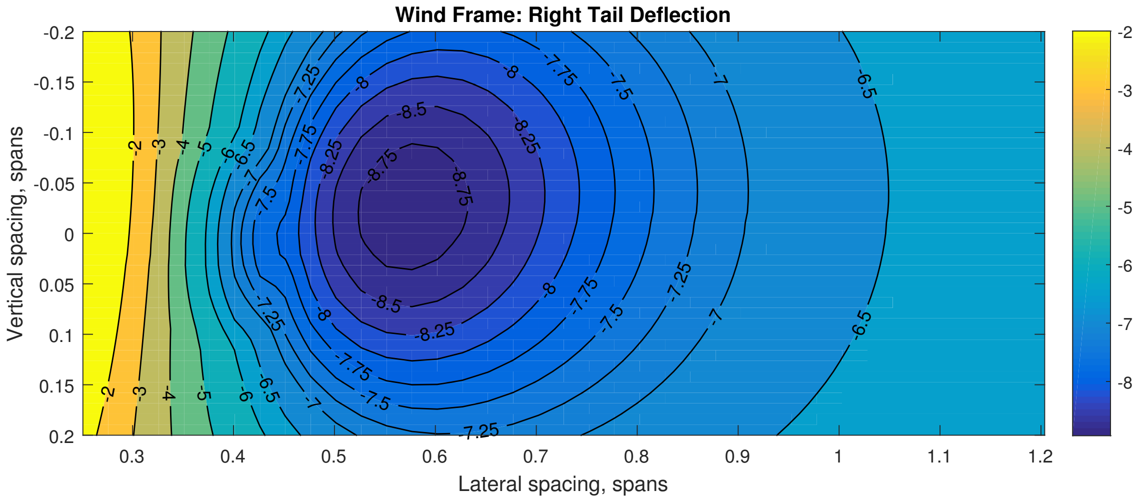

Figure E.54. Right Tail Deflection Simulation Results for the Full F-15E Light Tanker Case.

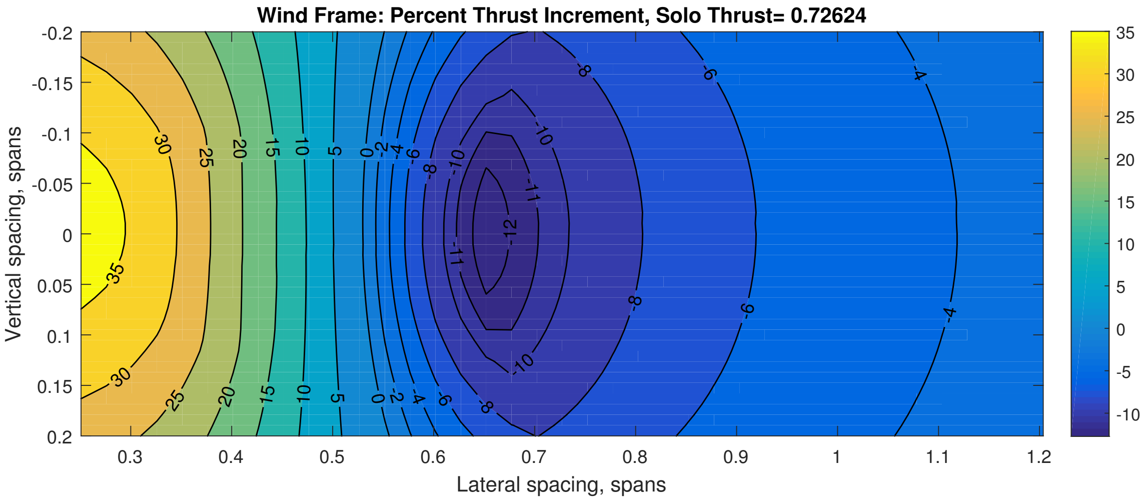

Figure E.55. Thrust Increment Simulation Results for the Full F-15E Light Tanker Case.

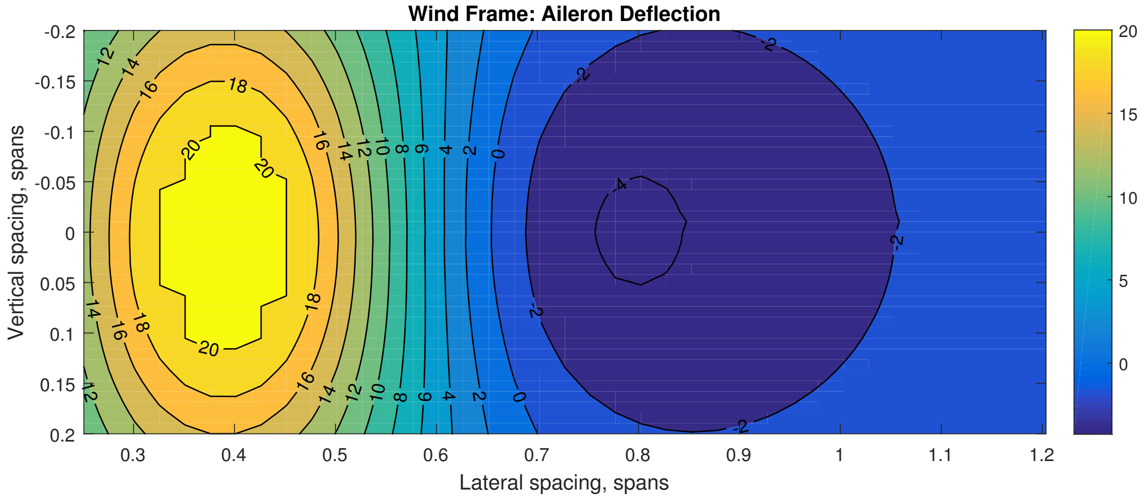

Figure E.56. Aileron Deflection Simulation Results for the Empty F-15E Light Tanker Case.

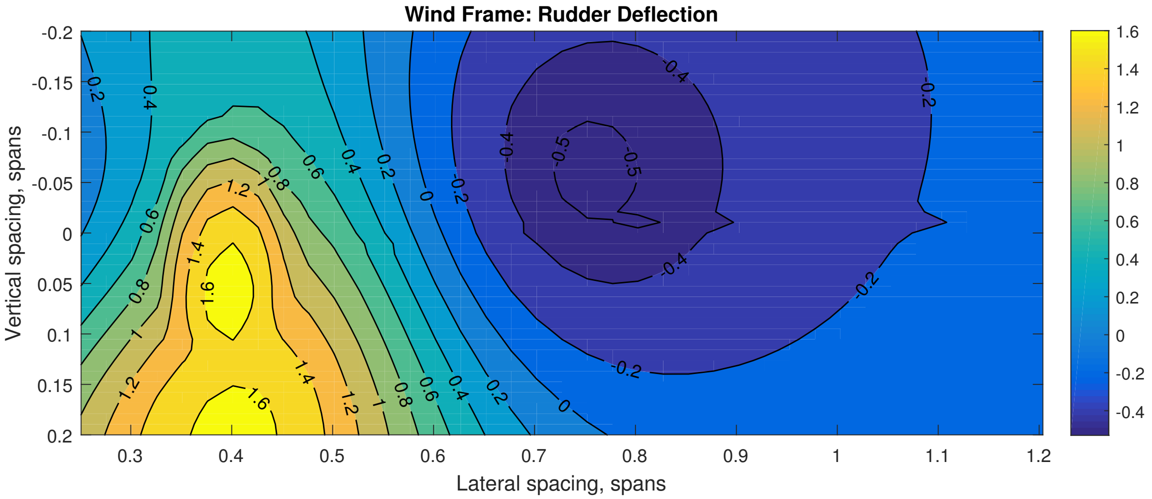

Figure E.57. Rudder Deflection Simulation Results for the Empty F-15E Light Tanker Case.

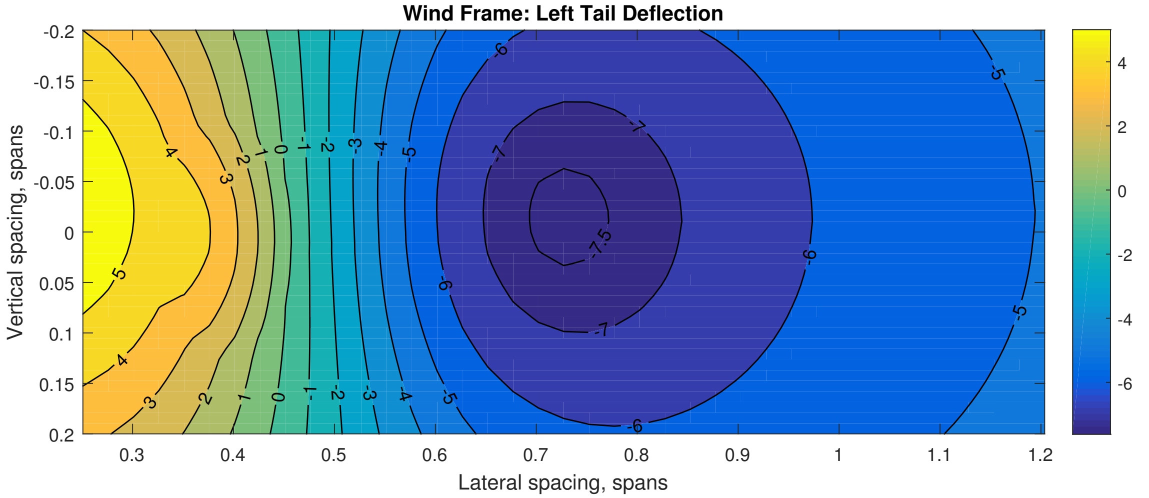

Figure E.58. Left Tail Deflection Simulation Results for the Empty F-15E Light Tanker Case.

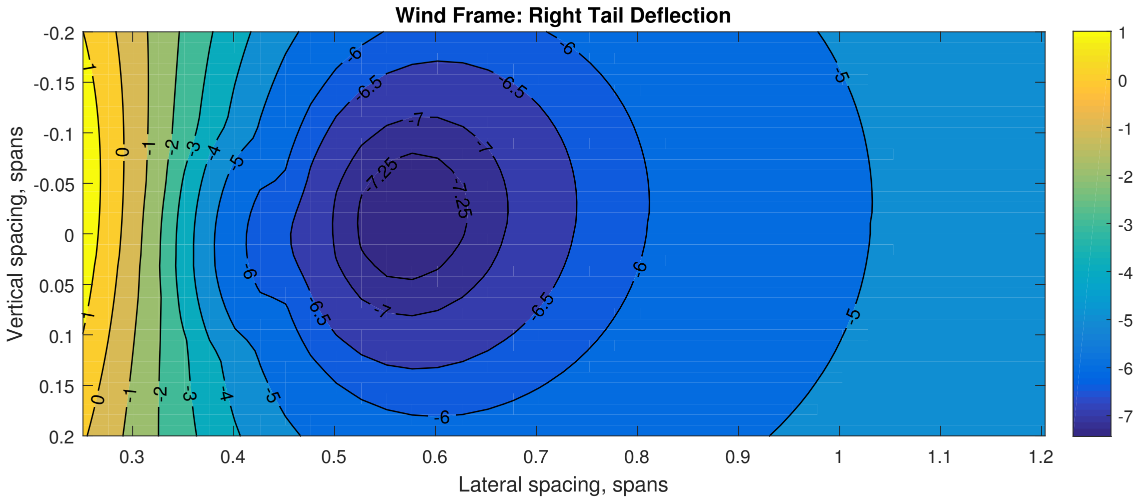

Figure E.59. Right Tail Deflection Simulation Results for the Empty F-15E Light Tanker Case.

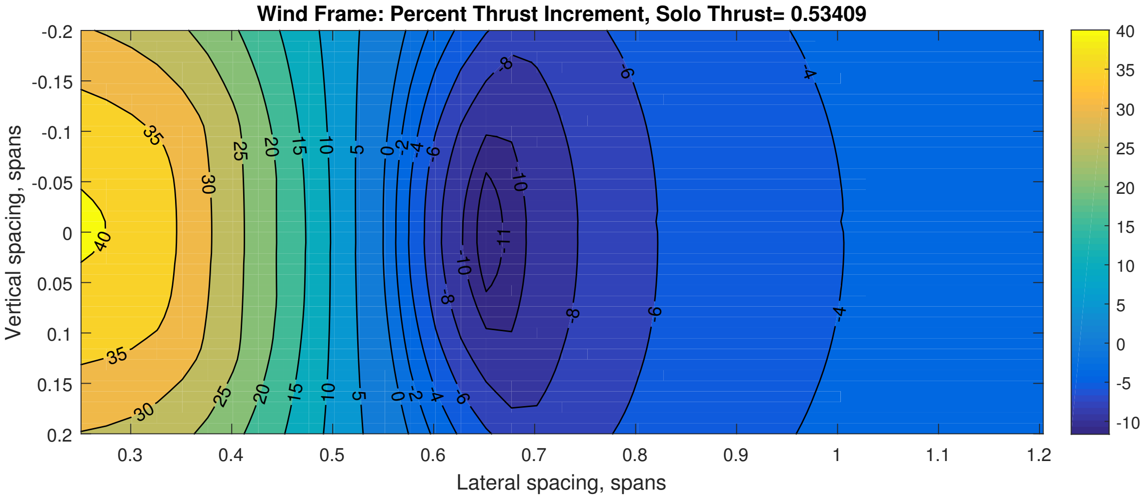

Figure E.60. Thrust Increment Simulation Results for the Empty F-15E Light Tanker Case.

REFERENCES

[1] W. Blake, S. Bieniawski, and T. Flanzer, “Surfing aircraft vortices for energy,” *Journal of Defense Modeling & Simulation*, vol. 12, no. 1, pp. 31–39, January 2015.

[2] “Air mobility operations,” Joint Chiefs of Staff, Publication 3-17, 30 September 2013.

[3] T. Stuart, “Coronet vs cargo: A study into increasing the usage of tanker asserts for cargo movement on coronet positioning and de-positioning legs,” Master’s thesis, Air Force Institute of Technology Thesis AFIT/IMO/ENS/10-13, June 2010.

[4] T. Flanzer, S. Bieniawski, and W. Blake, “Operational analysis for the formation flight for aerodynamic benefit program,” in *AIAA paper 2014-1460.* National Harbor MD: AIAA SciTech, January 2014.

[5] “Sky surfing for fuel economy,” press release, NASA, 24 July 2003.

[6] J. Tucker, A. Dogan, and W. Blake, “Derivation of the dynamics equations of receiver aircraft in aerial refueling,” in *proceeding of AIAA 45th AIAA Aerospace Sciences Meeting and Exhibit*, Reno, Nevada, Jan 8 - 11 2007.

[7] J. Waishek, A. Dogan, and W. Blake, “Derivation of the dynamics equations of receiver aircraft in aerial refueling,” *AIAA Journal of Guidance, Control and Dynamics*, vol. 32, no. 2, pp. 585–597, 2009.

[8] A. Dogan, E. Kim, and W. Blake, “Control and simulation of relative motion for aerial refueling in racetrack maneuvers,” *Journal of Guidance, Control and Dynamics*, vol. 30:5, pp. 1551–1557, 2007.

[9] A. Dogan, S. Venkataramanan, and W. Blake, “Modeling of aerodynamic coupling between aircraft in close proximity,” *AIAA Journal of Aircraft*, vol. 42:4, pp. 941–955, Jul–Aug 2005.

[10] A. Dogan and S. Venkataramanan, “Nonlinear control for reconfiguration of unmanned–aerial–vehicle formation,” *AIAA Journal of Guidance, Control and Dynamics*, vol. 28:4, pp. 667–678, Jul–Aug 2005.

[11] A. Dogan, “Effect of the wake vortex with turbulence on the control of a UAV in aerial refueling,” Control Design & Analysis Branch of Air Vehicles Directorate, AFRL, WPAFB, OH, Final Report of Air Vehicles Directorate Summer Faculty Research Program, October 30 2007.

[12] A. Dogan, T. Lewis, and W. Blake, “Wake-vortex induced wind with turbulence in aerial refueling - part a: Flight data analysis,” in *proceeding of AIAA Atmospheric Flight Mechanics Conference*, Honolulu, HI, Aug 18-21 2008, AIAA paper 2008-6696.

[13] ——, “Wake-vortex induced wind with turbulence in aerial refueling - part b: Model and simulation validation,” in *proceeding of AIAA Atmospheric Flight Mechanics Conference*, Honolulu, HI, Aug 18-21 2008, AIAA paper 2008-6697.

[14] ——, “Flight data analysis and simulation of wind effects during aerial refueling,” *AIAA Journal of Aircraft*, in press for publication.

[15] A. Dogan, “Control design and analysis of eq-ii receiver model in aerial refueling,” Control Design & Analysis Branch of Air Vehicles Directorate, AFRL, WPAFB, OH, Final Report of Air Vehicles Directorate Summer Faculty Research Program, July, 22 2008.

[16] W. Okolo, A. Dogan, and W. Blake, “Determination of sweet spot for trailing aircraft in formation flight,” in *proceeding of AIAA Atmospheric Flight Mechanics*

Conference. Portland, Oregon: American Institute of Aeronautics and Astronautics, August 8-11 2011, AIAA paper 2011-6302.

[17] ——, “Aircraft lateral trim using internal fuel transfer and differential thrust in formation flight,” in *proceeding of AIAA Atmospheric Flight Mechanics Conference.* Portland, Oregon: American Institute of Aeronautics and Astronautics, August 8-11 2011, AIAA paper 2011-6613.

[18] ——, “Application of sweet spot determination to a conventional pair of aircraft,” in *Proceedings of AIAA Atmospheric Flight Mechanics Conference*, Minneapolis, Minnesota, 13-16 August 2012, AIAA paper 2012-4402.

[19] W. Okolo, “Evaluating and augmenting fuel-saving benefits obtained in aircraft formation flight,” Ph.D. dissertation, The University of Texas at Arlington, Arlington, TX, May 2015.

[20] W. Okolo, A. Dogan, and W. Blake, “Quantification of trail aircraft performance in formation flight considering fuel burn,” in *proceeding of AIAA Aircraft Flight Dynamics, Control, Handling Qualities and Performance Conference*, 2015.

[21] ——, “Wind and turbulence effects on ride quality in formation flight,” in *proceeding of AIAA Atmospheric and Space Environments*, 2015.

[22] C. Kniffin, A. Dogan, and W. Blake, “Formation flight for fuel saving in coronet mission - part a: Sweet spot determination,” in *proceeding of AIAA Atmospheric Flight Mechanics Conference*, Washington, DC, Jun 13-17 2016, AIAA paper 2016-3393.

[23] ——, “Formation flight for fuel saving in coronet mission - part b: Full mission analysis,” in *proceeding of AIAA Atmospheric Flight Mechanics Conference*, Washington, DC, Jun 13-17 2016, AIAA paper 2016-3537.

[24] A. Dogan and W. Blake, *Flight Mechanics of Aerial Refueling.* Draft Book, Washington, DC: AIAA, December 2010.

[25] L. Nguyen and et al, “Simulator study of stall/post stall characteristics of a fighter airplane with relaxed longitudinal static stability,” in *NASA TP 1538*, December 1979.

[26] K. Iliff and R. Maine, “Subsonic stability and control derivatives for an unpowered, remotely piloted 3/8 scale f-15 airplane model obtained from flight test,” in *NASA TN D-8136*, January 1976.

[27] M. Brenner, K. Iliff, and R. Whitman, “Effect of sampling rate and record length on the determination of stability and control derivatives,” in *NASA TM 72858*, December 1978.

[28] S. Grafton, M. Croom, and L. Nguyen, “High angle of attack stability characteristics of a three-surface fighter configuration,” in *NASA TM 84584*, March 1983.

[29] D. Banks, P. Quntio, and J. P. Jr, “Thrust induced effects on low-speed aerodynamics of fighter aircraft,” in *NASA TM 83277*, May 1982.

[30] S. McWherter, C. Moua, J. Gera, and T. Cox, “Stability and control analysis of the F-15B quiet spike aircraft,” in *NASA TM 2009-214561*, August 2009.

[31] T. Sieron, D. Fields, A. Baldwin, and D. Adamczak, “Procedures and design data for the formulation of aircraft configurations,” in *WL-TR-93-3068*, August 1993.

[32] E. Saltzman and J. Hicks, “In-flight lift-drag characteristics for a forward-swept wing aircraft and comparisons with contemporary aircraft,” in *NASA TP 3414*, 1994.

[33] D. Shlapak, J. Stillion, O. Oliker, and T. Charlick-Paley, “A global access strategy for the u.s. air force,” in *RAND Report MR-1216-AF*, 2002.

[34] W. Okolo, A. Dogan, and W. Blake, “Effect of trail aircraft trim on optimum location in formation flight,” *Journal of Aircraft*, 25 Nov 2014.

[35] W. Blake, D. Leggett, and A. Romero, "Low speed testing and simulation of the STOL and maneuver technology demonstrator," in *effect paper 90-1820.* Los Angeles CA: AIAA Aerospace Engineering Conference & Show, February 1990.

[36] S. Venkataramanan and A. Dogan, "Modeling of aerodynamic coupling between aircraft in close proximities," in *Proceedings of the AIAA Atmospheric Flight Mechanics Conference and Exhibit*, Providence, RI, Aug 2004, AIAA paper 2004-5172.

[37] ——, "Dynamic effects of trailing vortex with turbulence & time-varying inertia in aerial refueling," in *Proceedings of the AIAA Atmospheric Flight Mechanics Conference and Exhibit*, Providence, RI, Aug 2004, AIAA paper 2004-4945.

[38] ——, "A Multi-UAV simulation for formation reconfiguration," in *Proceedings of the AIAA Modeling and Simulation Technologies Conference and Exhibit*, Providence, RI, Aug 2004, AIAA paper 2004-4800.

[39] S. Venkataramanan, A. Dogan, and W. Blake, "Vortex effect modelling in aircraft formation flight," in *Proceedings of the AIAA Atmospheric Flight Mechanics Conference and Exhibit*, Austin, TX, Aug 2003, AIAA paper 2003-5385.

[40] S. Venkataramanan and A. Dogan, "Nonlinear control for reconfiguration of uav formation," in *Proceedings of the AIAA Guidance, Navigation, and Control Conference*, Austin, TX, Aug 2003, AIAA paper 2003-5725.

[41] S. Venkataramanan, *Dynamics and Control of Multiple UAVs Flying in Close Proximity.* Arlington, TX: M.S. Thesis, The University of Texas at Arlington, 2004.

[42] A. Dogan, S. Sato, and W. Blake, "Flight control and simulation for aerial refueling," in *Proceedings of AIAA Guidance, Navigation, and Control Conference*, San Francisco, CA, Aug 2005, AIAA paper 2005-6264.

[43] E. Kim, A. Dogan, and W. Blake, “Control of a receiver aircraft relative to the tanker in racetrack maneuver,” in *proceeding of AIAA Guidance, Navigation, and Control Conference*, Keystone, CO, Aug 21-24 2006, AIAA paper 2006-6710.

[44] M. D. Tandale, R. Bowers, and J. Valasek, “Trajectory tracking controller for vision-based probe and drogue autonomous aerial refueling,” *AIAA Journal of Guidance, Control, and Dynamics*, vol. 29, no. 4, pp. 846–857, 2006, 0731-5090.

[45] M. Mammarella, G. Campa, M. R. Napolitano, M. L. F. ML, Y. Gu, and M. G. Perhinschi, “Machine vision/GPS integration using EKF for the UAV aerial refueling problem,” *IEEE Transactions On Systems Man And Cybernetics Part C-Applications And Reviews*, vol. 38, no. 6, pp. 791–801, November 2008.

[46] D. Saban, J. F. Whidborne, and A. Cooke, “Simulation of wake vortex effects for UAVs in close formation flight,” *Aeronautical Journal*, vol. 113, no. 1149, pp. 727–738, November 2009.

BIOGRAPHICAL STATEMENT

Christopher A. Kniffin enrolled at the University of Texas at Arlington (UTA) in 2009 for his undergraduate studies in aerospace engineering. As an undergraduate, he interned with Triumph Aerostructures. After graduating with his B.S. in 2013, he worked at Contract Fabrication and Design, where he worked on rotorcraft armament mounting systems. He began his graduate studies in the summer of 2015, when he also accompanied his advisor to the Air Force Research Laboratory (AFRL). During his graduate studies, he also worked on flight simulators at L-3 Link.